Low background techniques for the SuperNEMO experiment

Xin Ran Liu
University College London

Submitted to University College London in fulfilment
of the requirements for the award of the
degree of **Doctor of Philosophy**

12th January, 2017

Declaration

I, Xin Ran Liu, confirm that the work presented in this thesis is my own. Where information has been derived from other sources, I confirm that this has been indicated in the thesis.

[redacted]

Xin Ran Liu

Abstract

SuperNEMO is a $0\nu\beta\beta$ experiment aiming to reach a half-life sensitivity of 10^{26} years corresponding to an effective Majorana neutrino mass of $\langle m_{\beta\beta}\rangle < 50$ - 100 meV. Stringent radio-purity constraints are therefore placed on the detector construction material as well as the gases used in the central detector tracking volume.

Radon, ^{222}Rn, is one of the most problematic backgrounds for SuperNEMO due to its decay daughter, ^{214}Bi, having a high $Q_{\beta\beta}$ value. Hence the radon level within the SuperNEMO tracker gas mixture must not exceed 150 µBq/m^3. This activity is beyond the measurement capability of standard radon detectors, therefore a "Radon Concentration Line" was designed and constructed. This instrument has demonstrated the ability to measure the SuperNEMO tracker gas to a sensitivity of 20 µBq/m^3. For large volume of gases the ^{222}Rn activity can be measured with a sensitivity of <5 µBq/m^3. Measurements of the fully instrumented quarter trackers and its subsystems have been performed. Radon emanation chambers have also been built to be used with the electrostatic detector which has demonstrated sensitivities of <190 µBq.

High-purity germanium detectors offer a standard method to measure material contamination. A dedicated screening facility has been established at Boulby Underground Laboratory with four detectors fully commissioned for low background material measurements. Such a detector can be used to make a highly sensitive measurement of ^{96}Zr decay to the 0^+_1 excited state. Simulations of an experimental setup using 20 kg of ^{96}Zr have shown a sensitivity of 10^{21}yrs can be

achieved with a 1 year measurement, a factor of 3 improvement on current world's best limit.

Acknowledgements

First and foremost I would like to express my deepest and most sincere gratitude to my first supervisor Ruben Saakyan who was simply the best supervisor I could have asked for, better in fact than I could have imagined. It is hard for me to envisage working for anyone else and anywhere else without his guidance, in particular his ability to clarify any problem I have. To appropriately express my appreciation for everything he has done would require doubling the length of this thesis, so in the interesting of saving the trees I will simply say - thank you!

The same gratitude must also be expressed for my second supervisor, Chamkaur Ghag, whom from the start was much more involved with my project than the conventional job description of a UCL second supervisor. Interestingly, after the four year process, he also entirely fulfilled his primary directive which is the emotional counsellor, there to support the student whenever necessary. While the four years of PhD educated my mind, Cham also educated my soul. He rekindled my faith in humanity, introduced new ideas and radically challenged my thinking. For all this I shall be eternally grateful and I shall prove it through my actions.

I have always prided myself on living a life without any regrets, there isn't a single moment in my past I would alter nor a decision I would change. However, I do regret now having studied for 4 years under two of the most amazing people I can think of as my teachers, that I did not learn more from them both and taken greater advantage of this incredible opportunity. Thank you both for your endless patience.

I'm also extremely thankful for everyone in the NEMO group at UCL, past and present, from passionate office discussions to help and assistance whenever required. I am honoured to have met you all; David Water, James Mott, Anastasia (Bash) Freshville, Stefano Torres, Guillaume Eurin, Cristovao Vilela, Michele Cascella and of course Derek Attree and I number you all amongst my friends. This also extends

to Summer Blot and Pawel Guzowski, who are honorary UCL, especially as Summer is officially listed as so on DocDB.

A special thank you must go to Rob Flack for his knowledge, encouragement and above all for teaching me the importance of patience and following a plan through. Without him I might never have pursued a PhD in particle physics. I must also thank the SuperNEMO collaboration and everyone in it who made my four years such a pleasure, I genuinely cannot imagine a better experiment to be part of nor a friendlier mix of incredible people. A special thank to Frederick and Pia for their endless patience dealing with all my emails, John for all the great times (not to mention back flips) during collaboration meetings, Ramon for just being you, Benjamin Soule for being my French counterpart setting such a great example and Magali for making my life far too easy, I will miss you very much.

I also want to thank Emma, Paul and Sean at the Boulby Underground Laboratory for all their help and for showing me a truly unique place to do science.

A great big thank you to everyone in my office; Leigh, Ines, David, Lauren and Vincenzo who made my four years fly by. Also everyone in the UCL HEP group in particular; Becky Chislett, Alex Martyniuk, Andy Perch, Ben Strutt, Laura Manenti and Jim Dobson who made this one of the most memorable experiences of my life, and one I will remember fondly always. A special thanks to Sally Shaw for being there for me when GEANT4 wasn't. To my friends; Giulio Pepe, Becca Falla, Elisabeth Schopf, Andy Edmonds, Tom Webb and Emma Wroe for keeping me sane, at least to your best abilities. I can't imagine life without your friendship, so it's good I don't have to.

I want to thank Mr Brothwick and Mr Roberts for your patience and encouragement. I am writing this today because you believed in me over a decade ago. Anna Price and Ross Mitchell for starting my year, every year of this PhD, in the best way I can imagine. Finally and critically thank you to my parents who gave me life, the universe and everything.

To Jenna Deakin

> *"I love you, always. Time is nothing."*
> \- The Time Traveler's Wife

Contents

List of figures

List of tables

Chapter 1.

Introduction

The Standard Model of particle physics is the best theory of elementary particle physics at present and it is the most rigorously tested model in all of physics. The discovery of a Higgs like particle was another jigsaw piece falling into place, further validating the Standard Model.

However, the Standard Model describes only the baryonic sector of the universe, less than 5% of total mass-energy, and does not account for gravity. With the repeated observation of neutrino oscillations and flavour mixing, cracks are beginning to show in the Standard Model armour as it cannot conveniently incorporate massive neutrinos. These observations also open questions about the nature of the neutrino which cannot yet be answered by oscillation experiments alone. Questions such as what is the absolute neutrino mass cannot be answered by oscillations experiments as these are only able to measure mass difference between the three neutrino eigenstates. It is also unclear which of the three neutrinos is the lightest, hence putting in question the mass hierarchy.

The neutrinos may also be either Dirac or Majorana fermions. In the Dirac case, the neutrino would have a distinct anti-neutrino counter part, whereas, in the Majorana case the neutrino would be its own antiparticle. Whether neutrinos are Majorana or Dirac can only be tested through neutrinoless double beta ($0\nu\beta\beta$) decay experiments. The confirmation of the neutrinos as Majorana would provide unambiguous evidence for lepton number violation, a requirement for many Grand Unification Theories (GUT) to explain the matter and anti-matter asymmetry observed today and have major implications for the formation of the universe.

The SuperNEMO experiment is designed to search for the hypothesised $0\nu\beta\beta$ decay process with a capability to reach a half-life sensitivity of 10^{26} years. This corresponds to an effective Majorana neutrino mass of $\langle m_{\beta\beta} \rangle < 50$ - 100 meV. It distinguishes itself from other double beta decay experiments as it can reconstruct the 3D topology of each detected event thus providing a unique and powerful background rejection method and “smoking gun" evidence for the process.

This is an area of intense research with many of the new generation $0\nu\beta\beta$ decay experiments coming online and producing the first search results in various isotopes. The SuperNEMO detector is well placed to competitively search for the $0\nu\beta\beta$ decay with the isotope ^{82}Se, however, it is uniquely designed to be able to change and accommodate other isotopes if they are found to be more favourable.

A critical concern of any experiment waiting for an $0\nu\beta\beta$ event is the detector background. Earth is unfortunately a radioactive planet, as there are trace levels of contamination by uranium (U) and thorium (Th) in all materials. Due to the relatively short half-lives of U and Th compared to current half-life limits on $0\nu\beta\beta$ process, it is essential to ensure the radio-purity of the detector components in order to achieve a credible signal to noise ratio.

The way to minimise radiation background is through a dedicated screening and selection process using an array of complementary techniques such as gamma ray spectroscopy, radon measurements and mass spectrometry. This screening is essential not only for the selection of radio-pure materials, but also to better understand sources of background and their contribution to the detector background. This information can then be fed into simulations to estimate the number of expected background events at the region of interest during measurement.

Such techniques are required for all rare event search experiments. A key example is direct dark matter detection which faces many of the same challenges as $0\nu\beta\beta$ decay experiments and therefore requires similar material cleanliness. For example, the LUX Zeplin (LZ) experiment aims to update and improve on the current world leading dark matter experiment LUX technology. It will essentially use the same design however extrapolated by one order of magnitude in terms of xenon mass, in order to achieve target sensitivity. The LZ detector has onerous constraints on radio-purity requirements to achieve < 0.5 cts/ton/yr of combined electronic and nuclear recoils. Although the dominant source of background differs, between the

$0\nu\beta\beta$ decay and dark matter experiments, the demand for radio-purity remains the same.

1.1. Author's Contributions

Establishment of Germanium Facility at Boulby:

- Refurbished old germanium detector, cleaned and reassembled detector shielding
- Installed anti-radon shielding with gas purging system to detector
- Developed analysis software for gamma ray spectroscopy data
- Developed GEANT4 simulations for detection efficiency and detector calibrations
- Carried out material screening for SuperNEMO

Improvements to Boulby Germanium Facility:

- Installed three additional new low-background detectors
- Designed new customised shielding for each detector
- Helped to design and move all four detectors into a new dedicated germanium facility inside a class 1000 cleanroom
- Prepared SuperNEMO and LZ samples for screening and analysed the results
- Worked on possible ways to determine radon emanation suppression at liquid nitrogen temperatures

Germanium Studies of ^{96}Zr:

- Selected samples of zirconium oxide for radio-purity test
- Carried out MC studies to optimise the geometry for an experiment aimed at searching ^{96}Zr double-β decay to excited states
- Carried out sensitivity estimates for the double-β of ^{96}Zr to the 0_1^+ excited state of ^{96}Mo with a large ultra-low background HPGe detector

Radon concentration line:

- Designed and installed new carbon trap
- Installed new cooler to improve trapping efficiency
- Installed and tested new radon purification system for input gas
- Calibrated the new system
- Improved radon adsorption efficiency by a factor 2
- Improved trapping and transfer efficiency by a factor 2

Radon Emanation Chambers:

- Constructed, tested and commissioned two radon emanation chambers
- Developed cleaning process to ensure stable background
- Measured radon emanation of LZ and SuperNEMO materials
- Improved design for future emanation chambers

Radon measurements:

- First three quarter-sections of the SuperNEMO tracker
- Purified radon gas, gas bottles and gas delivery lines
- SuperNEMO gas mixing and delivery system
- Clean room where SuperNEMO is being built

R&D with 3D Printers :

- Design and printed objects used for material screening
- Selected 3D printing material for radio-purity

Presentation of the collaboration's work at Neutrino2014 (poster), Neutrino2016 (poster), IOP2016 (talk), NuPhys2013 (poster), NuPhys2014 (poster) & LRT2015 (talk)

Chapter 2.

Neutrino Mass Theoretical Background

2.1. Discovery

The neutrino was first postulated in 1930 by Pauli to explain a problem which had arisen in studies of nuclear beta decays. In such two-body decays if the parent nucleus, A, is at rest whilst the decay daughter nucleus, B, and the electron come out back-to-back with equal and opposite momenta then conservation of energy dictates the electron must have energy;

$$E = \left(\frac{m_A^2 - m_B^2 + m_e^2}{2m_A} \right) \tag{2.1}$$

where E should be fixed. In experimental measurements however, E resulted in a continuous spectrum. This resulted in Niels Bohr loosing his mind (not for the last time[1]) and abandon all reason for madness by proposing to forsake the conservation of energy.

Pauli instead proposed there must another particle emitted with the electron, which eludes detection, carrying away a fraction of the energy. He proposed to call this

---

[1] Bohr was an outspoke critic of Einstein's light quantum (prior to 1924), he discouraged Dirac's work on the relativistic electron theory, opposed Pauli's introduction of the neutrino, ridiculed Yukawa's theory of the meson and disparaged Feynman's approach to quantum electrodynamics [1].

particle the neutron since it must be electrically neutral to conserve charge. His proposal was incorporated into a theory of beta decay by Enrico Fermi. Since the name neutron was already taken, Fermi called this new particle the neutrino. Its existence was experimentally confirmed in 1956 by Cowan and Reines [2] using two large tanks of water doped with cadmium chloride and the “inverse" beta-decay reaction;

$$\bar{\nu} + p \rightarrow n + e^{+} \tag{2.2}$$

The neutrino is an elementary particle with spin $\frac{1}{2}$, it possesses no electric charge and only interacts weakly with matter. Neutrinos have left handed chirality and helicity, according to the Standard Model (SM), which assumes them to be massless.

Since neutrinos are electrically neutral, studies were conducted to determine whether distinctions existed between the neutrino and the anti-neutrino. In the late fifties, following the results of Cowan and Reines, Davis and Harmer [3] looked for the analogous reaction using anti-neutrinos

$$\bar{\nu} + n \rightarrow p + e^{-} \tag{2.3}$$

and found that it does not occur, establishing that the neutrino and anti-neutrino are distinct particles. Davis and Harmer therefore confirmed the rule introduced by Konopinski and Mahmoud [4] in 1953, which in effect assigned a lepton number $L = +1$ to; the electron, the muon, the tau and the neutrino and $L = -1$ to their subsequent anti-particles as well as proposed that lepton number in conserved.

Thus, the properties which distinguish the neutrino from the anti-neutrino are their lepton number: $L = +1$ for neutrinos and $L = -1$ for antineutrinos and their helicity: the neutrino is “left handed" whereas the antineutrino is “right-handed".

2.2. The Standard Model

The Standard Model of particle physics is the current best theory to describe the interactions of baryonic matter, leptons and gauge bosons of the universe. In this model, all matter is made from three types of elementary particles; leptons, quarks and their mediators. The elementary particles are classified as either fermions (with spin $\frac{1}{2}$) or bosons (with integer spin).

There are six leptons which are composed into three families, or generations, classified by their charge (Q) and lepton number ($L_{e,\mu,\tau}$). The same classification also applies to the quark sector, where there are also six quarks split into three families.

There are three forces in the Standard Model each having associated mediators. The elctro-magnetic force is mediated by the photon, the weak force by W^+, W^- and Z bosons and the strong force by the gluon.

The SM was completed by the discovery of the Higgs boson, which is responsible for the mass generation mechanism for bosons and fermions. Within the SM, the final count currently stands at 17 elementary particles as summarised in Figure 2.1.

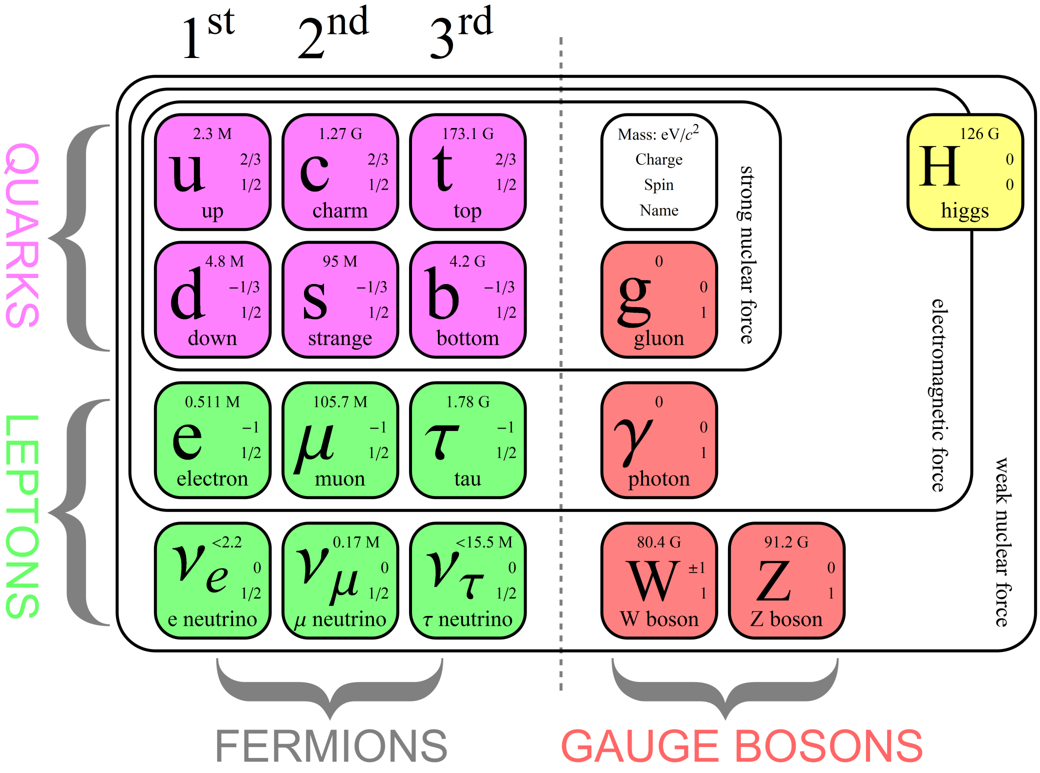

Figure 2.1: A summary of current elementary particles and their properties [5].

2.3. Standard Model Neutrinos

In the SM, neutrinos interact only via the weak force, either through a charged current (CC) interaction, involving the charged $W^{\pm}$ exchange, or a neutral current (NC) interaction with Z^0 exchange. The four possible interactions detectable by neutrino detectors are shown in Figure 2.2.

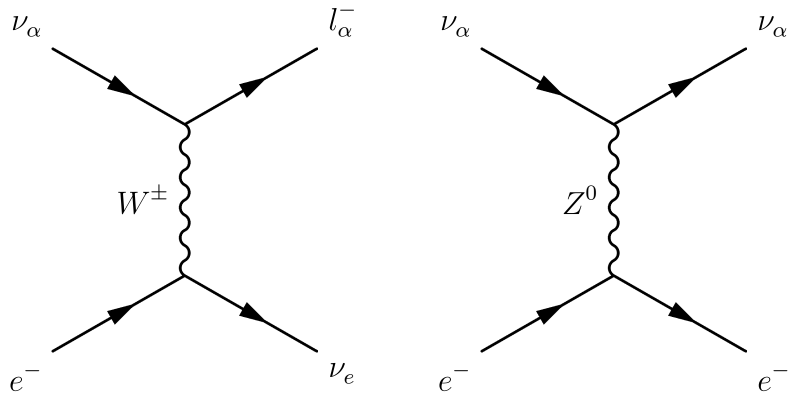

(a) CC ν-e^- Scattering **(b)** NC ν-e^- Scattering

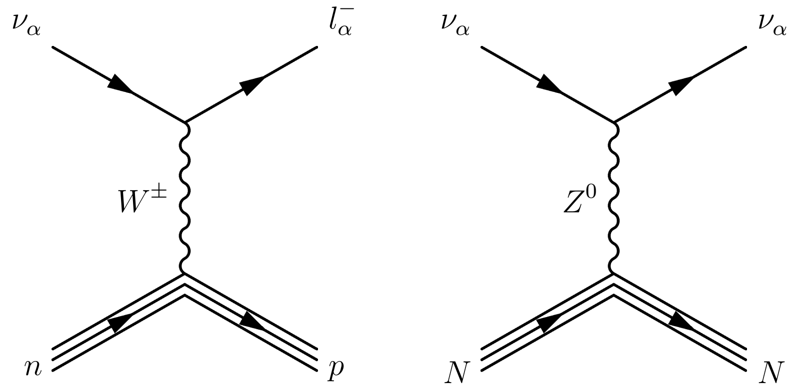

(c) CC ν-N Scattering **(d)** NC ν-N Scattering

Figure 2.2: Two charged current and two neutral current neutrino interactions.

Due to the neutrino's extremely small interaction cross section, large-scale detectors are required to detect their interactions, either scattering off atomic electrons or nucleons. To date there have been only three generations of neutrinos observed directly (ν_e, ν_μ and ν_τ) [6] [7]. Measurements of the Z^0 decay width at LEP [8], as shown in Figure 2.3, have placed strong constraints on the number of light neutrino flavours to three, corresponding to the three flavours of charged leptons [9].

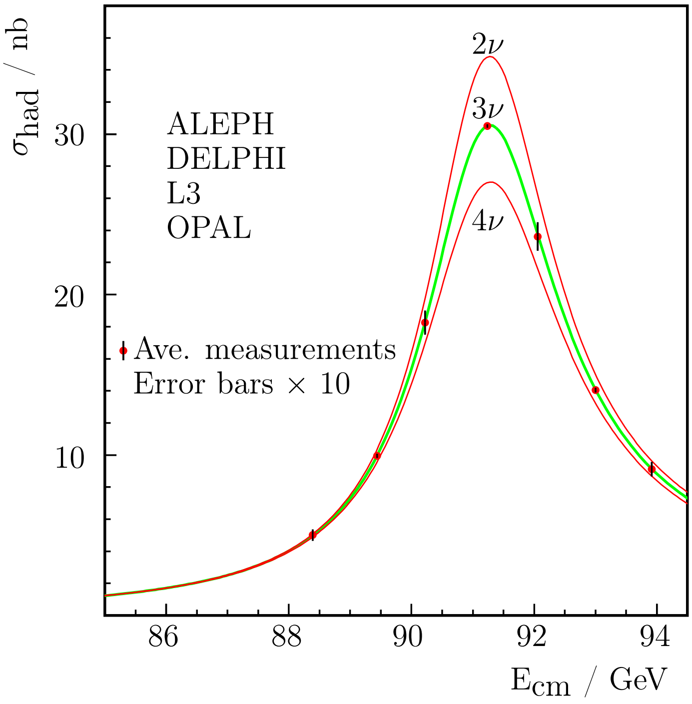

Figure 2.3: Combined LEP cross-section measurements for $e^+e^- \rightarrow$ *hadrons* around the Z^0 resonance. $N_\nu = 3$ is clearly favoured. [9].

The LEP result does not exclude the possibility of the existence of neutrinos with mass greater than $M_{Z^0}/2$ (45.6 GeV) nor neutrinos that do not couple to the Z^0, which are commonly termed *sterile neutrinos*.

All massive fermions in the SM have Dirac mass terms which means there must exist distinct left (LH) and right-handed (RH) chiral fields for each particle so they can couple to the Higgs field and acquire mass. Experimental evidence shows RH neutrinos do not couple to the weak interaction. Therefore, the SM is constructed with only LH neutrinos and RH anti-neutrinos which prevents them from acquiring mass via the Higgs mechanism. The neutrinos of the SM are therefore assumed to be massless travelling at the speed of light.

2.4. Neutrino Mixing and Oscillations

Many neutrino experiments, such as KamLAND [10] and SNO, have observed and confirmed the phenomenon of neutrino oscillations, first postulated by Bruno

Pontecorvo in 1957 [11, 12]. This also solved the three decade old "solar neutrino problem" in which there was a deficit in the number of neutrinos observed to come from the sun. Neutrino oscillations are a result of mixing between neutrino flavour and mass states.

The mixing between neutrino flavours and its associated oscillations can be treated analogously to the mixing in the quark sector through the Cabibbo-Kobayashi-Maskawa (CKM) matrix. The three weak eigenstates of the neutrino (ν_e, ν_μ and ν_τ) are expressed as a superposition of three mass eigenstates (ν_1, ν_2 and ν_3), these are linked by the Pontecorvo-Maki-Nakagawa-Sakata (PMNS) matrix. PMNS $U_{\alpha i}$ is a unitary matrix that defines the neutrino flavour states, $|\nu_\alpha\rangle$ in terms of the neutrino mass states, $|\nu_i\rangle$:

$$|\nu_\alpha\rangle = \sum_i^3 U^*_{\alpha i} |\nu_i\rangle \tag{2.4}$$

where $\alpha = e$, μ or τ and $i = 1$, 2, or 3 the three mass eigenstates. The most common representation of U is shown below:

$$U = \overbrace{\begin{pmatrix} 1 & 0 & 0 \\ 0 & c_{23} & s_{23} \\ 0 & -s_{23} & c_{23} \end{pmatrix}}^{\text{Atmospheric}} \overbrace{\begin{pmatrix} c_{13} & 0 & s_{13}e^{-i\delta} \\ 0 & 1 & 0 \\ -s_{13}e^{i\delta} & 0 & c_{13} \end{pmatrix}}^{\text{Cross-mixing}} \overbrace{\begin{pmatrix} c_{12} & s_{12} & 0 \\ -s_{12} & c_{12} & 0 \\ 0 & 0 & 1 \end{pmatrix}}^{\text{Solar}} D_M \tag{2.5}$$

where $c_{ij} \equiv \cos\theta_{ij}$, $s_{ij} \equiv \sin\theta_{ij}$, θ_{ij} is the mixing angle which determines the degree of mixing between mass states i and j, and δ the CP-violating Dirac phase. Furthermore, if the neutrino is a Majorana particle (Section 2.5.2) then there are additional CP-violating phases, ϕ_1 and ϕ_2, included in the diagonal matrix, D_M:

$$D_M = \begin{pmatrix} 1 & 0 & 0 \\ 0 & e^{i\phi_1} & 0 \\ 0 & 0 & e^{i\phi_2} \end{pmatrix} \tag{2.6}$$

The probability for a neutrino to change from flavour α to β is given by [13]:

$$P\left(\nu_\alpha \rightarrow \nu_\beta\right) = \left|\sum_i U^*_{\alpha i} e^{-im_i^2 \frac{L}{2E}} U_{\beta i}\right|^2 \tag{2.7}$$

where $U_{\alpha,\beta}$ are elements of the unitary PMNS matrices, m_i is the neutrino mass eigenstate, L is the propagation distance, E is the energy of the neutrino. In the simplified two neutrino case, in a vacuum, a neutrino of flavour α has the probability to turn to flavour β given by:

$$P\left(\nu_\alpha \rightarrow \nu_\beta\right) = \sin^2(2\theta_{ij}) \sin^2\left(\Delta m^2_{ij} \frac{1.27L}{E}\right) \tag{2.8}$$

where θ_{ij} is the neutrino mixing angle and m^2_{ij} is the mass splitting between the states i and j defined as:

$$\Delta m^2_{ij} \equiv m_i^2 - m_j^2 \,. \tag{2.9}$$

Therefore, if a neutrino is produced in a weak interaction as a particular flavour with a given energy it will mix between the different flavours as it travels. The oscillation probability is determined by $sin^2(2\theta_{ij})$ and m^2_{ij}, which defines the amplitude and frequency of the oscillation respectively. The oscillation parameters have been measured by several experiments and the results are summarised in Table 2.1. If neutrinos were massless then the probability for neutrino flavour oscillation would be zero.

2.5. Neutrino Mass: Dirac vs Majorana

The clear evidence for neutrinos undergoing flavour mixing and oscillations means they must also have none-zero mass. Therefore, it is reasonable to attempt to add

Oscillation Parameter	Inverted Ordering	Normal Ordering
$\sin^2\theta_{12}$	$0.304^{+0.013}_{-0.012}$	$0.304^{+0.013}_{-0.012}$
$\sin^2\theta_{23}$	$0.452^{+0.052}_{-0.028}$	$0.579^{+0.025}_{-0.037}$
$\sin^2\theta_{13}$	$0.0218^{+0.0010}_{-0.0010}$	$0.0219^{+0.0011}_{-0.0010}$
Δm^2_{21} $(\times 10^{-5} eV^2)$	$7.50^{+0.19}_{-0.17}$	$7.50^{+0.19}_{-0.017}$
Δm^2_{32} $(\times 10^{-3} eV^2)$	$+2.457^{+0.047}_{-0.047}$	$-2.449^{+0.048}_{-0.047}$

Table 2.1: Best current estimates for neutrino mixing parameters from a global fit performed for the inverted and normal mass orderings separately. The parameter $\Delta m^2_{32} > 0$ for normal ordering and $\Delta m^2_{32} < 0$ for inverted ordering [14].

this mass into the SM. However, depending on the nature of the neutrino this could be Dirac mass terms, Majorana mass terms or a combination of both.

2.5.1. Dirac Mass

The minimum extension to the Standard Model, to allow for a massive neutrino, would be to introduce right-handed (RH) neutrinos. These neutrinos do not interact weakly, based on experiments, so are sterile. The Lagrangian for a massive Dirac neutrino is then:

$$\mathcal{L}_D = -m_D\left(\overline{\nu_L}\nu_R + \overline{\nu_R}\nu_L\right) + \text{h.c.} \tag{2.10}$$

where m_D is a constant mass term that represents the Yukawa coupling between the neutrino and Higgs fields, and h.c. is the Hermitian conjugate. The Dirac mass construction requires four independent components where:

$$\nu = \nu_L + \nu_R, \qquad \bar{\nu} = \bar{\nu}_L + \bar{\nu}_R \tag{2.11}$$

therefore neutrinos and anti-neutrinos are fundamentally different particles. As both incoming and outgoing particles are neutrinos, lepton number is conserved. Although this method requires only a small extension to the SM, it is rather unsatisfactory. It introduces a sterile neutrino which cannot be observed experimentally and contrives an extremely small Higgs-neutrino Yukawa coupling in a deus ex machina fashion.

2.5.2. Majorana Mass

Since the neutrino is neutral it does not need to conserve charge. It is therefore possible to introduce a Majorana mass term, first proposed by Ettore Majorana in 1937 [15], which only requires two independent components and can be constructed from only the right-handed (or left-handed) neutrino field. The Lagrangian for a massive Majorana neutrino is then:

$$\mathcal{L}_M = -\frac{1}{2} m_M \overline{\nu_R^c} \nu_R + \text{h.c.} \tag{2.12}$$

$$\nu_R^c = C\nu_R \equiv i\gamma^2 \nu_R \tag{2.13}$$

where m_M is the Majorana mass matrix and h.c. is the Hermitian conjugate. A factor $1/2$ is introduced to avoid double counting since ν_R^c and ν_R are not independent of each other. The two components are:

$$\nu = \nu_L + \nu_L^C, \qquad \nu^C = \nu \tag{2.14}$$

The incoming neutrino is changed to an outgoing anti-neutrino therefore, lepton number is no longer a conserved quantity. The Majorana case removes the need for 4 neutrinos of which 2 are sterile as is the Dirac case. A Majorana neutrino would mean the PMNS matrix could have two independent CP violating phases resulting in an additional source of CP violation within the Standard Model. If CP violation can be observed in the lepton sector it can explain the matter-antimatter asymmetry of the universe through a process called leptogenesis.

2.5.3. See-Saw Mechanism

One possible way to explain away the significantly smaller neutrino mass is to combine the Dirac and the Majorana mass terms into a single Lagrangian.

$$\begin{aligned}\mathcal{L}_{See-Saw} &= -\frac{1}{2}m_D\left(\overline{\nu_L}\nu_R + \overline{\nu_R}\nu_L\right) - \frac{1}{2}m_M\overline{\nu_R^c}\nu_R + \text{h.c.} \\ &= -\frac{1}{2}\begin{pmatrix}\overline{\nu_L} & \overline{\nu_R^c}\end{pmatrix}\mathcal{M}\begin{pmatrix}\nu_L^c \\ \nu_R\end{pmatrix} + \text{h.c.} \qquad (2.15)\end{aligned}$$

where $\mathcal{M}$ is given by:

$$\mathcal{M} = \begin{pmatrix}0 & m_D \\ m_D & m_M\end{pmatrix} \qquad (2.16)$$

The neutrino states in Equation (2.15) are weak eigenstates, so $\mathcal{M}$ must be diagonalised to find the the mass eigenstates. From Equation (2.16), $\mathcal{M}$ has eigenvalues:

$$m_{1,2} = \frac{1}{2}m_R \pm \frac{1}{2}\sqrt{m_R^2 + 4m_D^2}\,. \qquad (2.17)$$

In this model, for the charged fermions, the Dirac masses are the physical masses so it is assumed that m_D is of the same order of magnitude as the other related fermions. The Majorana mass, m_M, is at the Grand Unification Theory (GUT) scale ($\sim 10^{16}$ GeV). In this scenario, where $m_M \gg m_D$, the two eigenvalues of Equation (2.17) can be approximated as:

$$m_1 \approx m_M \qquad (2.18)$$

$$m_2 \approx \frac{m_D^2}{m_M} \qquad (2.19)$$

This mechanism therefore assumes the neutrino to be a Majorana particle as the Majorana mass term appears in both eigenvalues. It can also be seen how the mechanism gained its name, as larger m_M results in larger m_1 and smaller m_2. Therefore, a GUT scale heavy right-handed neutrino of mass 10^{16} GeV leads to light left-handed neutrinos in the meV scale.

2.6. Double Beta Decay

The $0\nu\beta\beta$ decay is the most sensitive and perhaps the only practical way to probe whether neutrinos are Dirac or Majorana fermions as well as providing complementary information to cosmology, oscillation experiments to measure the absolute neutrino mass, and the mass hierarchy. The observation of $0\nu\beta\beta$ decay would be unambiguous evidence of lepton number violation which is required by theories of leptogenesis and baryogenesis to explain the matter-antimatter asymmetry of the universe and is also a requirement of almost every single GUT model. Therefore, the observation of $0\nu\beta\beta$ decay would have a profound impact on the field of particle physics and beyond.

2.7. Two Neutrino Double Beta Decay

The theory of $2\nu\beta\beta$ was first proposed by Goeppert-Mayer [16] in 1935. The process has two neutrons simultaneously decaying to two protons, emitting two electrons and two electron anti-neutrinos:

$$2n \rightarrow 2p + 2e^- + 2\bar{\nu}_e\,. \tag{2.20}$$

This is a second order electroweak interaction where the two emitted anti-neutrinos conserve lepton number, see Figure 2.4. This is a Standard Model process which was first observed in 1950 by Inghram and Reynolds [17] in a geochemical experiment. The observation of $2\nu\beta\beta$ was subsequently confirmed using a direct counter experiment in 1987 with enriched ^{82}Se [18].

All β decay processes involve a loss of energy, so β decay can only occur if:

$$M(A, Z_i) > M(A, Z_f) \tag{2.21}$$

where $M(A, Z)$ is the mass of the nucleus with A nucleons and Z protons, and i and f denote the initial and final nuclear states.

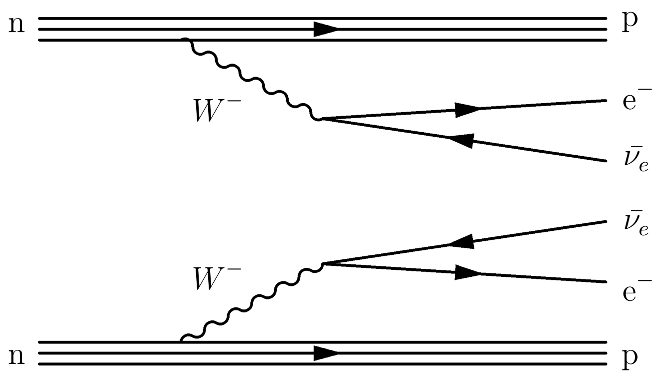

Figure 2.4: Feynman diagram for $2\nu\beta\beta$, a second order SM process.

For the double beta decay process to occur, single beta decay has to be highly suppressed energetically. Normal beta decay is energetically forbidden for a nucleus with atomic number Z if the mass of the daughter nucleus (with atomic number $Z + 1$ for β^- decay) is greater than that of the parent, see Figure 2.5. For double beta decay the daughter nucleus has atomic number $Z \pm 2$, hence for double beta decay to be allowed there must be a suitable nucleus with $Z \pm 2$ and with a lower binding energy.

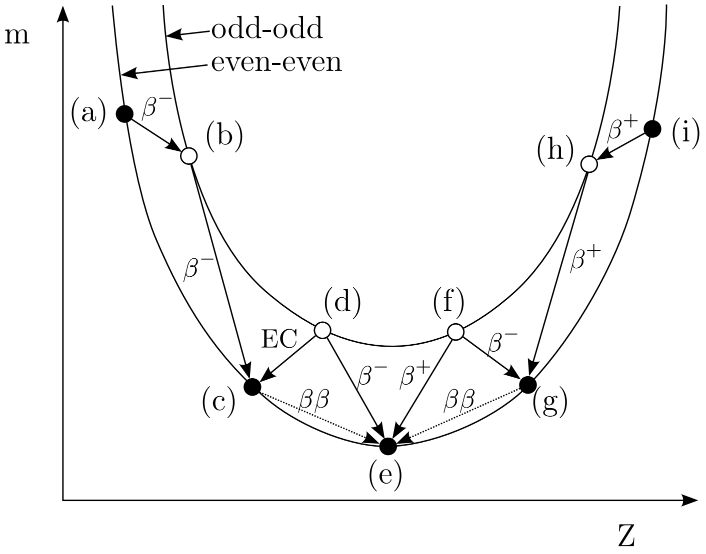

Figure 2.5: The two parabolas showing energetically allowed beta and double-beta decays for an arbitrary decay chain, where (e) is stable with the lowest mass, the transition (c) → (d) is energetically forbidden as the mass of (d) is greater than that of (c) and double beta decay allows the transition of (c) → (e) [19].

It is clear from Figure 2.5 that $2\nu\beta\beta$ can only occur for even-even nuclei since odd-odd nuclei will predominantly decay via β decay to an even-even state.

The half-life of the $2\nu\beta\beta$ can be calculated using;

$$\left(T^{2\nu}_{1/2}(A,Z)\right)^{-1} = |M_{2\nu}(A,Z)|^2 \times G^{2\nu}(Q,Z) \tag{2.22}$$

where;

$M_{2\nu}$ - Nuclear Matrix Element (NME)
$G^{2\nu}$ - phase space factor for the $2\nu\beta\beta$ process (can be calculated exactly).

The NME calculations are heavily model-dependent, see Section 2.9, so experimental information is crucial to improve the models. Precise experimental measurements of $2\nu\beta\beta$ for various isotopes can help constrain theoretical calculations of the NME as they are related via Equation (2.22). Since $2\nu\beta\beta$ decay requires simultaneous decay of two nuclei, in the same atom, it is an extremely rare event with a half-life of 10^{18} to 10^{24} years depending on the NME and the phase space factor of the decay isotope.

Experiments measure the spectrum of the total energy of the emitted electrons to identify the $2\nu\beta\beta$ decay process. Since the neutrinos carry away part of the energy, the energy of the emitted electrons is a continuous spectrum with an end-point at the nuclear transition energy, $Q_{\beta\beta}$, which is the total energy released in the decay:

$$Q_{\beta\beta} = M(A,Z) - M(A,Z+2)\,. \tag{2.23}$$

The shape of this spectrum can be seen in Figure 2.6.

2.8. Neutrinoless Double Beta Decay

The $0\nu\beta\beta$ is a hypothetical nuclear decay process where two neutrons decay simultaneously into two protons, emitting two electrons only, as shown in Figure 2.7. It was

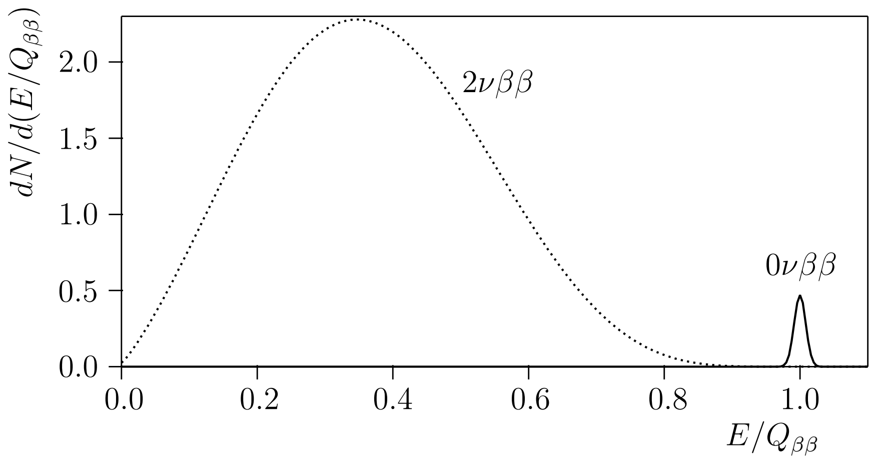

Figure 2.6: Spectrum of summed electron energy of double-β decay showing $2\nu\beta\beta$ and $0\nu\beta\beta$ decay with resolution effects of 2% taken into consideration. The decay rate of $0\nu\beta\beta$ is taken as 1% of the $2\nu\beta\beta$ rate [20].

first proposed in 1939 by W.H. Furry [21] and it is a process forbidden by the SM due to lepton number violation.

$$2n \rightarrow 2p + 2e^- \, . \tag{2.24}$$

This process is possible for all double-β isotopes. The $0\nu\beta\beta$ half-life is given by;

$$\left(T^{0\nu}_{1/2}(A,Z)\right)^{-1} = m^2_{\beta\beta} \cdot |M_{0\nu}(A,Z)|^2 \cdot G^{0\nu}(Q,Z) \, . \tag{2.25}$$

Where $m_{\beta\beta}$ is the effective Majorana mass of the electron neutrino:

$$m_{\beta\beta} = \left| \sum_i U^2_{ei} \, m_i \right|^2 \tag{2.26}$$

where U_{ei} are elements of the neutrino mixing matrix and m_i are the neutrino mass eigenstates. The $m_{\beta\beta}$ parameter depends on the underlying $0\nu\beta\beta$ decay mechanism. Measurement of $m_{\beta\beta}$ also allows $0\nu\beta\beta$ to determine the neutrino mass hierarchy as it depends on the relative masses of the neutrino flavours [22]. The current limits on the half-lives of this process are of the order of 10^{25} yr.

If observed, the result would provide further evidence of physics beyond the SM and support many Grand Unification theories (GUT), such as described in Section 2.5.3, where total lepton number violation is a requirement. This could also give a mechanism to explain the matter/anti-matter asymmetry in the present universe.

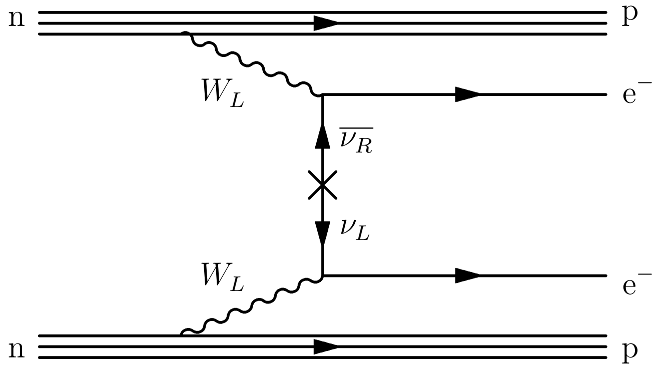

Figure 2.7: Feynman diagram from $0\nu\beta\beta$ for the neutrino mass mechanism. The decay is facilited by the exhange of a Majorana neutrino.

The process shown in Figure 2.7 is of the Mass Mechanism, or light neutrino exchange mechanism, the most widely discussed mechanism for $0\nu\beta\beta$ decay [23]. It requires the least modification to the SM, involving a light RH (ν_R) Majorana neutrino which undergoes a helicity flip to be absorbed as a light LH Majorana neutrino. There is an inherent dependence of the decay rate on the effective mass due to it requiring a helicity flip.

Other mechanisms also exist such as; V+A currents, Majoron emission, R-parity violating SUSY etc [20]. The SuperNEMO detector technology is unique in being able to provide 3D reconstruction of the process and hence a means by which to distinguish one mechanism from the others [24]. If nature is kind and the hierarchy is inverted then there are real prospects for either observing or excluding $0\nu\beta\beta$, mediated via the Mass Mechanism, in the coming decade.

2.9. Nuclear Matrix Elements

To convert measured $T^{0\nu}_{1/2}$ to the physics parameter of interest ($\langle m_{\beta\beta} \rangle$), the appropriate NME is required. Since the phase space can be calculated with relative precision, the accuracy with which NMEs can be calculated directly impacts the interpretation of any experimental result.

NME calculations require the many-body Schrödinger equation to be solved, accounting for each nucleon-nucleon interaction, given the total initial and final state nuclear wave functions. Due to the complexity of the calculations, various approximations and simplifications have to be made [23].

Until now there are five techniques which have been used to determine the NME, all involving a two step process. Firstly, create a many-body Hamiltonian to describe the nucleon-nucleon interactions at short distances and encompass known nuclear physics. Secondly, construct the many body wave functions which incorporates the information about the nuclear structure and residual interactions. It is primarily at this second step where the techniques differ with respect to their approximations of the interaction Hamiltonian, treatment of nucleon correlations and the construction of the single particle wave functions.

2.9.1. Interacting Shell Model

The interacting shell model (ISM) [25] is based on a complete description of a limited number of nuclear orbitals close to the Fermi level, but all possible correlations for these orbitals are included. This method tends to produce smaller than average values for the NME, compared to other approximations, which may be due to the small number of orbits being considered.

The ISM has calculated the NME for several nuclei. However, it is known the ISM is useful for calculating single particle states close to the Fermi level and has difficulty for calculations of deformed nuclei, such as ^{150}Nd, and heavy isotopes. Instead, the ISM produces more reliable results for smaller nuclei such as ^{48}Ca, ^{76}Ge and ^{82}Se.

2.9.2. Quasiparticle Random Phase Approximation

Complementary to the ISM, the quasiparticle random phase approximation (QRPA) [26] takes a different approach which is better suited for larger nuclei. In this method the number of different nuclear orbitals included is greatly increased, but the complexity of the interactions between nucleons is limited. The Hamiltonian describing the nucleus is modified based on experimental inputs. It has been shown that $2\nu\beta\beta$ results can be used to tune the g_{pp} parameter, which describes proton-proton interactions, this significantly reduces uncertainties associated with QRPA calculations.

2.9.3. Interacting Boson Model

The interacting boson model (IBM) [27] is similar to the ISM and shares similar advantages and disadvantages. It models the low-lying nuclear states as bosons in states with L=0 or 2 (s and d boson states respectively). Therefore only 0^+ and 2^+ neutron pairs can turn into two protons in $0\nu\beta\beta$.

2.9.4. Projected Hartree-Fock-Bogoluibov Method

In the projected Hartree-Fock-Bogoluibov (PHFB) [28] model, nuclear wave functions describing the double-β decay in medium and heavy mass nuclei are constructed by projecting a set of states with good angular momentum, while treating the pairing and deformation degrees of freedom simultaneously, on the HFB wave functions. The nuclear Hamiltonian is simplified to include only quadrupole interactions. It only describes neutron pairs with even angular momenta and positive parity (0^+, 2^+, 4^+ etc.). Although non-0^+ pairs are heavily suppressed compared to other calculations.

2.9.5. Energy Density Functional Method

The energy density functional (EDF) [29] method is similar to the QRPA since all intermediate single particle states are available. It is considered to be an improvement to the PHFB method where the inter-nucleon interaction is modified to reproduce the Gogny interaction.

2.9.6. Comparison of different NME calculations

The difference between the NME of the 11 possible $0\nu\beta\beta$ isotopes in the mass mechanism, calculated using the five methods described previously, are shown in Figure 2.8. The result presented in Figure 2.8 has been normalised for g_A and r_0, the axial vector coupling constant and nuclear radius respectively. This was necessary as there is current disagreement among theorists with regards to the strength of g_A which has to be adjusted to fit the experimentally measured $2\nu\beta\beta$ half-lives. The value for r_0 can also vary from 1.1 to 1.2 fm.

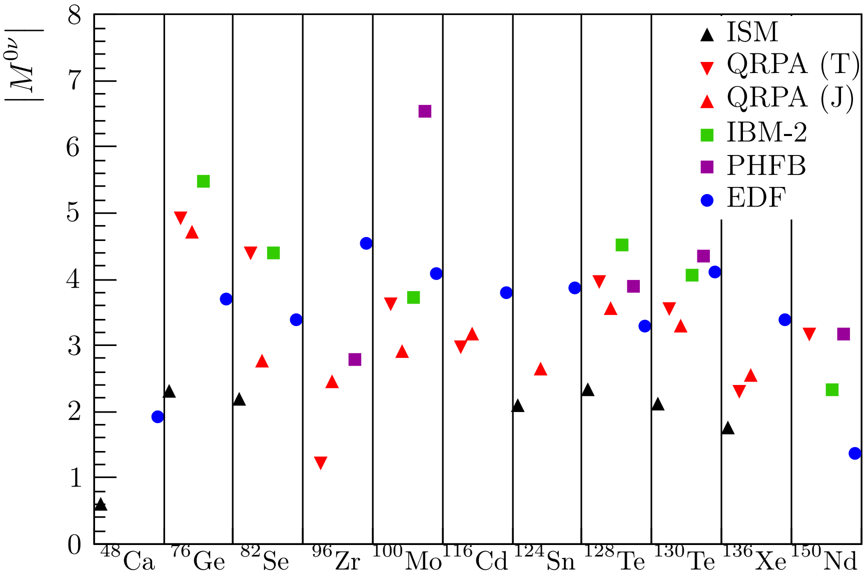

Figure 2.8: Comparison of NME, for the neutrino mass mechanism, calculated by various groups using the five different techniques. The results QRPA (T) and QRPA (J) show the results obtained, using the same technique, by the Tübingen-Bratislava-Caltech group and Jyväskylä group respectively. The $\left|M^{0\nu}\right|$ values are taken from [23]. All results have been normalised to $g_A = 1.25$ and $r_0 = 1.2$ for the purpose of direct comparison [19].

These techniques, in most cases, produce results which are a factor 2-3 times different to each other which is problematic. Even the results of two groups using the same technique produced different results. This variation translates directly into an uncertainty in the obtained $0\nu\beta\beta$ decay limits.

2.10. Current Constraints

The neutrino mass is constrained by experimental results from four different areas of physics. Neutrino oscillation experiments have accurately measured squared mass differences placing a lower bound on the neutrino mass. While tritium decay, $0\nu\beta\beta$ decay and cosmology have placed upper limits on the neutrino mass.

2.10.1. Oscillations Experiments

Although neutrino oscillation experiments are not able to determine the absolute neutrino mass, precise measurement of the largest mass splitting, $|\Delta m^2_{23}|$, can still provide a lower bound on the neutrino mass. Since the lightest mass state cannot be less than zero, at least one of the mass state must have mass > 0.05 eV.

2.10.2. Tritium Decay Experiment

The electron neutrino mass can be measured by measuring the single beta decay spectrum endpoint with high energy resolution. Tritium is the most popular candidate as it has a low Q_β and a simple atomic structure. Tritium experiments measure the decay process:

$$^3\mathrm{H} \rightarrow {}^3\mathrm{He} + \mathrm{e}^- + \overline{\nu_e}\,. \tag{2.27}$$

A massive neutrino must always carry away a minimum energy equivalent to its mass which will affect the tail of the decay spectrum due to the amount of energy available to the emitted electron compared to the massless case, as shown in Figure 2.9. The main advantage of this type of experiments is that they rely only on energy and momentum conservation to extract $\langle m_\beta \rangle$ and hence are model independent. The current world best limit of ν_e mass comes from a combination of Mainz and Troitsk experimental results with a value of $\langle m_\beta \rangle < 2.0$ eV (95% CL) [30–32].

A new tritium experiment called KATRIN is due to start data taking in 2017 and aims to reach a sensitivity of 200 meV (90% CL) and a 5σ discovery potential of 350 meV [34].

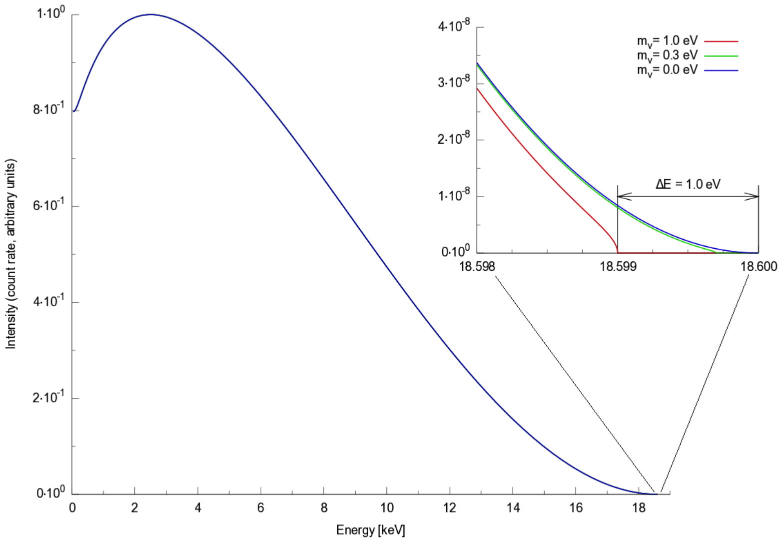

Figure 2.9: Electron energy spectrum for tritium decay, showing exaggerated distortion in the high energy tail due to neutrino of mass 30 eV [33].

2.10.3. Cosmology

Similar to the cosmic microwave background (CMB) it is predicted there should be a evenly distributed sea of cosmic neutrino background (CNB) sometimes referred to as relic neutrinos. The number density of this CNB is predicted by cosmological models and plays an important role in the evolution of the universe. Through large scale surveys of cosmological observables; such as anisotropies in the cosmic microwave background (CMB), baryon acoustic oscillations and large scale structure formation, constraints can be placed on the sum of the neutrino masses. Many observables are often combined to place stronger limits on the sum of neutrino mass, but this then becomes heavily model dependent.

The current best limits from cosmology are: $\sum m_i < 0.2 - 1.3$ eV (95% CL) [35] depending on the assumed cosmological parameters.

2.10.4. Neutrinoless double beta decay ($0\nu\beta\beta$)

The current world leading limit, from laboratory experiments, on the upper bound of the neutrino mass comes from $0\nu\beta\beta$ decay experiments. This limit is only valid if neutrinos are indeed Majorana particles and therefore able to undergo the $0\nu\beta\beta$ decay processes. The current best limit comes from the combined results of the Kamland-Zen and EXO experiments in ^{136}Xe, with a value of $\langle m_{\beta\beta} \rangle < 61-165$ meV (90% CL) [36]. The range in neutrino mass is a result of uncertainties in the NME calculations.

2.10.5. Current Landscape

A summary of the current leading constraints from each field of physics is presented in Table 2.2.

Parameter	Value	Source
$\langle m_\beta \rangle$	< 2 eV (95% CL)	Tritium Decay [31,32]
$\sum m_i$	$< 0.2 - 1.3$ eV (95% CL)	Cosmology [35]
$\langle m_{\beta\beta} \rangle$	$< 0.061 - 0.165$ eV (90% CL)	$0\nu\beta\beta$ [36]
m_1 or m_3	> 0.05 eV (68% CL)	Oscillations [30]

Table 2.2: The most competitive constraints on neutrino mass for four different types of experiment.

The constraints are included in a plot of the phase space for $\langle m_{\beta\beta} \rangle$ as a function of the lightest neutrino mass m_{light}, as shown in Figure 2.10. The $0\nu\beta\beta$ search is dependent on the ordering of the neutrino masses. The $\langle m_{\beta\beta} \rangle$ is constrained by the latest $0\nu\beta\beta$ results while m_{light}, is constrained by the most recent results of the Planck experiment. The two distinct bands represent the normal and inverted hierarchies. The width of each band is determined by the uncertainty over the CP-violating phases (ϕ_1 and ϕ_2) as shown in Equation (2.6).

2.11. Outstanding questions

There has been remarkable progress made in the field of neutrino physics since the discovery of neutrino oscillation. However, there remain many open questions to be resolved by current and next generation oscillation, tritium decay, cosmology and $0\nu\beta\beta$ experiments. A summary of outstanding neutrino questions and the experimental approaches designed to answer them are shown in Table 2.3.

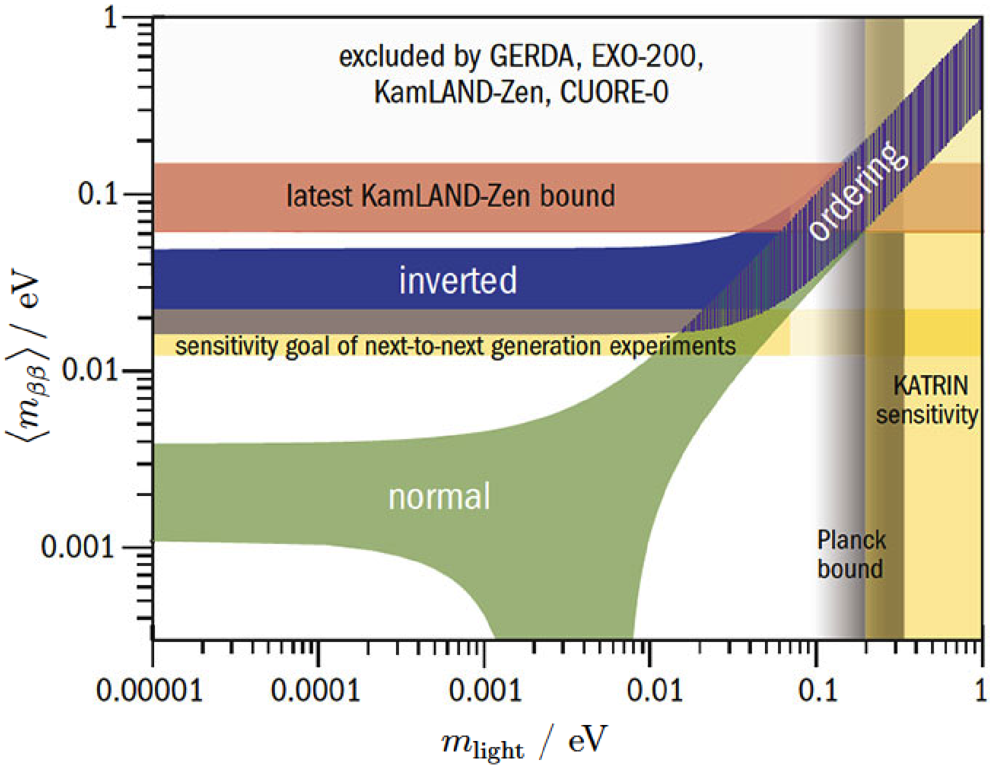

Figure 2.10: Plot showing the effective Majorana mass parameter $\langle m_{\beta\beta} \rangle$ related to the decay rate as a function of the lightest neutrino mass, with best fit values of the oscillation parameters, for normal hierarchy (green) and inverted hierarchy (blue).The latest results from $0\nu\beta\beta$ decay and cosmology as well as the anticipated KATRIN sensitivity are shown [37].

2.11.1. Number of neutrinos

There are currently three known light neutrino flavours as discussed in Section 2.3, with the possibility of one or more sterile neutrinos. There has been some experimental hints of a sterile neutrino from experiments such as LSND, MiniBoone along with reactor anomolies, however there has yet to be any concrete evidence. Experiments such as MicroBooNE and next generation short baseline reactor measurements could provide some answers.

Property	Oscillation	Cosmology	β-decay	$0\nu\beta\beta$
Number of Neutrinos	✓	✓		
Absolute Mass		✓	✓	✓
Mass Hierarchy	✓	✓		✓
Dirac or Majorana				✓
Dirac CP-violation	✓			
Majorana CP-violation				✓

Table 2.3: Outstanding questions of neutrino properties and experimental techniques to answer them.

2.11.2. Absolute Mass

The current and next generation of cosmology, tritium decay and $0\nu\beta\beta$ experiments will continue to try and determine the absolute neutrino mass. If neutrinos are Majorana particles $0\nu\beta\beta$ decay experiments are in the best position to probe masses down to 30 meV over the coming decade. It will be technically difficult to improve on the predicted KATRIN limit using tritium decay experiments in the near future due to the scale and quality of spectrometer required.

2.11.3. Mass Hierarchy

Neutrino oscillation experiments have accurately measured $|\Delta m_{12}^2|$ which shows $m_1 < m_2$. This gives rise to two possible scenarios where $m_1 < m_2 < m_3$, known as the normal hierarchy (NH) and $m_3 < m_1 < m_2$, known as the inverted hierarchy (IH). Future oscillation experiments will try to measure the sign of Δm_{32}^2 to determine if the mass hierarchy is normal or inverted.

2.11.4. CP Violation

Since CP violation has been observed in the quark sector, the question arises as to if this is the case in the leptonic sector. The PMNS mixing matrix contains at least one Dirac CP-violating phase and two more if neutrinos are Majorana particles. The answer to this could provide essential information to the matter anti-matter

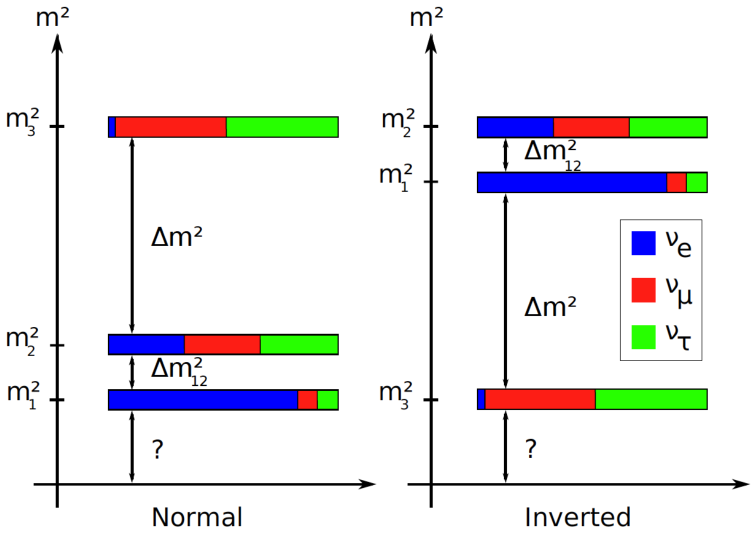

Figure 2.11: The "normal" and "inverted" mass hierarchies of absolute neutrino masses.

asymmetry in the present day universe which CP-violation in the quark sector alone is not enough to account for.

The Dirac CP-violating phase can be measured in accelerator or atmospheric neutrino experiments [38]. However, the Majorana CP-violating phase can only be measured through $0\nu\beta\beta$ decay experiments.

2.11.5. Dirac or Majorana

The only way to determine if neutrinos are fundamentally Dirac or Majorana particles is through $0\nu\beta\beta$ decay experiments. The current and next generation experiments will completely explore $\langle m_{\beta\beta}\rangle$ of the IH. However, there is no present design which is capable to reach $\langle m_{\beta\beta}\rangle$ if the mass hierarchy is normal.

To observe $0\nu\beta\beta$ decay would confirm lepton number violation, however, it can occur through various mechanisms other than the mass mechanism [39]. In these cases the lepton number violating parameter is not directly related to the neutrino mass and the double-β decay half-life will not provide direct information on the neutrino mass. Experiments which can reconstruct event topology (see Section 3.2.5) have an improved ability to distinguish between mechanisms.

Chapter 3.

Current Status of $\beta\beta$ Decay Experiments

A large variety of experiments using different techniques have probed $0\nu\beta\beta$ half life over the past decades, without observation, setting ever more stringent limits. These experiments have improved the $2\nu\beta\beta$ decay half-life measurement.

It is possible to approximately parametrise the expected half-life sensitivity of any given experiment using the following expression [20]:

$$T^{0\nu}_{1/2} \propto a \cdot \epsilon \cdot \sqrt{\frac{Mt}{\Delta E \cdot N_B}} \tag{3.1}$$

where

- $T^{0\nu}_{1/2}$ is the half-life sensitivity to $0\nu\beta\beta$ in years
- ϵ is the event detection and identification efficiency
- a is the isotopic abundance of the $0\nu\beta\beta$ source isotope in the source mass
- ΔE is the energy resolution
- Mt is the total exposure of the experiment in kg yr
- N_B is the number of expected background events for the exposure

This can be taken as an approximate figure of merit for defining sensitivities.

3.1. Experimental Considerations

The modern and future generations of $0\nu\beta\beta$ decay detectors must not only increase in size but must also be optimised in design in order to reach the sensitivities required to probe lower neutrino mass. The main ingredients necessary for such a detector are listed below.

3.1.1. Isotope

There are 35 naturally occurring isotopes which can undergo the $2\nu\beta\beta$ decay process of which only 12 have been observed. The choice of isotope for an experiment is extremely important with the following considerations.

- High isotope Q value: reduces possible backgrounds both $2\nu\beta\beta$ and natural radioactivity.
- Natural abundancy and ease of enrichment: increases the mass of $0\nu\beta\beta$ source.
- Phase space: must be as high as possible.
- NME: must be as high as possible.

The full list of $2\nu\beta\beta$ isotopes, their natural abundance, and enrichment methods are summarised in Table 3.1. For the majority of isotopes enrichment via centrifugation is possible which is relatively low cost compared with electromagnetic separation, which is currently the only way to enrich ^{48}Ca, ^{96}Zr and ^{150}Nd.

3.1.2. Radio-purity

The detector background usually increases linearly with mass and exposure time, hence the sensitivity of experiments is proportional to $\sqrt{Mt}$. It is therefore crucial to minimise background activity. Uranium and thorium are the dominant backgrounds for any rare event search experiments, their daughter isotopes ^{214}Bi and ^{208}Tl respectively are of particular concern for $0\nu\beta\beta$ decay experiments. They have decay Q values ($Q_\beta(^{214}\text{Bi})=3.27$ MeV and $Q_\beta(^{208}\text{Tl})=4.992$ MeV) high enough to mimic a $0\nu\beta\beta$ event.

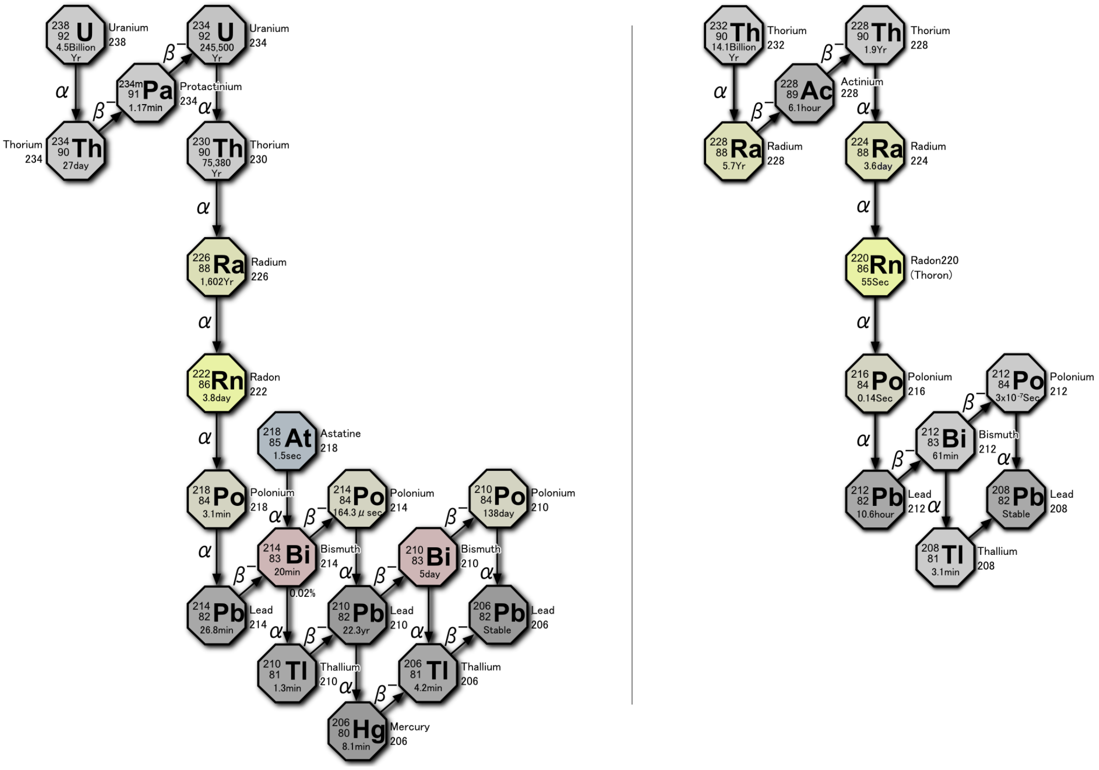

Figure 3.1: (Left) The decay chain for ^{238}U [41]. (Right) The decay chain for ^{232}Th [42].

Isotope	$Q_{\beta\beta}$ keV	$G^{0\nu}$ 10^{-14} yr^{-1}	NA %	Enrichment Possibilities Current Method	R&D Method(s)
^{48}Ca	4276	7.15	0.187	EMS	Laser Separation, Gaseous Diffusion
^{76}Ge	2039	0.71	7.8	Centrifugation	–
^{82}Se	2992	3.11	9.2	Centrifugation	–
^{96}Zr	3348	5.63	2.8	EMS	Laser Separation
^{100}Mo	3034	5.03	9.6	Centrifugation	–
^{116}Cd	2804	5.44	7.6	Centrifugation	–
^{130}Te	2529	4.89	34.5	Centrifugation	–
^{136}Xe	2467	5.13	8.9	Centrifugation	–
^{150}Nd	3368	23.2	5.6	EMS	Laser Separation, Centrifugation

Table 3.1: Details of isotopes commonly used in double-β decay experiments, showing Q-value, phase space factor, natural abundance (NA) and possibilities for enrichment. EMS is electromagnetic separation. $G^{0\nu}$ is calculated with $g_A = 1.25$ and $R = 1.2\ A^{1/3}$ fm [23, 40].

To reduce backgrounds, the detector must be constructed from extremely radio-pure materials surrounded by layers of external shielding. The only way to achieve this is to screen all the detector construction materials for radio-purity and select only those with the lowest levels of ^{238}U and ^{232}Th. To achieve sensitivities capable of exploring the inverted mass hierarchy detector materials would need to be of the order of µBq/kg level.

If all background events can be removed then the sensitivity has the advantage of scaling linearly with mass and exposure time.

3.1.3. Location

A major source of backgrounds for rare event search experiments comes from space. So when building a $0\nu\beta\beta$ decay experiment, it is essential to locate the detector underground to ensure suppression of cosmic backgrounds, such as muons, to 10^{-7} of that at the surface. A list of underground laboratories are shown in Figure 3.2.

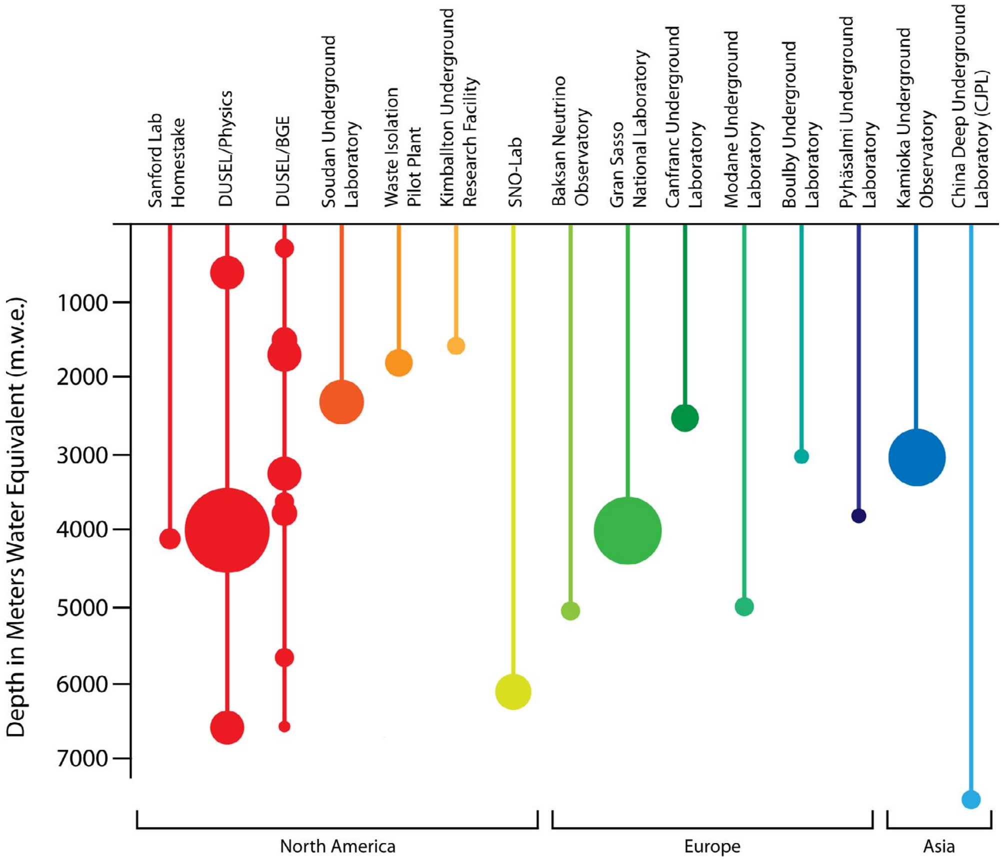

Figure 3.2: Underground laboratories of the world and their respective depth in meters water equivalent (m.w.e.) and volume as defined by the size of the circles [43].

Some low background experiments, such as Majorana employing ^{76}Ge, have gone to the extreme of electroforming copper shielding components underground to avoid cosmogenic activation.

3.1.4. Shielding

In addition to building detectors out of radio-pure material, the best way to reduce detector background is to provide additional shielding from external sources. These can range from cosmic muons to the surrounding environment housing the detector. Rare event search detector shielding are often constructed in Russian doll style layers, with radio-purity requirements increasing with each layer.

- Environmental shielding: provides radiation protection from the laboratory walls and materials, usually 10s of cm thickness.
  - Outer lead shield
  - Inner radio-pure lead shield
  - Ultra pure copper shield
  - Additional water shielding to remove neutrons
- Detector shell: protection from the radiation from the environmental shielding. Housing for the most radio-pure internal detector.
  - Constructed from ultra pure materials
  - Provides radon barrier
  - Containment for detector
- Fiducial self shielding: use part of the radio-pure detector to provide additional shielding from the detector shell.

There still exist backgrounds which cannot be shielded against, such as B^8 solar neutrinos, which scales linearly with detector mass. Current detectors are not yet sensitive to this source of background, however it could pose an irreducible background for future generation experiments.

3.1.5. Energy Resolution

In a perfect world the ideal detector would have perfect energy resolution and be background free. If this can be achieved, the observation of a single event would qualify as a discovery and the corresponding half-life can be determined by counting the number of events with time.

Since the $0\nu\beta\beta$ decay signature is very narrow, a good resolution detector, $< 1\%$ (FWHM), can allow a narrow signal window and therefore further reducing background events. Even if it were possible to build a completely radio-pure detector with perfect shielding, the $2\nu\beta\beta$ decay would still contribute as a irreducible background with typical half-lives of $10^{18} - 10^{19}$ yr. Good energy resolution is therefore required to prevent background events from obscuring the signal.

3.1.6. Scalability

Modern $0\nu\beta\beta$ experiments are probing ever increasing half-life times. However, there is a diminishing gain as a function of exposure time as the achievable sensitivity flattens. Therefore, the ability to easily scale up the isotope mass is essential in order to reach higher sensitivities to further probe neutrino mass regions of interest.

3.1.7. Event Topology

The ability to differentiate background events from signal provides a powerful handle on detector backgrounds. This can range from simple separation of electrons and alphas to full reconstruction of event topology, the later offering a powerful way for background rejection as well as the ability to study the process. Given the current generation material screening capability there is a limit on the selection of radio-pure materials, particle tracking may be the only way to further reduce background levels.

3.2. Experimental Techniques

The various considerations to optimise half-life sensitivity means there is no perfect recipe for constructing a $0\nu\beta\beta$ experiment as some factors are inversely related, whereby improving one may require the sacrifice of another. The cost and R&D required for these improvements are also not trivial. This has resulted in an exciting array of experiments using different approaches to compete for observation. The advantages and disadvantages of each experimental design will be discussed.

3.2.1. Scintillator Experiments

The $0\nu\beta\beta$ decay isotope is placed into the scintillating material which is relatively cheap and radio-pure. The sample is then surrounded with PMTs to observe the light emitted when the decay product of the $0\nu\beta\beta$ isotope excites the scintillation material.

There are two methods for designing a scintillation experiment, the first of which is where the isotope is mixed directly into a large volume of liquid scintillator. This method has the advantage of achieving high isotope mass (^{136}Xe, ^{130}Te or ^{150}Nd), abundance with good detection efficiency, self-shielding due to the large volume and low background. However, it suffers from a poor energy resolution. The two major experiment using this design are the SNO+ experiment using ^{130}Te and the KamLAND-Zen experiment with ^{136}Xe.

- **SNO+** plans to load ^{130}Te doped liquid scintillator into the existing SNO neutrino detector. The detector is located within the Sudbury Neutrino Observatory, 2 km underground, near Sudbury, Canada. It is one of the world's deepest underground laboratory at 6000 m.w.e. The doped scintillator will be contained within an acrylic sphere, 12 m in diameter and 5.5 cm thickness, which is then suspended in the centre of the detector surrounded by 9500, 8 inch, PMTs. This is further enclosed within 5700 tonnes of water as an external shielding. The walls of the cavern where the detector is located has also been lined with a material to prevent radon diffusion.

  The ^{130}Te load will be 0.3%, for the initial phase, within a scintillation solution: LAB (Linear AlkylBenzene). This is equivalent to 800 kg of $0\nu\beta\beta$ isotope reaching an estimated sensitivity of $\langle m_{\beta\beta} \rangle < 50 - 100$ meV. If successful the concentration will be increased to 3%, 8000 kg of ^{130}Te, pushing the sensitivity down to levels of $\langle m_{\beta\beta} \rangle < 20 - 40$ meV [44].

- **KamLAND-Zen** similarly plans to load ^{136}Xe doped liquid scintillator into the existing KamLAND neutrino detector. This is contained within a nylon balloon at the centre of the detector surrounded by 1000 tonnes of liquid scintillator, which strongly suppresses backgrounds, and 2000 PMTs. This is enclosed within a 3200 tonne water-Cherenkov detector to veto cosmic-ray muons further improving the background rejection. The first phase used ~ 300 kg of ^{136}Xe in 13 tonnes of liquid scintillator and achieved an exposure of 89.5 kg yr equivalent to a half-life limit of $T^{0\nu}_{1/2} > 1.9 \times 10^{25}$ yr, corresponding to $\langle m_{\beta\beta} \rangle < 160 - 330$ meV [45].

  Since the initial phase the liquid scintillator has undergone a purification process to remove impurities. The latest results from the second phase using ~ 340 kg of ^{136}Xe shows the $^{110\text{m}}$Ag was reduced by a factor 10 and with an exposure of 504 kg yr a half-life limit of $T^{0\nu}_{1/2} > 9.2 \times 10^{25}$ yr was set. Combining the results from phase 1 and 2 gives a half-life limit of $T^{0\nu}_{1/2} > 1.07 \times 10^{26}$ yr corresponding to $\langle m_{\beta\beta} \rangle < 61 - 165$ meV [36].

  Furthermore, due to its low background level, KamLAND-Zen can observe $2\nu\beta\beta$ across a wide energy range and provide strong constraints on Majoron emission decay modes [46].

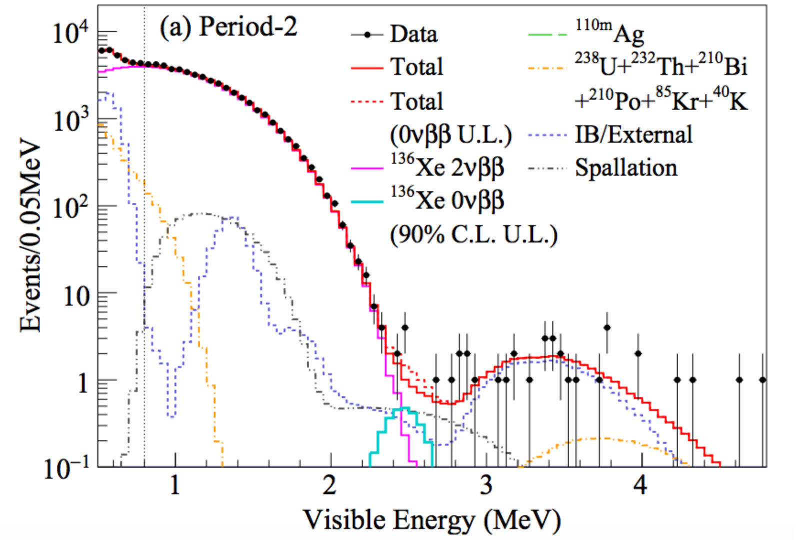

Figure 3.3: Energy spectrum of results from KamLAND-Zen [36].

Future upgrades would see the construction of KamLAND2-Zen which will upgrade the KamLAND detector to improve light collection. The load isotope capacity will be enlarged to hold 1 tonne of ^{136}Xe. The final expected sensitivity is $\langle m_{\beta\beta} \rangle \sim 20$ meV [47].

The second method is where the isotope is inherently part of the scintillator. The two major experiments using this design are: the ELEGANT VI experiment, and the CANDLES III experiment. Both are using ^{48}Ca as the target isotope.

- **ELEGANT VI** experiment was located in Kamioka, using 23 CaF$_2$(Eu) crystal scintillators with a total mass of 7.6 g of ^{48}Ca. The crystals were surrounded by an active veto to reduce background. A total exposure of 0.015 kg yr produced a half-life limit of $T^{0\nu}_{1/2} > 5.8 \times 10^{22}$ yr or $\langle m_{\beta\beta} \rangle < 3.5 - 22$ eV [48].
- **CANDLES III** evolved from ELEGANT VI. 305 CaF$_2$ crystals are used that have a total mass of 305 kg and 300 g of ^{48}Ca. These crystals are surrounded by liquid scintillator which acts as active shielding and removes the need for doping of the crystals. The experiment is currently taking data and a sensitivity to $\langle m_{\beta\beta} \rangle$ of 0.5 eV is expected. If improvements in enrichment technology are realised, then the scale of the experiment will be increased by an order of magnitude to contain $\sim$ 3 kg of ^{48}Ca and achieve a sensitivity of $\sim$50 meV [49].

3.2.2. Bolometer Experiments

The radioactive decay process is measured through minute temperature rises within a material as a result of energy absorption. The amount of heat generated is proportional to the ionising particle energy as it passes through the material. The temperature increase is then the ratio of the energy deposited over the heat capacity. Since the heat capacity of material at very low temperatures T is proportional to T^3, bolometer experiments are usually operated at below 10 mK. Semiconductor thermistors are used to measure the temperature variations.

Generally, bolometer experiments have good energy resolution and detection efficiency. However, particle identification can be challenging and the detector response time can be long (order of seconds). This can pose problems in reducing the background to the necessary levels.

- **CUORICINO** operated between 2003 and 2008 with a tower array of 62 enriched and natural TeO$_2$ crystals made from 75% and 33.8% of isotope

^{130}Te respectively. In total, 11 kg of ^{130}Te was used with a total exposure of 19.75 kg yr which translates to a half-life limit of $T^{0\nu}_{1/2} > 2.8 \times 10^{24}$ yr, corresponding to $\langle m_{\beta\beta} \rangle < 300 - 710$ meV [50]. The array was installed inside a dilution refrigerator, at the LNGS, to maintain cryogenic temperatures of 8 mK and surrounded by passive shielding.

- **CUORE** will be the successor of CUORICINO based on the same technology, increasing the number of TeO_2 crystals to 988 corresponding to 206 kg of ^{130}Te. A prototype detector, CUORE-0, is a single tower produced from the CUORE assembly line. It contained 52 crystals with a total of 10.9 kg of ^{130}Te and operated between 2013 and 2015. It re-used the CUORICINO cryostat which has a higher background than that anticipated for CUORE. The CUORE-0 experiment achieved a background of $0.058 \pm 0.004 \pm 0.002$ cts/keV/kg/yr in the region of interest (ROI) and a half-life limit of $T^{0\nu}_{1/2} > 2.7 \times 10^{24}$ yr and $T^{0\nu}_{1/2} > 4.0 \times 10^{24}$ yr or $\langle m_{\beta\beta} \rangle < 270 - 760$ meV when combined with previous CUORICINO results [51]. CUORE plans to start operations by the end of 2016. The target background in the ROI is 0.01 cts/keV/kg/yr with expected sensitivities of $T^{0\nu}_{1/2} > 9.5 \times 10^{25}$ yr ($\langle m_{\beta\beta} \rangle < 50 - 130$ meV) [52].

In order to further reduce the background level of bolometric experiments scintillating bolometers could be used with scintillation tagging. A small fraction of the energy deposited in the crystal is released as light which can be used to significantly reduce backgrounds from surface contamination.

- **LUCIFER** will study ^{82}Se using ZnSe as scintillating bolometric crystals. The isotope choice has the advantage of a high Q value ($Q_{\beta\beta} = 2.998$ MeV), above ^{208}Tl at 2.615 keV. The experimental configuration will be similar to CUORE with the addition of an extra bolometer which will act as a light detector for the scintillation light. The target experimental background is 0.001 cts/keV/kg/yr in the region of interest. The crystals will contain ~ 18 kg of ^{82}Se and have a half-life limit of $T^{0\nu}_{1/2} > 6.0 \times 10^{25}$ yr ($\langle m_{\beta\beta} \rangle < 70 - 190$ meV).

3.2.3. Semiconductor Experiments

Semiconductor experiments are the most popular homogeneous design where a $0\nu\beta\beta$ candidate isotope acts both as the source and the detector. The natural abundance of the $0\nu\beta\beta$ isotope is usually enriched to increase isotope mass. The most popular choice is Ge with ^{76}Ge, which can be readily enriched to above 80% abundance and produce large pure crystals. High-purity germanium (HPGe) detectors allows high detection efficiency for gamma rays up to ~ 5 MeV and the crystals used are extremely radio-pure. HPGe detectors must be operated at cryogenic temperatures to optimise the intrinsic resolution of detector. In this configuration they can achieve excellent energy resolution of $\sim 0.3\%$ (FWHM). The main disadvantage is the low $Q_{\beta\beta}$ for ^{76}Ge at 2039 keV.

Modern development of Broad Energy Germanium (BEGe) detectors further improves the performance such as energy resolution and lower backgrounds. The small size of its signal electrode results in low capacitance which improves the energy determination and the BEGe also has an increased field near the electrode for more advanced capability of background identification using the event topology. As a result BEGe detectors are used in all modern Ge $0\nu\beta\beta$ decay experiments. Modern generation HPGe experiments: GERDA and MAJORANA, are now building on the successes of previous H-M [53] and IGEX [54] experiments:

- **GERDA** is located at the LNGS and consists of a series of HPGe detectors, 8 from H-M and IGEX, immersed in a 64 m^3 cryostat filled with liquid argon (LAr) for active shielding. This gives GERDA the ability to directly test the H-M claim [55] of $0\nu\beta\beta$ decay. The LAr provides both cooling and shielding against external backgrounds. In addition the cryostat is surrounded by 3 m of ultra-pure water shielding with PMTs to detect Cherenkov light from cosmic muons.

  The experiment consists of two phases, GERDA-I and GERDA-II. Phase I was designed to verify the H-M claim with a higher sensitivity. Phase II aims to significantly increase the $\beta\beta$ mass and decrease the detector backgrounds to maximise detector sensitivity and physics potential.

  GERDA-I ran from Nov 2011 to May 2013 with eight recycled HPGe detectors from H-M and IGEX, totalling 17.7 kg, along with 3.6 kg of new BEGe detectors. Despite the shorter run time, lower backgrounds of 0.01 cts/keV.kg.yr meant GERDA-I achieved a total exposure of 21.6 kg yr. No $0\nu\beta\beta$ signal was observed setting a half-life limit of $T_{1/2}^{0\nu} > 2.1 \times 10^{25}$ yr, which corresponds to a limit of $\langle m_{\beta\beta} \rangle < 240 - 480$ meV [56].

GERDA-II aims to add a further 20 kg of enriched Germanium and reduce the detector background by a factor 10, with an increase in sensitivity to reach the $50 - 100$ meV level [57]. A first analysis of GERDA Phase-II results showed it has reached a background of 0.001 cts/keV/kg/yr which is a major achievement.

- **MAJORANA** is located at the Sanford Underground Laboratory using a very similar technique to the GERDA experiment. The key differences are MAJORANA will deploy its HPGe detectors in a custom vacuum cryostat instead of submersing them in LAr and will use a compact shield made with lead, oxygen free copper, electro-formed copper and scintillator paddles instead of LAr and high purity water as is the case with GERDA. It aims to achieve extremely low backgrounds of 0.001 cts/keV/kg/yr. To do this requires many of the detector components to be especially made in underground facilities to ensure they meet the ultra low radio-purity requirements, as well as more effective shielding and the use of pulse shape discrimination. A Demonstrator has operated since January 2016 to prove that the required low background levels can be achieved. The Demonstrator consists of two modules with a total of 35 (29.66 kg) of p-type point contact detectors with 88% enriched ^{76}Ge and 24 (15.1 kg) natural Ge.

  Module 1 achieved a exposure of 3.03 kg yr setting a half-life limit of $T^{0\nu}_{1/2} > 3.7 \times 10^{24}$ yr. Module 2 is due to come online at the end of 2016, if the target background levels can be achieved, a sensitivity of $80 - 160$ meV will be reached after 2.5 years of data-taking [58].

The future will see the MAJORANA and GERDA collaborations working cooperatively, to build a tonne level experiment in ^{76}Ge with a sensitivity of $\langle m_{\beta\beta} \rangle \sim 15$ meV [59].

- **COBRA** operates at LGNS and uses an array of CdZnTe (CZT), an intrinsic semiconductor at room temperature, which holds five different $\beta\beta$ isotopes, ^{114}Cd, ^{128}Te, ^{70}Zn, ^{130}Te and ^{116}Cd. The COBRA Demonstrator consists of a 4x4x4 array of 1 cm^3 (5.9g) detectors and achieved a 234.7 kg d exposure, setting a half-life limit of $T^{0\nu}_{1/2} > 1.6 \times 10^{21}$ yr, $T^{0\nu}_{1/2} > 1.9 \times 10^{21}$ yr, $T^{0\nu}_{1/2} > 6.8 \times 10^{18}$ yr, $T^{0\nu}_{1/2} > 6.1 \times 10^{21}$ yr and $T^{0\nu}_{1/2} > 1.1 \times 10^{21}$ yr respectively [60].

  An energy resolution better than 1.2% FWHM at 2600 keV has been achieved, and a background rate of approximately 2.7 counts/keV kg yr has been achieved.

Although the energy resolution is not as good as with HPGe experiments, it possesses the advantage of operating at room temperature. The experiment will proceed with a 3x3x3 test array of new crystals with improved readout, finally moving towards a 415 kg detector with a modular 20 layer design using larger 2x2x1.5cm (36g) crystals with segmented readout. Using this design, it could be possible to track and identify particles which may greatly reduce the background level. If the background is sufficiently reduced, such a detector can expect a target sensitivity of $50 - 70$ meV.

3.2.4. Time Projection Chamber Experiments

Time projection chamber (TPC) experiments consist of a liquid medium embedded within an electric field and are able to acquire position information of the electron as it passes through a detector. In a gaseous TPC the ionising radiation produces free electrons that are drifted towards a collection device giving long tracks. The induced current is proportional to the level of ionisation. While the location of the energy deposit provides two-dimensional positioning, knowing the drift speed of free electrons through the medium and their measured arrival times can allow for 3 dimensional event reconstruction. This allows the search for two electrons from a common vertex which is a powerful background rejection method.

Most TPC experiments are complemented by selecting a detector medium that is also a scintillator, this provides the critical measurement of a T_0 and a more accurate energy measurement. Xenon is the only medium suitable for TPC design among double-β candidates with the advantage of being the cheapest isotope to enrich.

- **EXO** is located in an underground clean room at the Waste Isolation Pilot Plant (WIPP) in New Mexico, U.S.A. and uses a cylindrical homogeneous TPC. The current generation detector EXO-200 is filled with 200 kg of liquid xenon enriched to 80% in ^{136}Xe. Of the total xenon mass 175 kg is in a liquid phase, and 110 kg is in the active volume of the detector. The TPC is symmetric around a central cathode grid and at each end there are planes of anode wires with an array of avalanche photodiodes for ionisation and scintillation readout, respectively.

EXO-200 phase I began taking data in 2011 and achieved a total exposure of 100 kg yr. No $0\nu\beta\beta$ signal was observed setting a half-life limit of $T^{0\nu}_{1/2} > 1.1 \times 10^{25}$ yr, which corresponds to a limit of $\langle m_{\beta\beta} \rangle < 190 - 450$ meV. It was also able to demonstrate good energy resolutions of 1.53 % and achieve background levels of 0.0017 cts/keV/kg/yr [61].

EXO-200 phase II started data acquisition in Jan 2016 with improved readout, detector resolution and radon suppression in the surrounding gas. It is expected to reach a half-life limit of $T^{0\nu}_{1/2} > 5.7 \times 10^{25}$ yr.

The EXO-200 experiment has demonstrated the ability to reach the energy resolution and background goals. The next generation detector, nEXO, will scale the isotope mass to 5 tonnes, with sub 1% energy resolution. Also, by scaling up, the backgrounds can be reduced as it does not scale linearly with isotope mass. New techniques such as barium ion tagging can further drastically reduce the background levels. The nEXO experiment aims to achieve a sensitivity of $T^{0\nu}_{1/2} > 6.6 \times 10^{27}$ yr or $\langle m_{\beta\beta} \rangle < 7 - 18$ meV [62] for 5 years of data.

- **NEXT** will be located at the LSC and applies a similar technique to the EXO experiment, using both scintillation and ionisation signals. However, the choice of medium is gaseous xenon at high pressure rather than liquid xenon. Although liquid xenon detectors are easily scalable, a gaseous xenon TPC offers the advantage of tracking as particles moves through the detector. The xenon is contained within an asymmetric TPC which has an array of PMTs at one end, and silicon photomultipliers at the other. Electrons excite and ionise the xenon which emits the prompt scintillation light detected by the PMTs at one end of the TPC (energy plane). The electrons from the ionisation are drifted by a weak electric field to the electro-luminescence region where a larger electric field accelerates the electrons to excite but not ionise the Xe. This produces a large amount of 172 nm photons which are detected by both the silicon photomultipliers on the other end of the TPC (tracking plane) as well as the energy plane, providing tracking reconstruction, to greatly reduce background, and improve the energy resolution to better than 1%. However, maintaining detector stability and the complexity of working at high pressure are much more challenging in gaseous TPCs compared to liquid TPCs with cryostat-cooling.

The demonstrator NEXT-100 detector is currently under construction and will contain 100 kg of gaseous xenon enriched to 91% in ^{136}Xe. It aims to achieve background levels of 0.0004 cts/keV kg yr and better than 0.6% resolution at FWHM of $Q_{\beta\beta}$. After three years of running it is anticipated to reach a sensitivity of $T_{1/2}^{0\nu} > 6 \times 10^{25}$ yr corresponding to $\langle m_{\beta\beta} \rangle < 80 - 160$ meV [63]. If the experiment is successful, there is the possibility to enlarge it to contain a tonne of material and achieve sensitivities of $\langle m_{\beta\beta} \rangle < 15 - 32$ meV.

3.2.5. Tracker Calorimeter Experiments

Tracker calorimeter experiments follow a more classical collider detector design where the event occurs at the centre of the detector surrounded by a tracking volume followed by a separate calorimeter for energy measurements. This provides the advantage of full topology reconstruction and kinematics of single particles which results in excellent background rejection and the ability to disentangle the underlying $0\nu\beta\beta$ decay mechanism [24]. These experiments can therefore achieve some of the lowest background rates of all $0\nu\beta\beta$ experiments across the entire energy spectrum, which makes them ideal for both $2\nu\beta\beta$ and $0\nu\beta\beta$ measurements. In the case of two important models, the mass mechanism (MM) and the right-handed current (RHC), it has been shown that the angular and electron energy difference distributions can be used to discriminate between the models, as shown in Figure 3.4. Another advantage of separation between source and detector is the flexibility of studying any $0\nu\beta\beta$ isotope. The cost of such a design is relatively poorer energy resolution.

- **NEMO-3** was located at the Laboratoire Souterrain de Modane (LSM) and operated from 2003 to 2011. It was the most successful tracker calorimeter experiment to date and carried out $0\nu\beta\beta$ decay searches in seven different double-$\beta\beta$ isotopes setting the leading $0\nu\beta\beta$ limits on four isotopes and the most accurate measurement of $2\nu\beta\beta$ half-lives on all seven isotopes. The $0\nu\beta\beta$ isotopes were made into thin foils and placed at a fixed radius around the detector. The foil was then surrounded on either side by a gaseous tracker operated within a magnetic field of 25G to enable charge identification. This is further enclosed by the calorimeter walls which provided position, energy and timing measurements of individual electrons, positrons, gamma rays and α particles. The NEMO-3 detector achieved a background level in the signal

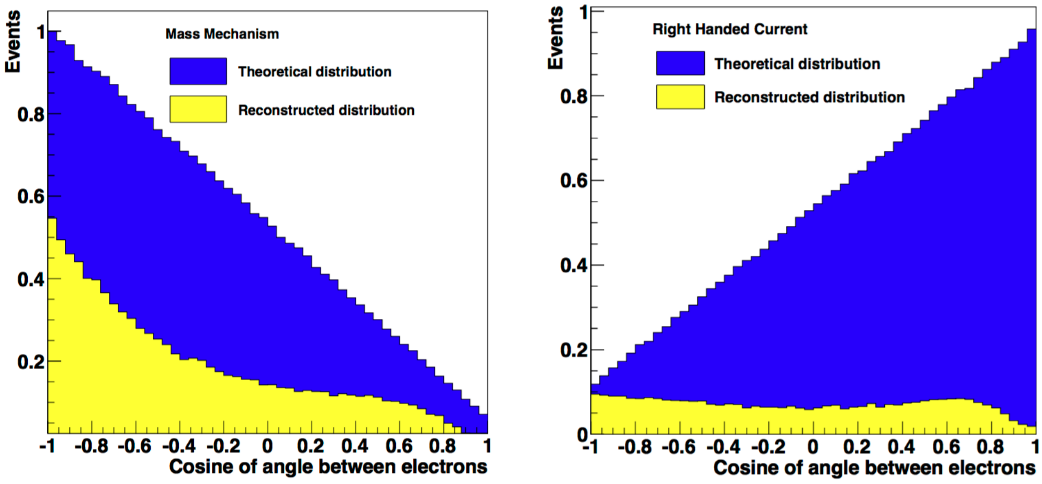

(a) MM **(b)** RHC

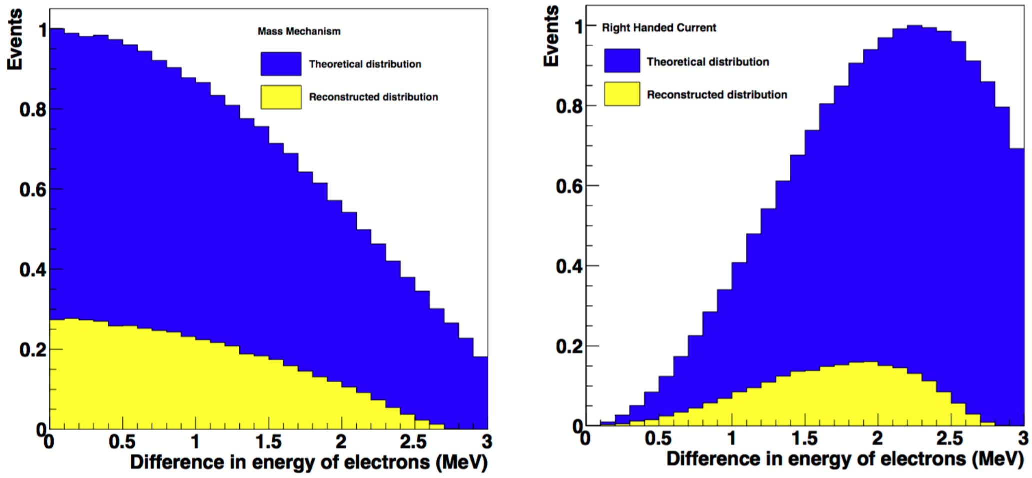

(c) MM **(d)** RHC

Figure 3.4: Theoretical and experimental electron angular distributions for MM (a) and RHC (b). Theoretical and experimental electron energy difference distributions for MM (c) and RHC (d). All distributions are shown for the isotope ^{82}Se and the reconstructed distributions are normalised to the theoretical distribution to show signal efficiency [24].

region [2.8-3.2] MeV of 0.44 ± 0.13 cts/yr/kg. The most stringent $0\nu\beta\beta$ limit of NEMO-3 comes from 6.9 kg of ^{100}Mo, with an exposure of 34.3 kg yr setting a limit of $T^{0\nu}_{1/2} > 1.1 \times 10^{24}$ yr or $\langle m_{\beta\beta} \rangle < 330$ - 620 meV [64].

- **SuperNEMO** will also be located at the LSM and will build upon the successful NEMO-3 design with improvements in radiopurity, calorimeter design and detection efficiency. It will feature 20 identical modules containing 100 kg of enriched ^{82}Se with a target sensitivity of $T^{0\nu}_{1/2} > 1.0 \times 10^{26}$ yr corresponding to $\langle m_{\beta\beta} \rangle < 50 - 100$ meV [65]. More information on SuperNEMO can be found in Chapter 4.

3.3. Outlook to Future Experiments

The observation of $0\nu\beta\beta$ decay would crucially confirm lepton number violation. The current generation of experiments which are currently under construction or data-taking will be sensitive to $\langle m_{\beta\beta} \rangle \sim 60$ meV which probes the top of the parameter space for the inverted hierarchy, as shown in Figure 2.10. Many of these experiments have plans to scale up to larger masses in order to probe the full inverted hierarchy parameter space at $\langle m_{\beta\beta} \rangle \sim 10$ meV. Therefore, if there is conclusive evidence from oscillation experiments for the inverted hierarchy and $0\nu\beta\beta$ is mediated by the mass mechanism then the next generation of experiments will either discover or exclude the $0\nu\beta\beta$ process.

The current and future sensitivities for seven key $0\nu\beta\beta$ decay experiments are summarised in Table 3.2. The future achievable sensitivities are based on predictions by each experiment.

Experiment	$\langle m_{\beta\beta} \rangle$ (meV)	
	Present sensitivity	Future sensitivity
SNO+	$<$ 50 - 100	$<$ 20 - 40
KamLAND-Zen	$<$ 61 - 165	$\sim$ 20
CUORE	$<$ 270 - 760	$<$ 50 - 130
GERDA	$<$ 240 - 480	$<$ 50 - 100
(GERDA + MAJORANA)	N/A	$\sim$ 15
EXO	$<$ 190 - 450	$<$ 7 - 18
NEXT	N/A	$<$ 80 - 160
SuperNEMO	N/A	$<$ 50 - 100

Table 3.2: A summary of experimental capability of different $0\nu\beta\beta$ decay experiments in the present and future (at 90% C.L.).

To reach the sensitivity required for the normal hierarchy: original innovation, R&D and intelligent experimental design will be necessary to overcome the numerous challenges. Present $2\nu\beta\beta$ experiments, with few exceptions, are sensitive to all mechanisms [39] but are limited to only being able to distinguish between one or two modes of $0\nu\beta\beta$ decay, either light neutrino exchange or Majoron emission.

Chapter 4.

The SuperNEMO Experiment

SuperNEMO is a modern $0\nu\beta\beta$ decay experiment with a design capability to reach a half-life sensitivity of 10^{26} years. This corresponds to an effective Majorana neutrino mass of $\langle m_{\beta\beta}\rangle$ < 50 - 100 meV. It distinguishes itself from other double beta decay experiments as it can reconstruct the 3D topology of each detected event, thus providing a unique and powerful background rejection method and evidence for the underlying decay process.

To achieve the required sensitivity stringent radio-purity requirements are imposed for both the construction materials and the gas in the tracking chamber. A stringent screening and selection programme for these materials is therefore required. Dedicated facilities have been established in the UK for the assay of detector construction materials.

4.1. From NEMO-3 to SuperNEMO

The NEMO-3 detector had a cylindrical design with a height of 3 m and a diameter of 5 m as seen in Figure 4.2. This design allowed for the direct detection of two electrons from a common vertex. Although it did not observe the $0\nu\beta\beta$ decay, it was a successful experiment, setting the world leading limits on all seven isotopes as well as the best measurements of their $2\nu\beta\beta$ half-lives.

The SuperNEMO design is based essentially on the principles of the NEMO-3 detector, with upgrades to energy resolution, reduction in backgrounds and an increase in isotope mass as summarised in Table 4.1. SuperNEMO aims to achieve a background

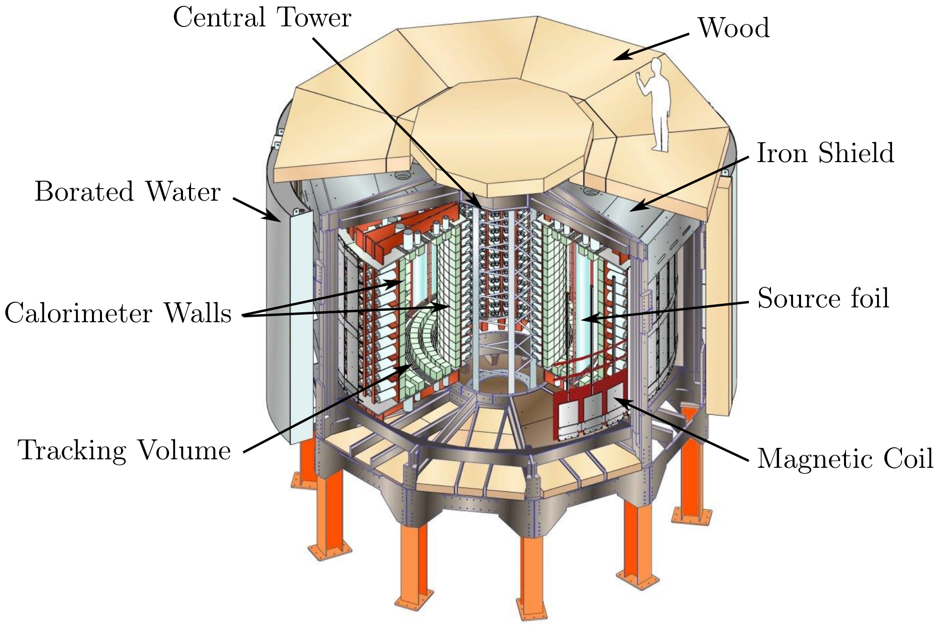

Figure 4.1: Schematic of the NEMO-3 design showing the key aspects of the detector.

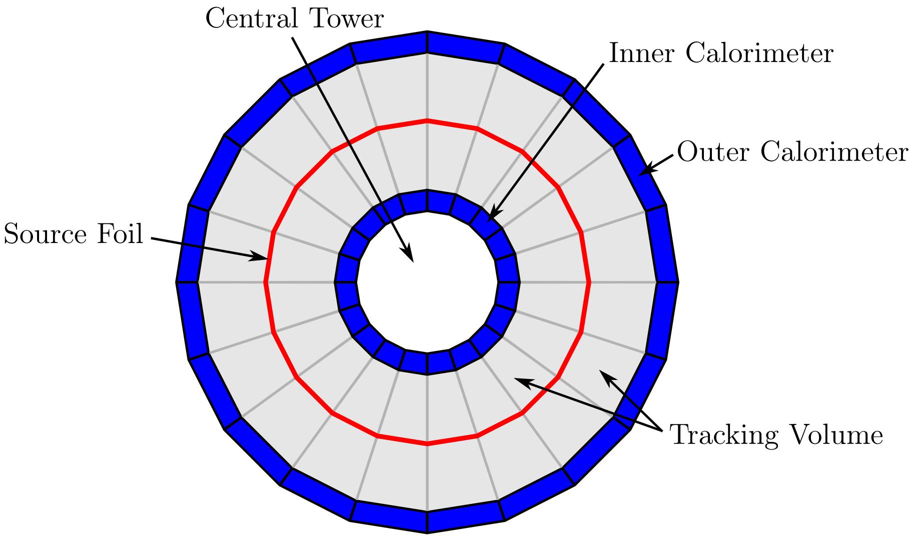

Figure 4.2: Section across the diameter of NEMO-3 showing the 20 identical sectors, each containing source foil, tracker and calorimeter.

level of 0.0005 cts/keV/kg/yr in the region of interest. The primary isotope is ^{82}Se, however, as with NEMO-3 other isotopes can also be used.

Detector Property	NEMO-3	SuperNEMO
Isotope	^{100}Mo	^{82}Se
Source Mass	7 kg	100 kg
$0\nu\beta\beta$ Efficiency	18%	30%
Energy Resolution	8% @ 3 MeV	4% @ 3 MeV
^{214}Bi in foils	300 µBq/kg	10 µBq/kg
^{208}Tl in foils	100 µBq/kg	2 µBq/kg
^{222}Rn in tracker	5 mBq/m^3	0.15 mBq/m^3
$T^{0\nu}_{1/2}$ Sensitivity	10^{24} yr	10^{26} yr
$\langle m_{\beta\beta}\rangle$ Sensitivity	0.3 – 0.7 eV	40 – 100 meV

Table 4.1: Summary of the key experimental achievements of NEMO-3 and the target levels for SuperNEMO.

This chapter gives a brief overview of the SuperNEMO detector, for a more detailed description of the SuperNEMO detector and its operational principles please refer to the SuperNEMO conceptual design report [66].

4.2. SuperNEMO Detector Geometry

The SuperNEMO baseline design consists of 20 identical planar modules. Each module is 6m long, 4m high and 2m wide and comprises five segments with the $0\nu\beta\beta$ decay isotope made into a thin foil (40mg/cm^2) at the centre. The foil is then surrounded by a gaseous tracking chamber on either side, followed by calorimeter walls, as shown in Fig 4.3.

The first module to be constructed will contain all the design upgrades as a proof of principle and will be called the demonstrator. This first module, currently under construction, will contain 7 kg of ^{82}Se (other isotopes possible) and is expected to reach a half-life sensitivity of $T^{0\nu}_{1/2} > 6.5 \times 10^{24}$ yr. The key radio-purity requirements for the demonstrator are A(^{214}Bi) < 10 μBq/kg, A(^{208}Tl) < 2 μBq/kg for the source foil and < 0.15 mBq/m^3 for the tracker gas.

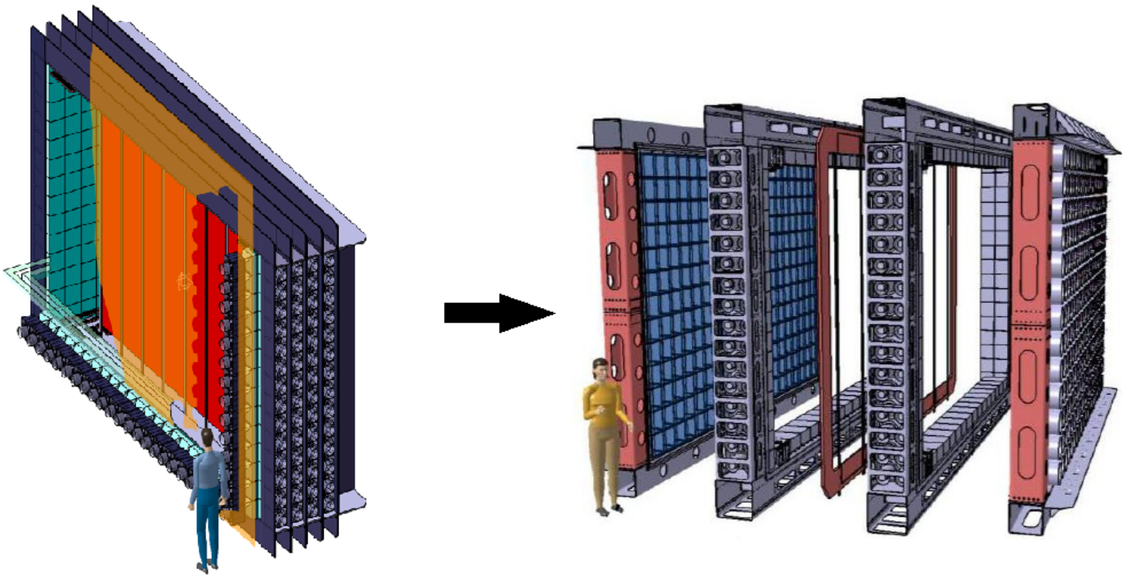

Figure 4.3: Schematic showing on the left a single complete SuperNEMO module, and on the right an open Demonstrator with the central source foil surrounded by the tracking chambers on either side, followed by the calorimeters.

In order to achieve the challenging targets, all construction materials are screened using HPGe detectors to varying levels of sensitivity, depending on location within the detector. Those materials in direct contact with the tracker gas are further screened for radon emanation.

Together the tracker, calorimeter and the magnetic field gives SuperNEMO the distinctive ability to reconstruct the trajectory in all three dimensions, determine the vertices, differentiate between positive and negative charge, find the time of flight and measure the energies of single charged particles. Therefore, tight constraints can be placed on $0\nu\beta\beta$ events as the event requires two electron being emitted from the same point on the foil simultaneously. Using the vertex and angular distributions between the two emitted electrons and the total energy measured by the calorimeters this method gives SuperNEMO a powerful method for recognising a $0\nu\beta\beta$ event from background, as shown in Fig 4.4.

In addition to being underground, which reduces cosmic rays by 10^6, all modules are housed within a low radon environment and surrounded by ultra-pure water passive shielding [67] to capture fast and thermal neutrons as well as iron shielding to reduce γ rays. The potential of SuperNEMO to probe new physics scenarios of

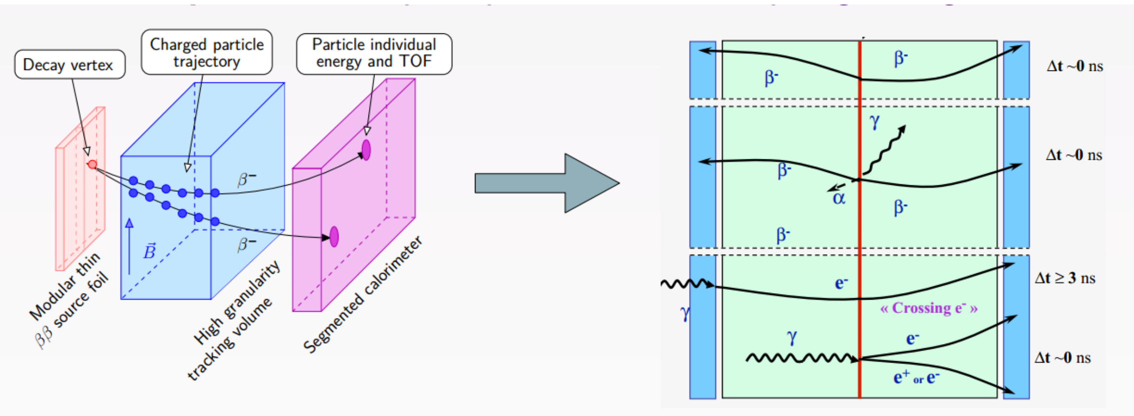

Figure 4.4: Schematic demonstrating, on the left, the ability to reconstruct a particle's trajectory in three dimentions and, on the right, the ability to distinguish between the various background events for the $0\nu\beta\beta$ process. The top process shows the $0\nu\beta\beta$ process, the rest are other processes which could contribute to background.

light Majorana neutrino exchange and right-handed currents has been studied in detail [24].

4.3. Source Foil

A key design feature of SuperNEMO is the ability to measure different isotopes since it is an inhomogeneous detector where the source is separate from the detector. After installation it is also possible to extract and exchange the source foil for a different isotope. The isotope ^{82}Se was selected due to; its transition energy ($Q_{\beta\beta}$), NME, phase space, backgrounds in the energy region of interest, half-life of the standard model allowed $2\nu\beta\beta$ decay, purification feasibility, isotopic abundance of the candidate as well as the feasibility of enrichment.

The enrichment of ^{82}Se was performed in Russia using a centrifugation method. The production of source foils (with a thickness of 40-60 mg/cm2) were developed at LAPP (Annecy) and ITEP (Moscow). Since the source foil is at the heart of the detector, it has the most stringent radio-purity requirements of A(^{214}Bi) < 10 μBq/kg, A(^{208}Tl) < 2 μBq/kg. To confirm this level of radio-purity has been achieved a dedicated detector called BiPo [68] was constructed which measures the well known features of the delayed coincidence between an electron and an alpha particle (BiPo events), see in Figure 6.7b.

4.4. Tracker

The tracking chamber contains 2000 wire drift cells operated in Geiger mode within a gas mixture of He (95%), Ar (1%) and ethyl alcohol (4%). The cells are arranged in nine layers parallel to the foil. Each cell has a 40μm stainless steel central anode wire surrounded by twelve 50μm ground wires, with a cathode pickup ring at each end. A 25G magnetic field is used to reject positron events from external γ background. Due to the large number of wires (over 400,000 wires for all 20 modules) and strict radio-purity requirements, automated wiring is used (Figure 4.5).

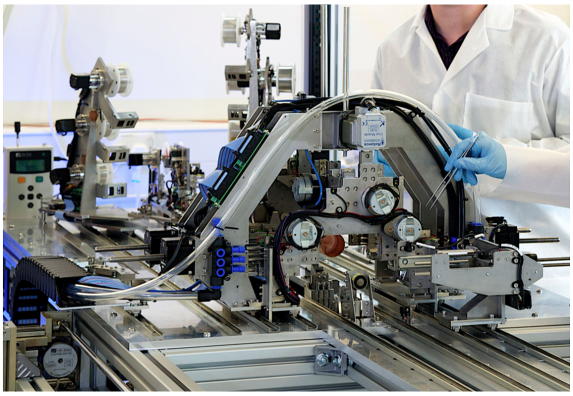

Figure 4.5: Wiring robot used for cell production for SuperNEMO.

4.5. Calorimeter

The Demonstrator calorimeter will contain 550 plastic scintillator blocks with a cross-section of 26cm×26cm coupled to a low radioactive 8 inch PMT. In addition, there are 64 veto blocks, and 128 X-wall blocks, on top and bottom of the tracker module. This configuration has demonstrated energy resolutions of $7-8\%/\sqrt{E(\mathrm{MeV})}$.

The three key functions of the calorimeter are to measure the particle energy, the time-of-flight (TOF) in order to measure and reject external background and to give a fast trigger signal.

(a) Main wall **(b)** X-wall

Figure 4.6: Examples of SuperNEMO calorimeter blocks.

4.6. Readout electronics and data acquisition system

The SuperNEMO detector will have a very low data acquisition rate compared to standard HEP experiments therefore it is practical to run SuperNEMO readout as a triggerless system. This means all data is recorded allowing the processing and topology reconstruction to be performed offline. The trigger and data acquisition system for the tracker and calorimeter are inter-dependent. The calorimeter front-end boards determine the timing since the calorimeter is much faster than the tracker. The tracker is then synced to the calorimeter clock. This is not only the triggering and data collection for double-β runs but also for calibration runs and background studies. A block diagram of the SuperNEMO readout electronics can be seen in Figure 4.8.

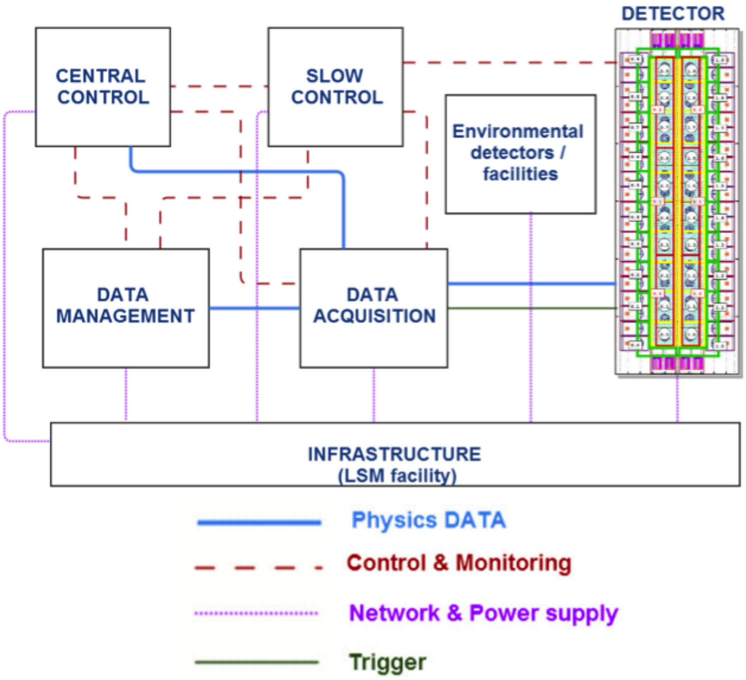

Figure 4.7: Schematic of the SuperNEMO readout electronics.

4.7. Radon Shielding

The gaseous tracker is isolated from the external environment by the detector main frame which is sealed tightly together using materials selected as good radon barriers. The detector is thoroughly checked for leaks which are removed with styrene-butadiene rubber (SBR) which forms a radon barrier. A further layer of nylon film, 25 μm thick, is placed directly in front of the calorimeter wall to further reduce radon diffusing into the tracker gas. The thickness is selected to prevent any loss of energy resolution in the calorimeter yet still providing a factor 10^5 reduction in radon activity.

4.8. Passive Shielding

The SuperNEMO detector will be housed inside the Frejus mountain, under 1200 meters of rock (4800 m.w.e.) reducing the cosmic muon flux by six orders of magnitude. Although cosmic muons do not pose a direct background due to their distinct event signature they can produce neutrons from spallation. However, there are still gamma rays and neutrons coming from nuclear decay in the surrounding environment under the mountain. The neutrons can undergo neutron capture on various parts of the detector frame, and produce up to 10 MeV gammas. The gamma rays can interact with the source foil and cause the emission of two electrons via three processes, see Figure 4.8.

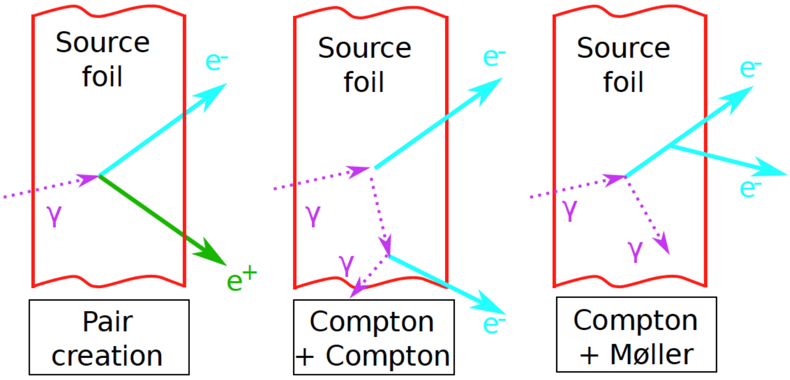

Figure 4.8: External gamma mimicking double electron event topology.

To prevent a background contribution from the surrounding environment, external shielding was constructed which is composed of 20 cm of iron for the external gammas and 20 cm of paraffin for the neutrons. This external shielding is surrounded on all sides by 35 cm of borated water and 30 cm of wood to further suppress fast neutrons. The use of instrumented (with PMTs) ultra-pure water or liquid scintillator to tag high energy cosmic muons is also under consideration. A completed SuperNEMO module with all the shielding is shown in Figure 4.9.

4.9. Anti Radon Factory

Due to the rock composition at the LSM, the average radon level inside the underground laboratory is 15 Bq/m^3. In order to minimise radon diffusion into the tracker an anti radon tent will surround the demonstrator module and will be constantly flushed with filtered air. This flow system requires the use of a radon-free air factory consisting of two adsorption columns, 0.6 m and 3 m high, filled with 500 kg of activated charcoal cooled to -50 °C. The trapped radon is allowed to decay away naturally inside the columns. The anti radon facility filters air from within the LSM

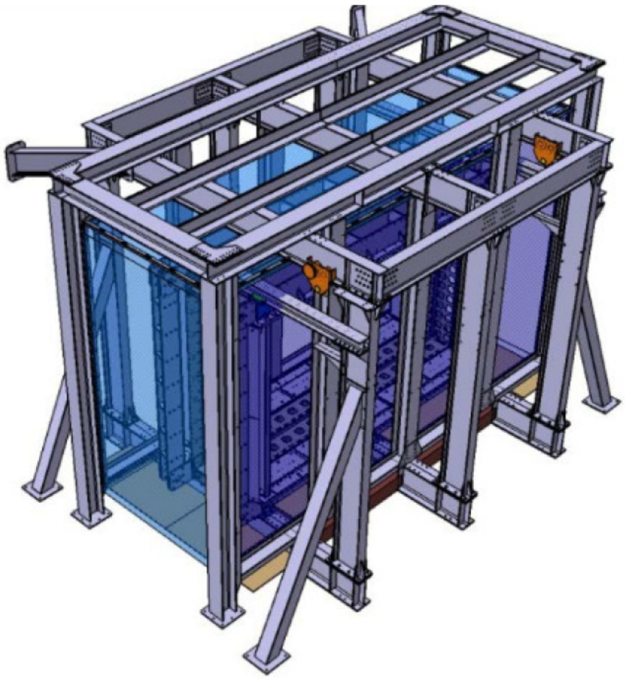

Figure 4.9: Schematic of the SuperNEMO demonstrator module with full external shielding.

lab at a rate of 150 m^3/hr. This will reduce the radon levels in the gas surrounding the detector by three orders of magnitude, from 15 Bq/m^3 to 18 mBq/m^3.

4.10. Alternative calorimeter layout (bar design)

An alternative design to the baseline has been investigated in order to increase scalability. In this alternative design the tracker and calorimeter is replaced with long (2 m) scintillator bars with readouts from both ends using two 3 inch PMTs. Instead of single source foil modules, the bar design would require the construction of super-modules with many calorimeter-source-calorimeter repetitions. The central calorimeters of the super-module are shared between two source foils, see Figure 4.10.

The advantages of the bar design are: more efficient gamma tagging, better self shielding and lower PMT mass leading to further background reduction. The bar design is simpler and would use a reduced number of PMTs and calorimeter channels

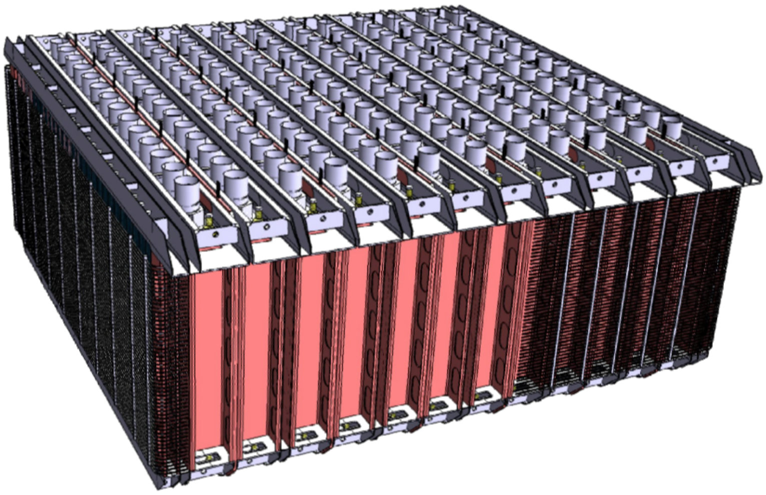

Figure 4.10: A SuperNEMO super-module based on the calorimeter bar design.

meaning it would be significantly cheaper than the baseline design. However, this is at the cost of reduced energy resolution of the scintillator bars.

Ultimately it was decided that the bar design has too many "unknowns" such as the ageing of the scintillator bars, their time calibration, internal/external background levels and a reduced sensitivity to excited states. The planar design is far more similar to NEMO-3 and therefore a safer option. However, the bar design remains a backup option in case the demonstrator cannot meet its strict background targets due to PMT contributions and if scaling of the baseline design proves to be too challenging.

Chapter 5.

Radon Background and SuperNEMO Sensitivity

5.1. Properties of Radon

Radon is a radioactive, colourless, odourless noble gas with symbol Rn and atomic number 86. It occurs naturally as an indirect decay product of uranium and thorium and is found as a monatomic gas with the unusual property that it has only radioactive isotopes.

Of the 36 radioactive isotopes which have been characterised, atomic mass 193-228, the most stable is ^{222}Rn (from the ^{238}U decay series) as shown in Fig 3.1. Another important isotope is ^{220}Rn (from the ^{232}Th decay series) which also produces actinon (^{219}Rn) from the ^{228}Ac series.

Radon was first discovered in 1900 by Friedrich Ernst Dorn who reported of a radioactive gas emanating from radium compounds. Later in 1910, radon was isolated and studied in detail by William Ramsay and Robert Whytlaw-Gray at University College London and it was determined to be the heaviest of the noble gases [69].

As a noble gas, which has a full outer valence shell, radon is inert to most chemical reactions. Combined with a relatively long half-life, radon has a long diffusion length in solids making it difficult to seal against as well as being difficult to remove chemically, posing a major challenge for all low background experiments sensitive to radon. The diffusion length, L_i, of radon in a material, in which it has diffusion coefficient D_i, is usually defined as;

$$L_i = \sqrt{\frac{D_i}{\lambda}} \tag{5.1}$$

where λ is the decay constant. Metals typically have a very short diffusion length. As well as being highly diffusive, when a parent radium atom decays by the emission of an alpha particle, the resulting radon must recoil in the opposite direction for momentum conservation with an initial energy of 86 keV. The distance the recoil radon can travel depends on the material density and composition. This recoil can pose as a background for direct dark matter detection experiments.

Radon levels are heavily location dependent and can vary drastically. In open air, typical ranges are from 1-100 Bq/m^3 reducing to 0.1 Bq/m^3 above the ocean. Indoor levels are usually between 30-50 Bq/m^3 again varying significantly depending on the location as well as the construction materials and ventilation of the building. Cleanrooms, where there is strong ventilation and lack of exposed brickwork, normally have reduced levels of <5 Bq/m^3. Underground laboratories, have a similar level of variation in radon activity which is dependent on the surrounding rock content, ranging from uranium mines (few kBq/m^3) to salt mines (few Bq/m^3).

Outside of experimental physics, accurate measurement of radon activity has become a subject of general interest due to public health concerns. Since radon is gaseous it can be easily inhaled. When radon decays the new radioactive radon daughters are solid and stick to surfaces such as dust particles in the air which in turn can also be inhaled. Once inhaled, such contaminated dust can stick to the airways of the lungs and subsequent radioactive decays of these particles lead to increased risk of developing lung cancer. Radon is therefore responsible for the majority of the public exposure to ionising radiation and is the second largest cause of lung cancer after smoking.

A wide range of commercial devices are therefore available for measuring radon activity in the 0.1 Bq/m^3-1 MBq/m^3 range with varying levels of accuracy. However, current and next generation rare event search experiments require activities of radon far below this sensitivity, requiring the need for custom-made detectors to achieve this level of sensitivity.

5.2. SuperNEMO Radon Budget

The decay daughters of the radon isotopes ^{222}Rn and ^{220}Rn produce ^{214}Bi and ^{208}Tl respectively. Radon is the only gaseous isotope in both decay chains and is highly diffusive. Radon can enter the detector either by diffusion from the environment via the detector seals or by emanation of materials within the detector itself. Once inside the ^{214}Bi and ^{208}Tl can be deposited on the source foil or tracker wires and undergo subsequent β-decay with Q_β of 3.27 MeV and 4.99 MeV respectively which can contribute to the SuperNEMO background. The decay scheme of ^{214}Bi and ^{208}Tl are shown in Figure 5.1 and Figure 5.2 respectively.

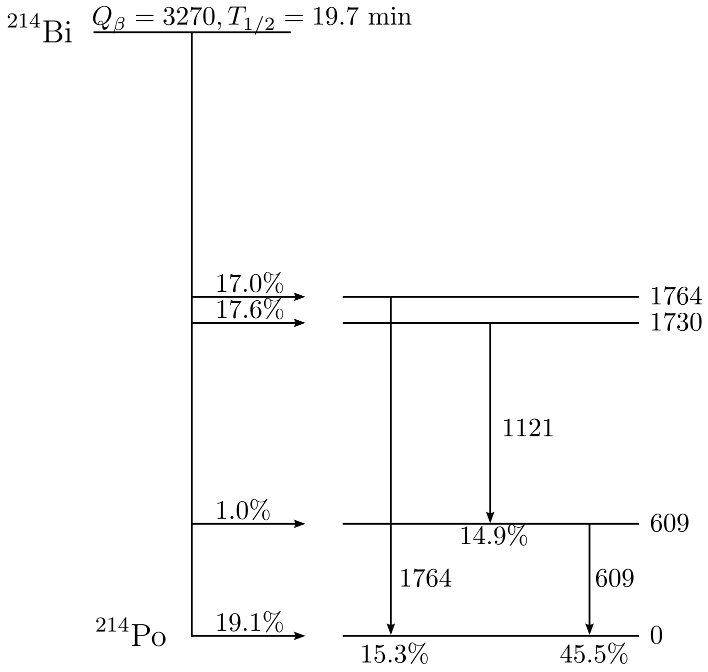

Figure 5.1: Simplified decay scheme for the β-decay of ^{214}Bi to ^{214}Po, showing the three strongest gamma transitions. β-decays are shown as horizontal lines and γ transitions are shown vertically. All energies shown are in keV [19].

The effect of various concentrations of radon on the SuperNEMO sensitivity has been studied and the result is shown in Figure 5.3. In this case ^{222}Rn is of far greater

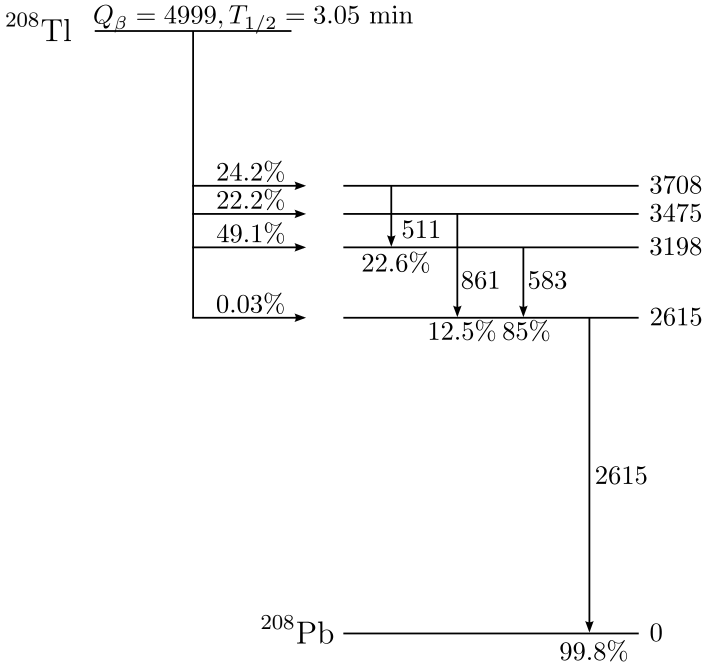

Figure 5.2: Simplified decay scheme for the decay of ^{208}Tl to ^{208}Pb, showing the four strongest gamma transitions. All energies shown are in keV [19].

concern as it has a much longer half-life than ^{220}Rn which has a half-life of 55.6 s which means very little ^{220}Rn can enter the tracker either through diffusion or emanation. The study does not take into account possible ^{214}Bi already present in the source foil, taking this into account a requirement of < 150 µBq/m^3 of radon is set for the tracker gas which is equivalent to the same contribution of ^{214}Bi as from the purified source.

5.3. Active Flow for Radon Suppression

One way to achieve this challenging radon budget is to constantly replace the tracker gas with clean radon-free gas. This removes the diffused and emanated radon, creating an effective radon suppression as a function of flow rate. Studies have shown the optimum flow-rate to achieve the necessary radon suppression factor (18.4), taking into consideration of the costs, to be 33.3 lpm ($\sim$ 2 m^3/hr), as shown in Figure 5.4 [71]. Higher flow-rates can also affect the existing gas mixing system's ability to correctly introduce the required 4% ethanol into the final tracker gas.

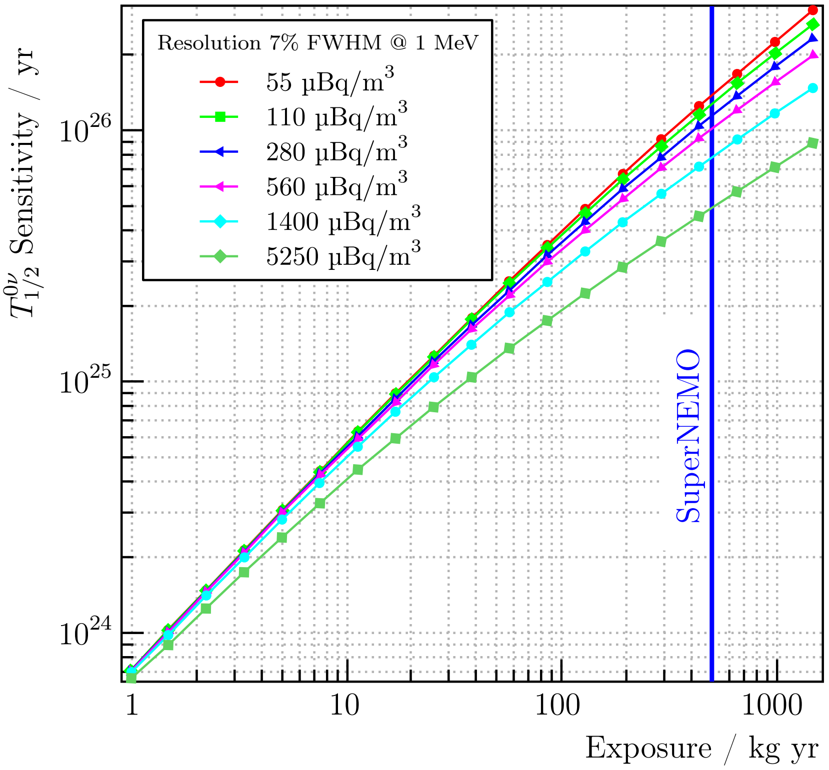

Figure 5.3: SuperNEMO sensitivity as a function of exposure for different radon activities inside the tracker. Internal contamination of ^{214}Bi is neglected [70].

There are several challenges to achieving an active gas flow. Firstly a carbon trap system must be developed, similar to the anti-radon factory, to purify the helium and argon gas of any radon content. Then the gases must be passed through a gas mixing system to ensure the correct concentrations of helium, argon and ethanol are present before the mixture can be delivered to the demonstrator. It is unavoidable a small fraction of radon is also picked up which has been emanated by the gas mixing system itself. Radon purification cannot occur post gas mixing as the ethanol in the gas mixture is adsorbed in a similar way to the radon by the activated charcoal. In fact the ethanol would quickly saturate any trapping system, removing their ability to trap radon. Thus suppression with gas flow also depends on how free the replacement gas can be of radon.

When the tracker is sealed and the radon levels are in equilibrium, the number of radon atoms inside the tracker, N_T^0, is;

$$N_T^0 = A_T/\lambda \tag{5.2}$$

The gas flow suppression factor can be found by taking a ratio of the number of radon atoms in the tracker with flushing and without flushing:

$$F_S = \frac{N_T}{N_T^0} = \frac{A_T + A_G}{\lambda'_T}\frac{\lambda}{A_T} = \frac{1 + A_G/A_T}{1 + f/V_T\lambda} \tag{5.3}$$

where N_T is the number of radon atoms in the tracker with flushing, A_T is the activity of the tracker, A_G is the activity of the flushing gas, f is the flow rate and V_T is the volume of the tracker. Here λ'_T is a modified decay constant:

$$\lambda'_T = \lambda + \frac{f}{V_T} \tag{5.4}$$

where the active flow is equivalent to increasing the natural decay rate. The radon suppression power is plotted as a function of gas flow rate in Figure 5.4 for three different levels of gas activity. A suppression factor of 18.4 can be achieved even with a flushing gas containing a relatively high radon activity as long as a gas flow rate of 33.3 lpm is maintained. Studies have showed the performance of the tracker was not effected [72] at this flow rate.

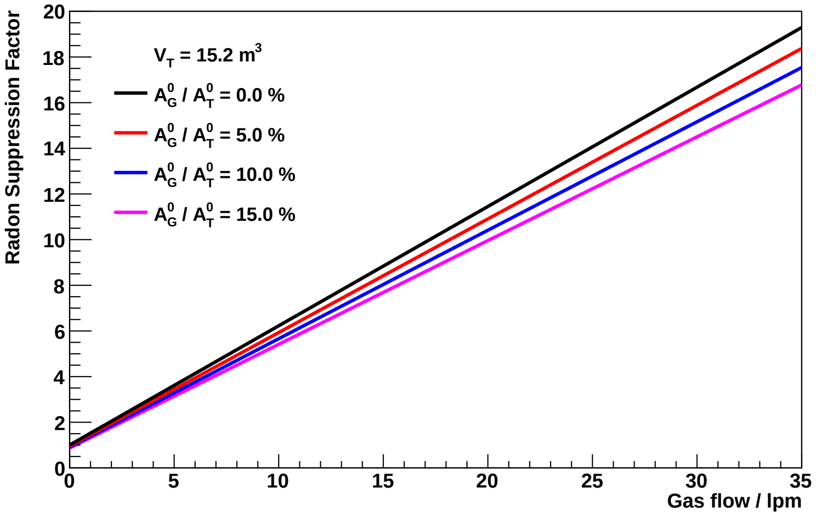

Figure 5.4: Suppression factor for radon activity inside the tracker at various flow rates, with 33.3 lpm, equivalent to 2m^3/hr, the nominal Demonstrator gas flow-rate. Four different levels of radon purity of the input gas is shown at 0%, 5%, 10% and 15%.

Chapter 6.

Radon Detection and Techniques

The SuperNEMO requirement for radon in the tracker gas to be less than 0.15 mBq/m^3 poses a significant challenge not only in terms of reaching this target but also in terms of being able to measure and monitor such ultra-low activities. The best commercial radon detectors in the world are only able to achieve sensitivities of 0.1 Bq/m^3. Therefore, for use in the SuperNEMO experiment an electrostatic detector was especially developed with significantly improved sensitivity, however, it was still not able to achieve the necessary sensitivity. A new system therefore had to be developed called the radon concentration line (RnCL) which further improved sensitivities in order to confirm the challenging SuperNEMO target had been achieved.

6.1. The Electrostatic Detector

A custom-made electrostatic detector, shown in Figure 6.1a, originally developed for high sensitivity radon measurements for the ELEGANT V and Super-Kamiokande experiments [73, 74] was acquired for SuperNEMO. It is capable of measuring radon activities to 1-2 mBq/m^3, 2 orders of magnitude better than the best commercial radon detectors.

The detector consists of an electro-polished stainless steel chamber, with a volume of 70 litres, and a silicon PIN diode located at the top, as shown in Figure 6.1b. The detector electronics are housed in the lid of the detector separated from the detection chamber by a sheet of perspex with a feedthrough for the PIN diode. This

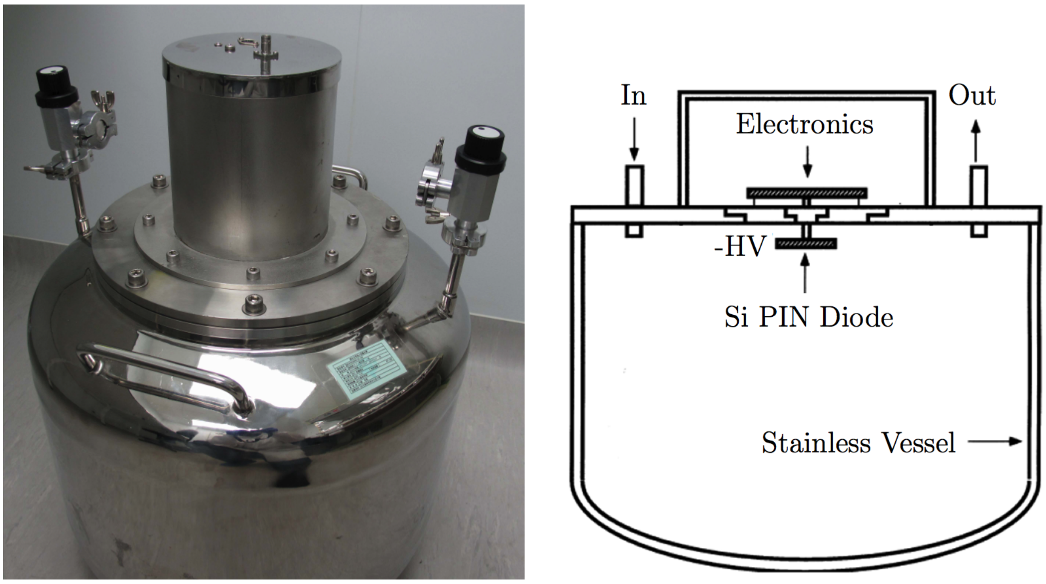

(a) Electrostatic radon detector in operation **(b)** Electrostatic radon detector schematic as shown in [73].

Figure 6.1: Electrostatic radon detector used for all measurements carried out on the radon emanation chamber.

design minimises the distance of the signal cable before pre-amplification as well as providing shielding from external noise. These electronics supply the bias voltage to the diode and provide the voltage rails for the multi-stage amplification of the signal and filter the HV power supply. A negative high voltage is applied to the PIN diode (typically -1500 V) which is then passed through a voltage divider. The HV is then separated into 100 V which is used as the bias voltage and 1400 V which generates an electric field inside the chamber. Two gas flow valves, inlet and outlet, are located on either side of the detector. These have been coated with styrene butadiene rubber (SBR) to prevent radon diffusion.

The daughter nuclei of radon are predominantly positively charged ions. The fraction of positively charged ions was measured to be 88% in 1913 [75] which is still in surprisingly good agreement with the recent measurement of 87.3 ± 1.6% [76]. These ions are attracted to the PIN diode by the applied electric field between the vessel and the diode. Once at the diode, some of the ions undergo α decays which are detected along with their energy. Decays of ^{218}Po, ^{214}Po and ^{210}Po are distinguishable by the amount of energy they deposit: 6.1MeV, 7.9 MeV and 5.4 MeV respectively. Another feature which separates ^{218}Po and ^{214}Po is the time is takes for their activity inside the detector to reach an equilibrium with the ^{222}Rn activity, as shown in

Figure 6.2. The ^{218}Po reaches equilibrium with the ^{222}Rn quickly, however, ^{214}Po takes 4.5 hrs to reach equilibrium, this is due to it being further down the decay chain with two relatively long lived isotopes in between.

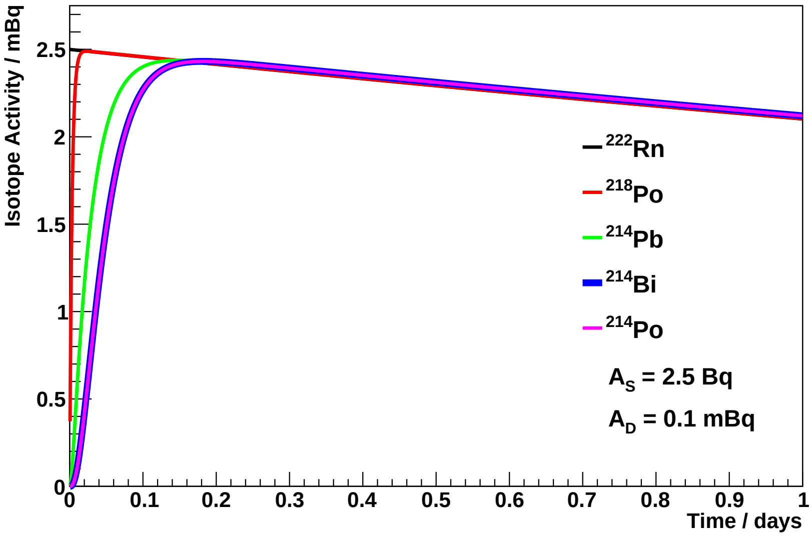

Figure 6.2: Activities of different isotopes in the ^{222}Rn decay chain with respect to time after introduction of 2.5 Bq of ^{222}Rn into a detector with 0.1 mBq background.

6.1.1. Detector Response

The signal from the detector electronics is passed to a NEMbox DAQ system (Wiener NEMbox SU706), which is a programmable field-programmable gate array (FPGA) designed to function as a NIM crate in a small, confined, bench-top unit. The NEMbox is used to trigger and digitise the pulse for storage as well as preventing re-triggering from after pulses. The signal pulses are recorded for offline analysis, which causes a dead time of ~17 ms whilst the data is written to disk. The dead time was calibrated using a signal of known frequency and measuring the detector response, as shown in Figure 6.3. This dead time should have a negligible effect on all measurements except for some calibrations runs when the activity is high, when it must be taken into account.

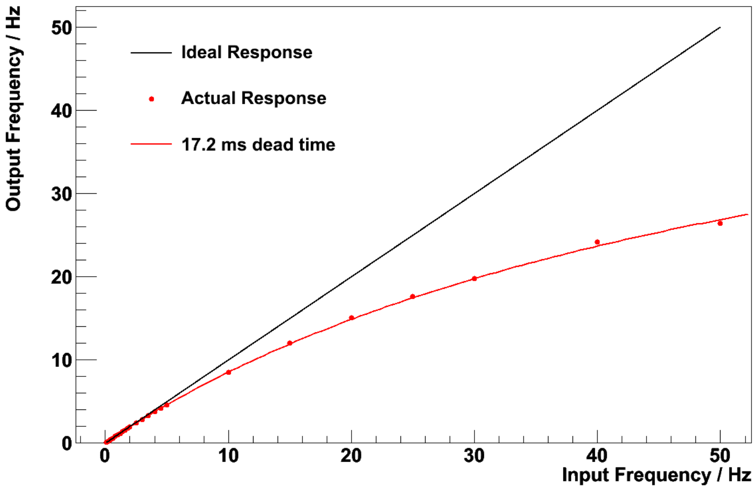

Figure 6.3: Response of DAQ system with varying frequencies. The red dots show the measured values [19].

6.1.2. Detector Efficiency

The detection efficiency of the electrostatic detector was calibrated using a source of known activity (1.32 kBq “flow-through" ^{226}Ra source by Pylon Electronics, RN-1025) and two separate methods. The first was a "spike" method which introduced a known amount of radon into the detector and measured the activity as it decayed, the results are shown in Figure 6.4. Typically helium gas is chosen as the carrier gas over nitrogen, due to impurities such as nitrous oxide in the latter which can effect the detection efficiency by neutralising positive ions.

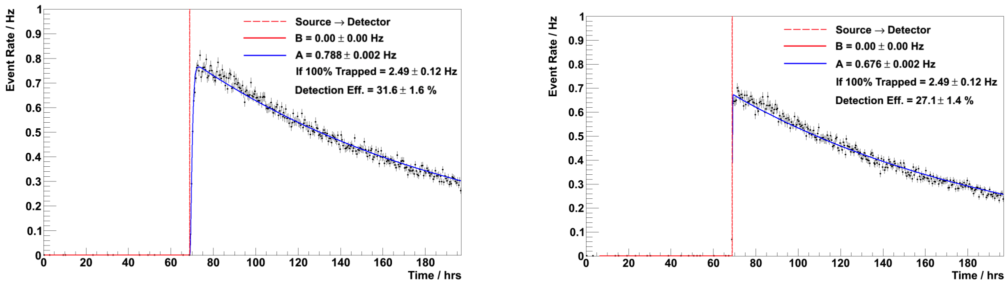

(a) ^{214}Po event rate.

(b) ^{218}Po event rate.

Figure 6.4: The detected event rate of ^{214}Po and ^{218}Po when 2.5 Bq of radon is introduced into the detector volume.

The detection efficiency was determined by taking the ratio of the observed radon activity against the expected radon activity from the calibration source. The resultant detection efficiency was be determined to be 31.6±1.6% and 27.1±1.4% for ^{214}Po and ^{218}Po respectively. This is in excellent agreement with the previous efficiency results, for example detection efficiency measured from over a year ago of 31.5±1.3% and 28.4±1.1% for ^{214}Po and ^{218}Po respectively. This suggests the detector has remained stable over the year even after the HV unit was changed. The associated errors are dominated by the uncertainties on the source activity. It is worth noting that the maximum detection efficiency achievable is 50% for this type of detector, calculated from the solid angle, as this is the probability that the alpha from the decay will be emitted into the PIN diode, rather than away from it. The difference in observed detection efficiency is as a result of neutralisation by contaminates within the carrier gas.

The ^{214}Po efficiency is higher than that of ^{218}Po as it has a lower ionisation potential so is less susceptible to neutralisation making the collection efficiency of ^{214}Po more stable in an environment where there are trace amounts of impurities. A typical background spectrum from the electrostatic detector is shown in Figure 6.5.

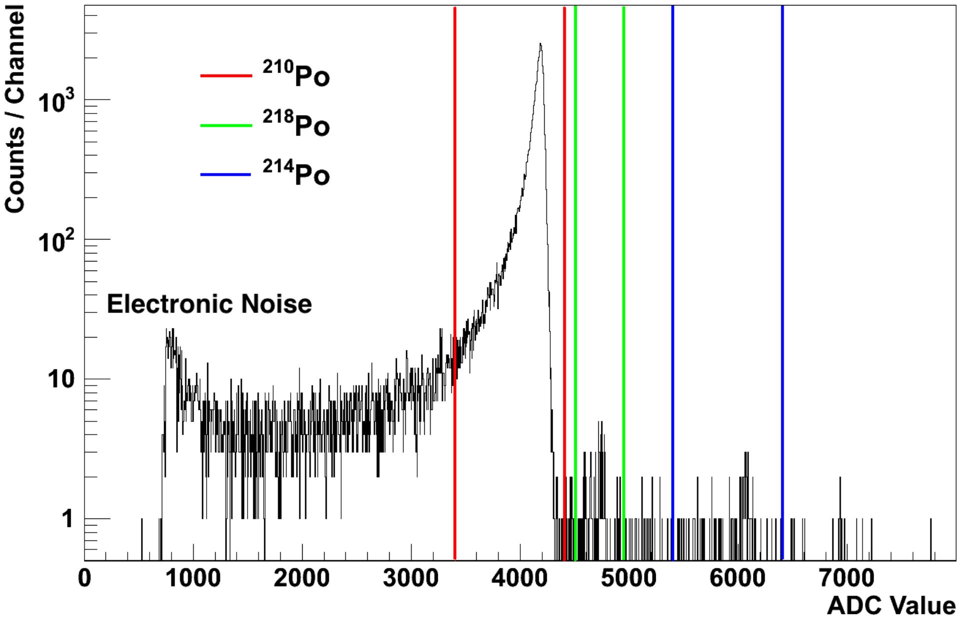

Figure 6.5: Background spectrum of the electrostatic detector with the ^{210}Po, ^{218}Po and ^{214}Po peak ranges displayed from left to right.

In addition, the ^{218}Po efficiency is also affected by the proximity of the ^{210}Po peak, which under normal low activity circumstances, is much larger. The residual ^{210}Po is a decay product of ^{222}Rn (see Figure 3.1) which accumulates over measurements due to its relatively long half-life of 138 days. Even with the excellent resolution of the detector, there is still an overlap between the tail of the ^{218}Po and ^{210}Po, caused by αs which aren't fully contained in the active areas of the Si diode. Therefore, ^{214}Po is by far the best candidate for use in radon measurements.

With the helium replaced by nitrogen the detection efficiency is expected to be reduced as a result of extra impurities which can cause neutralisation. This reduced efficiency was indeed observed with the detection efficiency measured to be 28.1 ± 1.1% and 22.3 ± 0.9% for ^{214}Po and ^{218}Po respectively.

A second calibration method was used to cross-check the efficiency results. This method required gas to flow continuously through the source and into the detector. The result of a flow-through calibration is shown in Fig. 6.6. The calibration was conducted using nitrogen at a flow rate of 4.2 lpm. This translates to a detection efficiency of 29.4 ± 2.0 and 23.2 ± 1.6 for ^{214}Po and ^{218}Po respectively. This agrees closely with the efficiencies found using the "spike" method.

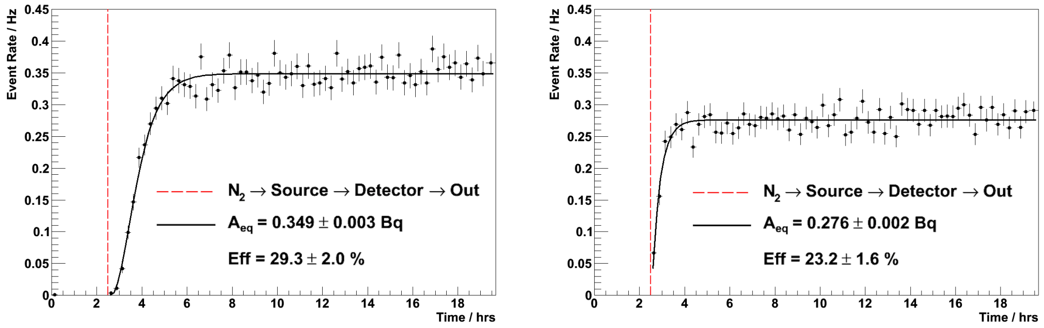

(a) ^{214}Po event rate.

(b) ^{218}Po event rate.

Figure 6.6: Event rates of ^{214}Po and ^{218}Po for a flow through-type calibration run with a flow rate of 4.2 lpm of nitrogen. The black lines show the expected response taking into account the radon half life.

The detection efficiency calibration results using both methods and for helium and nitrogen are summarised in Table 6.1.

Calibration Mode	Measurement Gas	Efficiency / % ^{214}Po	Efficiency / % ^{218}Po
Spike	He	31.6 ± 1.6	27.1 ± 1.4
Spike	N_2	28.1 ± 1.1	22.3 ± 0.9
Flow-through	N_2	29.3 ± 2.0	23.2 ± 1.6

Table 6.1: Electrostatic detector detection efficiency using helium and nitrogen as the carrier gas.

6.1.3. Detector Background Measurement

The ultimate sensitivity of the detector is not only limited by detection efficiency but is also heavily dependent on the background counting rate. Before each measurement, the background level inside the detector is measured to ensure the background is stable and can be correctly subtracted from any activity of radon observed.

Occasionally long background measurements are made to ensure the radon emanation levels inside the detector remain consistent. From a 25 day background measurement, the internal emanation of the detector, for ^{214}Po, was found to be 5.2 ± 0.9 counts-per-day (cpd). For this measurement, the detector was filled with helium to maximise detection efficiency, hence the intrinsic activity of the detector can be determined as 0.27 ± 0.02 mBq or 3.82 ± 0.28 mBq/m^3.

During background measurements ^{210}Po is the dominated peak which is similar in low activity measurements. During calibration measurements when the radon level inside the detector is high, the situation changes and the ^{218}Po and ^{214}Po peaks dominate. Although the ^{210}Po rate does not provide any useful contribution to calculating the radon activity it does provide a reliable way of checking the stability of the detector and the DAQ system, as it stays nearly constant over time with a half-life of 22.2 years [77]. The amount of intrinsic ^{210}Po does increase as more plates out onto the PIN diode over time. This build up could effect the sensitivity of the ^{218}Po measurement as more ^{218}Po decays are drowned out by the tail of the ^{210}Po distribution.

6.1.4. Data Analysis Method

Each detected pulse is recorded via the NEMbox DAQ system as an event in a text file for offline analysis. Each text file records the date and time of 1000 pulses where each pulse is digitised into 1024 sample points. The text files are then analysed using ROOT.

The signal identification and analysis are separated into two steps. Firstly, a peak finding algorithm identifies the number of peaks present per pulse, along with their times and magnitude. From this, the pulses can be categorised into four distinct types as shown in Figure 6.7.

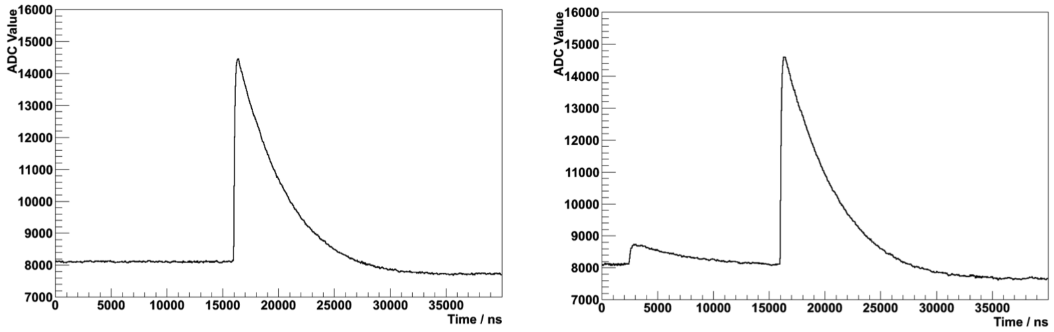

(a) Signal Event

(b) BiPo Event

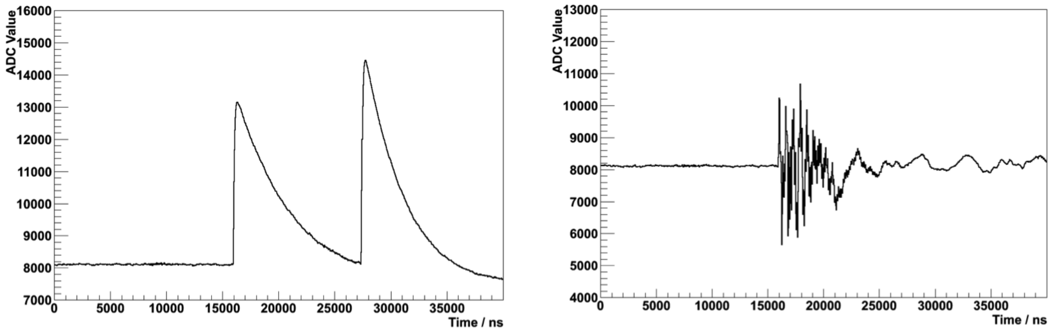

(c) Pile-up Event

(d) Noise Event

Figure 6.7: The four types of events distinguished by the analysis algorithm.

Signal pulses have only one peak (Figure 6.7a) and are passed straight to the second stage. BiPo pulses (Figure 6.7b), characterised by the electron and alpha double peak of the ^{214}Bi and its decay daughter ^{214}Po with a half-life of 164.3 μs, and pile-up pulses (Figure 6.7c) both have two peaks, and which can be distinguished from each other by the relative magnitude of each of the two peaks. These pulses are rare, BiPo pulses contribute to only ∼1% of ^{214}Po pulses and pile-ups are only observed in calibration measurements. Finally, noise pulses have many peaks (Figure 6.7d) which usually have low amplitude and only occasionally have an amplitude high enough to mimic a signal pulse.

To optimise the extraction of the signal amplitude each pulse is fitted with a function. The fitting function was defined as the expected form of a signal from the PIN diode after being passed through the pre-amplifier. The PIN diode signal form was found by shining a fast LED onto the photodiode and observing the output. This treatment removes any single peak pulses which do not have the normal signal pulse-type.

The form of the true signal was found by shining a fast LED onto the PIN diode and reconstructing the output directly. The result was a signal that could be modelled as a sharp linear rise, followed by an exponential decay. The pulse shape parameters are fixed to measured values for this experimental setup, so that even single peaked pulses that do not originate from the PIN diode may be rejected. An example of a pulse with a superimposed fit is shown in Figure 6.8.

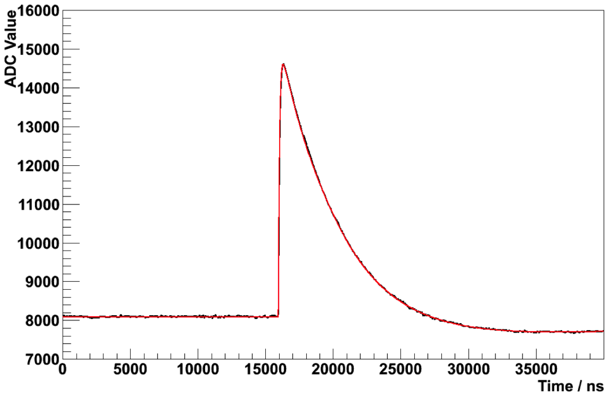

Figure 6.8: A signal event (black) with the fitting function superimposed (red) [19].

6.2. The Minimum Detectable Activity for an Electrostatic Detector

To obtain an Minimum Detectable Activity (MDA) for the electrostatic detector at the Mullard Space Science Laboratory (MSSL), a rigorous definition must first be defined for the sensitivity of a measurement. In this case, the Minimum Detectable

Activity (MDA) as stated in 'Radiation Detection and Measurement' by G. F. Knoll [78] was used. The MDA stated in this thesis represents the detection system sensitivity at 90% CL (unless stated otherwise). The procedure to determine the number of excluded events at the above confidence level is described in Section A.1.

A sample with activity, A_S, corresponding to A_S/λ radon atoms, is introduced into the detector and the detector background, A_D, is intrinsic. The number of radon atoms in the detector at a given time can be found by using:

$$\frac{dN}{dt} = -\lambda N + A_D\,. \tag{6.1}$$

Therefore:

$$\frac{d}{dt}(e^{\lambda t}N) = e^{\lambda t}(\frac{dN}{dt} + \lambda N) = e^{\lambda t}A_D \tag{6.2}$$

and:

$$e^{\lambda t}N = \int e^{\lambda t}A_D dt = \frac{A_D}{\lambda}e^{\lambda t} + C \tag{6.3}$$

Before a measurement the detector is flushed so $N = A_S/\lambda$ at t=0. Therefore C = A_S/λ - A_D/λ and

$$N = \frac{A_D}{\lambda}(1 - e^{-\lambda t}) + \frac{A_S}{\lambda}e^{-\lambda t} \tag{6.4}$$

which is the sum of the background term and the exponentially decaying signal term.

It is a reasonable approximation to consider the signal events to come purely from ^{222}Rn decay without considering the decay chain to ^{214}Po. This approximation can be made as the intermediate isotopes of the decay chain have relatively short half lives compared to any real measurement time. For the number of signal events, S, expected to have been detected after a given time, T, in a detector with detection efficiency, ϵ, with a detector background of zero and:

$$S = \epsilon \int_0^T \lambda N dt = \epsilon \int_0^T A_S e^{-\lambda t} dt = \epsilon \frac{A_S}{\lambda}(1 - e^{-\lambda T}) \,. \tag{6.5}$$

Similarly for the number of expected background events, B, the signal activity is set to zero so that

$$B = \epsilon \int_0^T \lambda N dt = \epsilon \int_0^T A_D(1 - e^{-\lambda t}) dt = \epsilon A_D T - \frac{\epsilon A_D}{\lambda}(1 - e^{-\lambda T}) \,. \tag{6.6}$$

The efficiency of the detector has been measured as ϵ, ~31.6%, and the background measured to be ~7.3 counts per day (cpd), equivalent to $A_D = 0.27$ mBq. From this the MDA for the detector can be calculated by first finding B using equation (6.6), then S_0, which is the minimum number of signal events that are detectable for a given confidence level, using the method described in the appendix (A.20). Finally S_0 is converted into the MDA using equation (6.5). The detector MDA vs. measurement time, T, is shown in Fig 6.9.

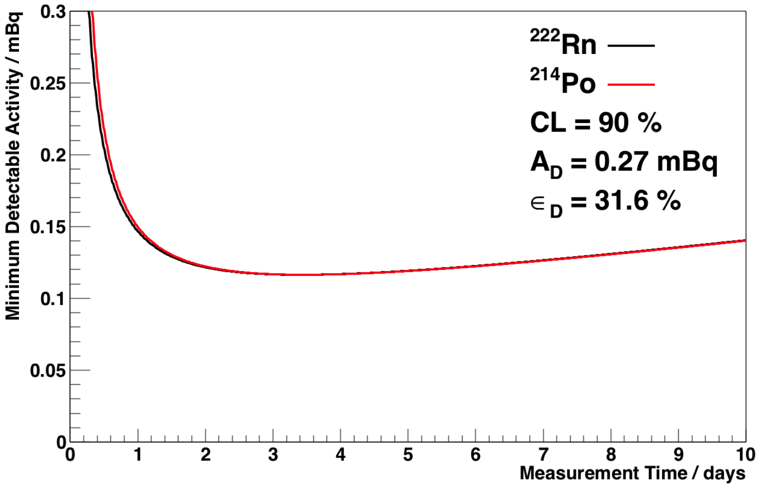

Figure 6.9: The MDA for the electrostatic detector vs. the duration of the measurement. The ^{222}Rn (black) and ^{214}Po (red) results are shown, 0.27 mBq corresponds to 7.3 cpd.

The MDA minimum is reached after ~3 days. After this, the decreasing ratio of signal to background counts takes effect. From this plot, the MDA for the detector can be extracted to be 0.12 mBq or 1.7 mBq/m^3. Since detectors are often subject to contamination, the background levels can vary significantly between detectors. Therefore the relationship between the MDA and the background level can be studied, as shown in Fig 6.10.

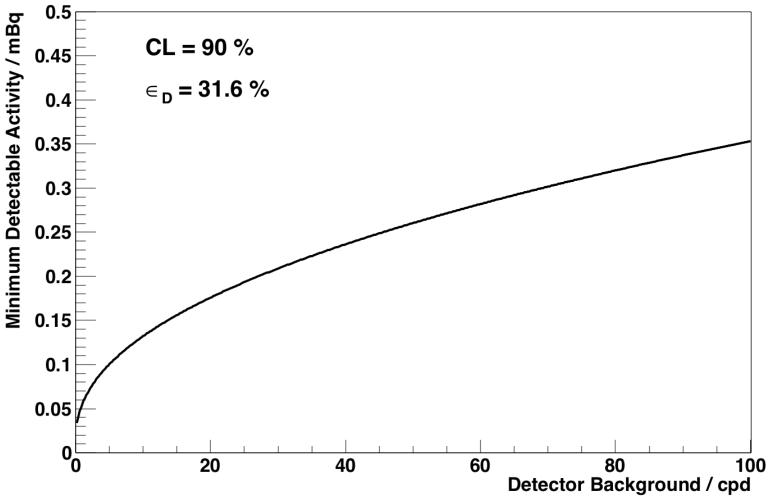

Figure 6.10: The MDA for the electrostatic detector at 90% CL with an efficiency of 31.6 % as a function of the detector background level.

6.3. The Radon Emanation Chambers

A radon emanation chamber was constructed, using stainless steel, in Alabama, United States. It was then assembled and tested at UCL in order to measure the level of radon emanation. The emanation chamber, shown in Fig 3.1, is 152.4 mm in length and 146 mm in diameter resulting in an internal volume of approximately 2.6 litres.

The emanation chamber has two stainless steel flanges, one on each side of a stainless steel tubular body, sealed using copper gaskets. The chamber was leak tested, when first constructed and after opening, in two ways. Firstly, once a sample is sealed inside the chamber helium was used to flush the emanation volume to remove any residual air. A helium leak detector (GasCheck Tesla Helium Leak Detector, ion science) was then used to test all the connections to ensure no leaks above 10^{-6} cc/s were observable. Then the chamber was then sealed under 0.5 bar of pressure and

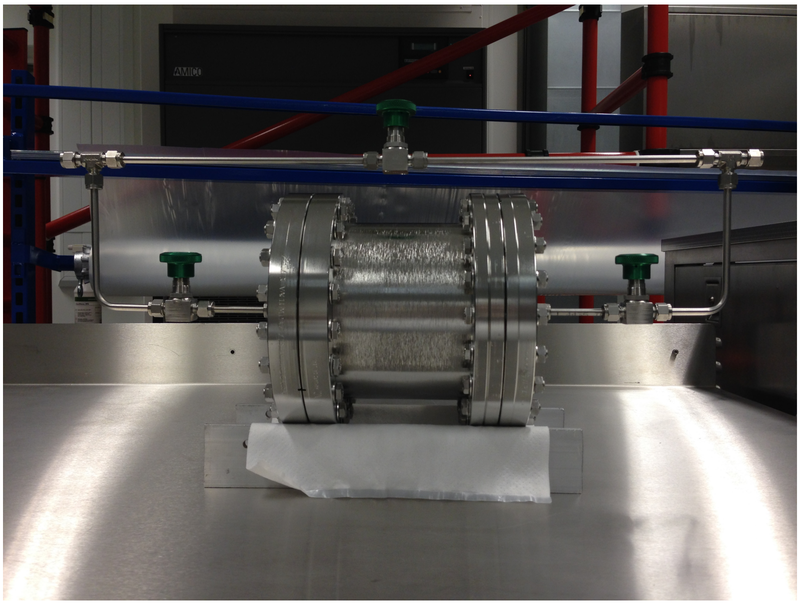

Figure 6.11: The radon emanation chamber fully assembled at MSSL.

the same leak tests were repeated again to ensure no leaks above 10^{-6} cc/s were observable.

For each new sample the emanation chamber is purged using helium for 200 times the volume of the chamber (VC) to ensure other gases are completely removed, before it is sealed under atmospheric pressure. The chamber is then left to emanate for at least 1 week before the gas inside is transferred directly into the electrostatic detector for measurement.

6.3.1. Background Measurement

Having established that the radon emanation chamber was leak-free the chamber was then transported to MSSL where it was reassembled. It was then connected to the radon detector directly, as shown schematically in Figure 6.12. The entire line with the chamber attached was flushed using helium and a leak test was again performed to ensure the line was air tight. The chamber itself remained sealed for the entire process. After flushing with helium for 100 VC, the chamber was sealed under atmospheric pressure in order to measure the background emanation from the chamber itself.

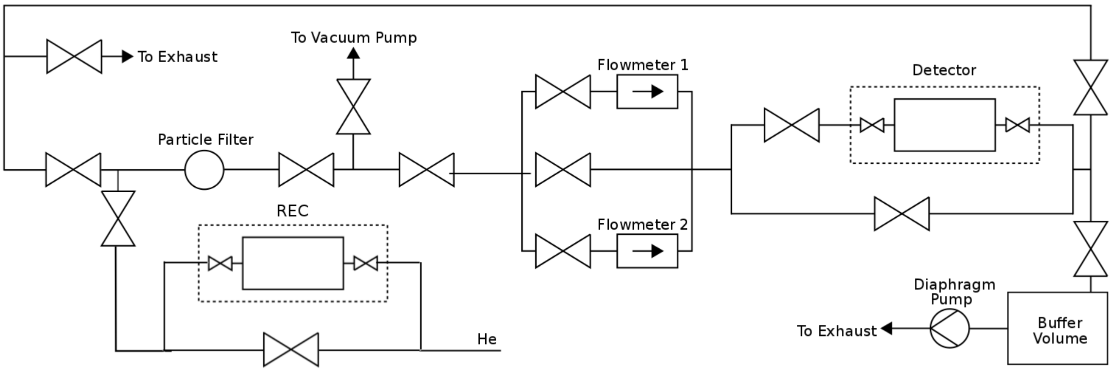

Figure 6.12: Schematic diagram of the design of the entire RnCL built for SuperNEMO measurements.

After 30 days when the level of radon inside the chamber had reached equilibrium, it was flushed into the detector using 25 litres of helium, ~10 VC. The process is shown in Fig 6.12. The results after a one week measurement are shown in Fig 6.13. The number of detected signal events inside the radon detector are plotted with a vertical dashed line signifying the time of sample transfer into the radon detector for measurement. A polynomial fit is applied to the data prior to the sample measurement which is taken as the radon detector background (B). The data post transfer is fitted with a exponential decay curved based on the radon half-life. The radon activity (A) is determine by extrapolating back to the moment of transfer (t_0).

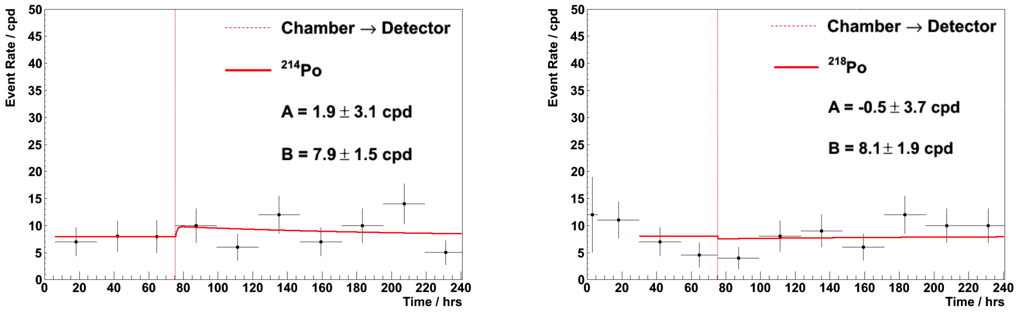

(a) ^{214}Po event rate.

(b) ^{218}Po event rate.

Figure 6.13: The detected event rate of ^{214}Po and ^{218}Po as measured by the alpha detector.

From the results shown in Fig 6.13, a limit may be placed on the emanation chamber background, calculated using:

$$A_L = \frac{R_D \times 1.64\,(\text{at } 90\%\ \text{C.L.})}{86400\,(\text{secs/day})} \tag{6.7}$$

where A_L is the limit at 90% confidence level (C.L.) and R_D is the uncertainty on the detected rate. Correcting for the detection efficiency of the detector and the transfer efficiency, ε, the true activity A_T is:

$$A_T = \frac{A_L}{\varepsilon(1 - e^{-N_v})}\,, \tag{6.8}$$

where N_v is the number of volumes of the chamber flushed into the detector. Finally, correcting for the initial activity levels from equilibrium;

$$A = A_T(1 - e^{-\lambda t})\,. \tag{6.9}$$

Hence, the sensitivity limits on ^{214}Po and ^{218}Po (90% C.L.) are:

$$^{214}\text{Po} < 0.187\ \text{mBq} \quad \text{and} \tag{6.10}$$

$$^{218}\text{Po} < 0.246\ \text{mBq}\,. \tag{6.11}$$

6.3.2. The Radon Harbouring Hypothesis

During measurements of materials through which radon can diffuse, it was observed some residual radon from the atmosphere can diffuse into the materials such as the duracon and scintillator. Even after flushing such materials can still out gas radon, hence producing a higher activity value.

This is known as the radon harbouring hypothesis and it was demonstrated using the radon emanation chamber and a sample of duracon. The sample was placed into an emanation chamber which was then purged with 200 volumes of radon-free helium and left to emanate at atmospheric pressure. After 7 days, the gas inside the chamber was transferred into the radon detector for measurement, as shown in Figure 6.14. After transfer the chamber was again flushed with helium and sealed at atmospheric pressure. After 10 more days (17 days inside chamber) a second transfer was made of the gas inside the chamber to the radon detector which showed no positive signal, as shown in Figure 6.14. This result is of particular interest as there are components inside the tracker that are made from materials which have a sizeable radon diffusion length.

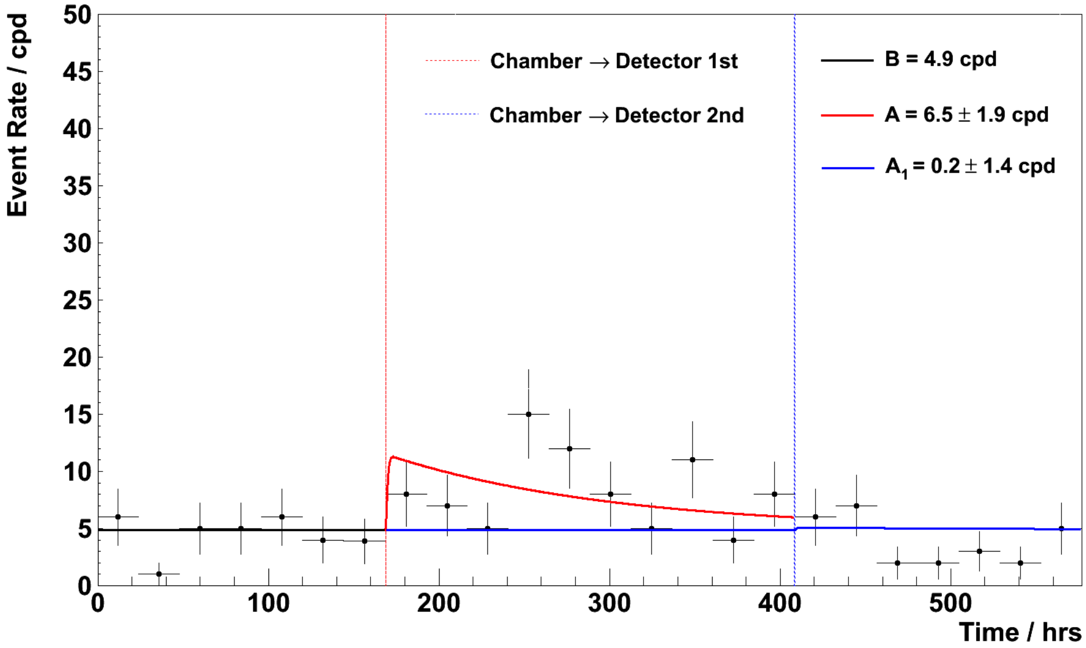

Figure 6.14: The measured ^{214}Po activity from the first and second transfers, demonstrating the radon harbouring hypothesis. The result from the first transfer is fitted with a red line whilst the result from the second transfer is fitted with a blue line.

6.4. The Radon Concentration Line

The modified electrostatic radon detector has demonstrated a stable low background making it one of the most sensitive compact detectors in the world. However, it is still one order of magnitude away from the SuperNEMO radon requirements. Therefore, a new technique and system had to be developed in order to further improve its sensitivity.

A radon trapping system known as the Radon Concentration Line (RnCL) was developed to be used in conjunction with the electrostatic radon detector. The RnCL system essentially consists of a stainless steel trap containing ultra radio-pure activated carbon which is cooled to -50 °C. The cooling significantly improves the charcoal's ability to capture radon [79]. Large volumes of gas can be flown through the trap where the radon is adsorbed. After the gas volume to be measured has passed through the charcoal trap, it is sealed and the concentrated radon sample can then be heated, releasing the radon, which can then be flushed into the electrostatic detector for measurement.

The radon concentration line was built to increase the sample volume of gas measurable using the radon detector. This significantly increased the sensitivity of the detector in terms of Bq/m^3. The design of the RnCL is similar to the MoReX line [80] developed in Heidelberg, however, the design has been simplified for increased portability. The setup of the RnCL is shown in Figure 6.23

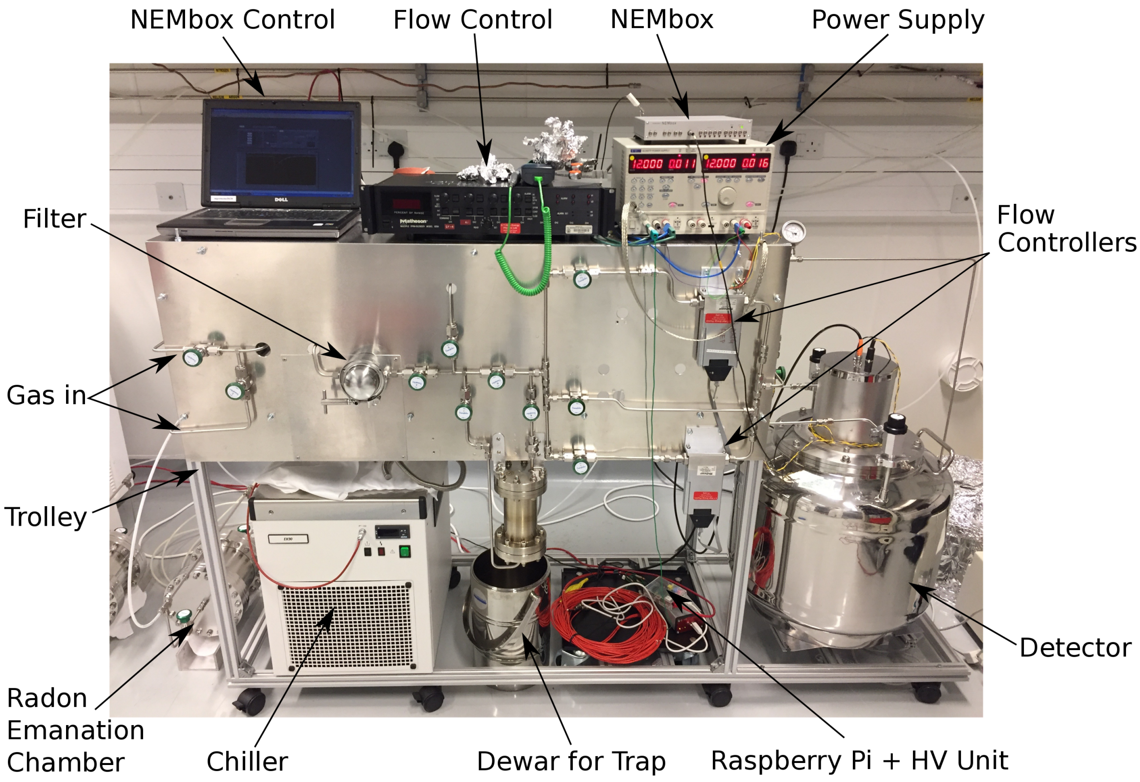

Figure 6.15: The radon concentration line setup.

The RnCL was designed with vacuum capability and a vacuum pump attachment. However, the detector demonstrated better and more stable performance when the purge gas is simply transferred directly with the detector at atmospheric pressure. Due to the small volume of the trap, 25 litres of helium is enough to ensure more than 100 volume replacements and almost complete transfer of the released radon into the detector. The increase in operational pressure from 1 bar to 1.36 bars was shown to have a negligible effect on the detector performance.

An additional buffer volume and a diaphragm pump was added to the RnCL exhaust which enabled the possibility to actively draw gas through the line. This was necessary for the measurement of gas volumes at low or atmospheric pressures as at least 0.2 bars of overpressure is required to achieve the nominal flow rate, 7 lpm, through the RnCL for measurement. Therefore, the pump is essential as the completed trackers cannot safely accommodate a large over-pressure.

6.4.1. Modifications to the RnCL

The initial rendition of the RnCL successfully demonstrated the ability to surpass the sensitivity required for radon measurements of the SuperNEMO tracker. In order to further improve the trapping and transfer efficiency of radon in large gas volumes as well as minimising the systematic uncertainties several modifications were made to the RnCL which was then re-calibrated to quantify the effects of these modifications.

6.4.2. Gas Line Filter

A series of particle filters were used to prevent any particulates contaminating the electrostatic detector. However, positive levels of radon emanation were observed which were attributed to a gas line filter made of a black plastic material. An emanation test was therefore performed to test this hypothesis, the result showed the activity of the gas line and particle filter to be 7.4±1.0 mBq.

The gas line filter was replaced with a Swagelok stainless steel filter with a 0.5 micron pore size. The entire gas line was filled with helium and sealed at atmospheric pressure for radon to build up from emanation. Then, after 5 days, the gas was transferred directly into the detector for measurement. The results are shown in Figure 6.16.

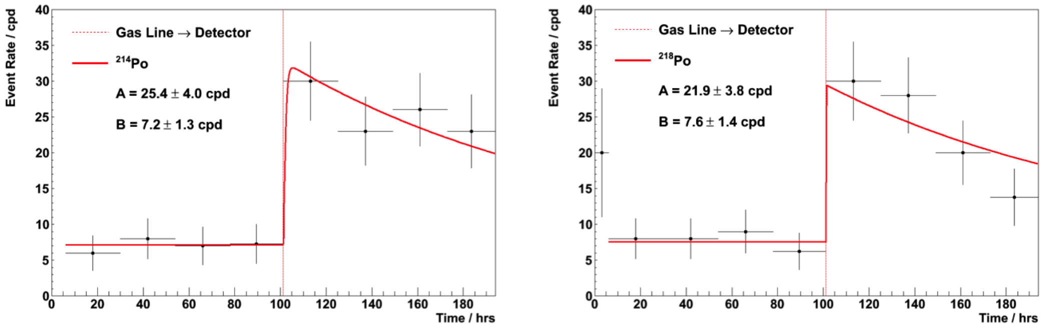

(a) ^{214}Po event rate. **(b)** ^{218}Po event rate.

Figure 6.16: The detected event rate of ^{214}Po and ^{218}Po from the gas line measurement.

From this, an activity of 1.8±0.3 mBq can be extracted, using:

$$A_O = \frac{\text{cpd}}{86400} \tag{6.12}$$

where A_O is the observed activity in Bq. Correcting for the detection efficiency of the detector and the transfer efficiency, ε, the true activity A_T is:

$$A_T = \frac{A_O}{\varepsilon(1 - e^{-N_v})}\,, \tag{6.13}$$

where N_v is the number of volumes of the chamber flushed into the detector. Finally, correcting for the initial activity levels from equilibrium;

$$A = A_T(1 - e^{-\lambda t})\,. \tag{6.14}$$

The result suggests the particle filter was indeed the major contributor to the radon background.

6.4.3. Trap Cooler

A new cooler (EK90 Immersion Cooler by Thermo Scientific) was purchased which was capable of reaching temperatures of -90 °C instead of -30 °C previously. This lower temperature should increase the trapping efficiency of the activated carbon, this is shown in Section 6.4.6.

6.4.4. Trap Modification

The carbon trap underwent a complete redesigne to improve the trapping and transfer efficiency. Due to the design of the old carbon trap it was very difficult to ensure all the Swagelok connections were tightly sealed and it was impossible to carry out a leak test on the system. During operation the pressure required to flow gas through the trap at a constant rate went up over a period of 12 months of use. This also coincided with a fall in the trapping efficiency which led to the hypothesis that a blockage could have occurred at the gas outlet and a leak could be present at a point above the active carbon as shown in Figure 6.17.

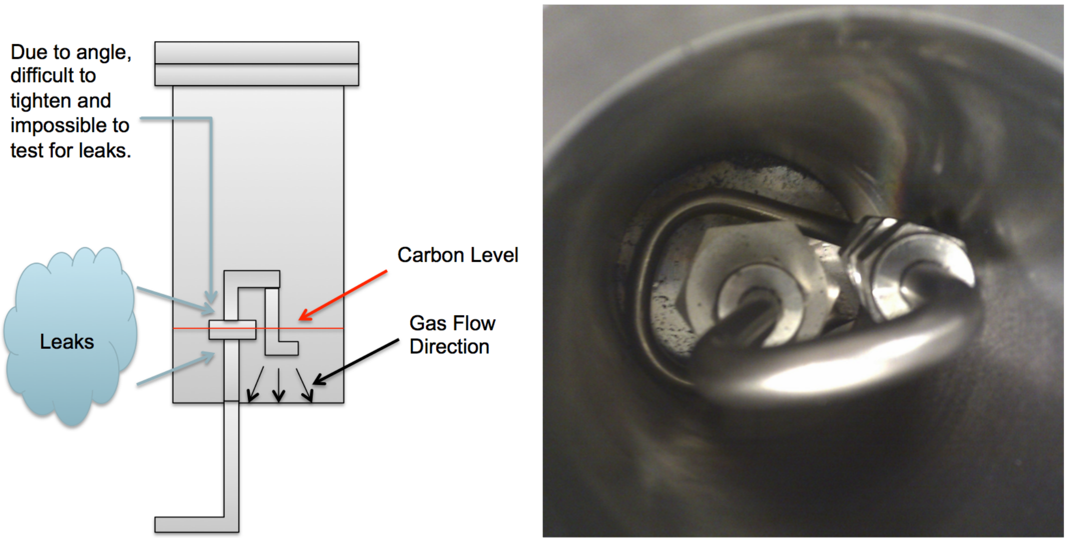

(a) Possible issues with the old carbon trap. **(b)** Inside of the old trap.

Figure 6.17: The schematic on the left shows the possible issue with the old trap design which can be compared to the real picture taken of the inside of the carbon trap.

A new trap was developed in order to minimise the risk of a leak developing in the pipe work within the trap. It has a detachable base flange which allows easy access to tighten the pipe work, as shown in Figure 6.18.

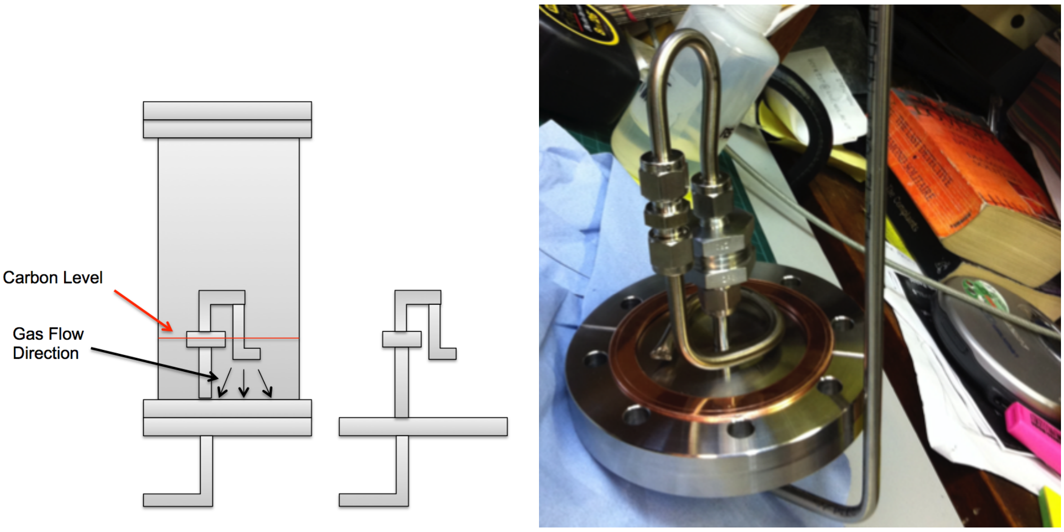

(a) New trap schematic. **(b)** Base flange with pipework.

Figure 6.18: The new carbon trap design which has a detachable base flange thus allowing easy access for pipe work installation.

The new trap has a slightly larger volume, 0.5 l compared to 0.4 l of the old trap. From the transfer some activated carbon was also lost, resulting in 52.5 g of carbon in the new trap instead of the 57 g present in the old trap. The new trap was installed onto the RnCL and the trap emanation background was measured.

To determine the trap background, the trap was first cleared by heating to 210 °C and flushing continuously with high purity helium. Then the trap was sealed with helium inside under atmospheric pressure to emanate for 7 days. After 7 days, the gas inside the trap is transferred into the detector using helium for measurement. The resultant plots are shown in Figure 6.19.

The activity was calculated to be 0.48±0.14 mBq and 0.42±0.14 mBq for ^{214}Po and ^{218}Po respectively. This is slightly higher than the old trap which was found to be 0.23±0.11 mBq, but the two results are consistent within ∼1.3 sigma.

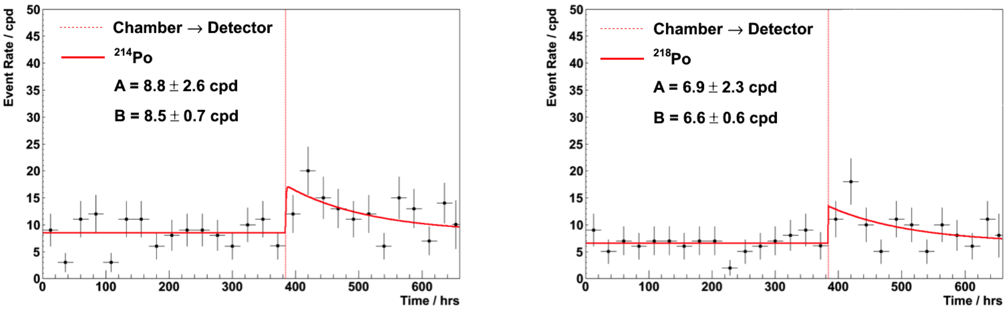

(a) Event rate of ^{214}Po.

(b) Event rate of ^{218}Po.

Figure 6.19: The new carbon trap backgrounds.

6.4.5. HV Upgrade

The RnCL was previously run on a multi channel CAEN HV unit and it required a very stable supply of 1500 volts of which 100 volts is used to create the reverse bias on the PIN diode. Large shifts were observed in the spectrum from the electrostatic detector which was traced back to fluctuations on the output of the Caen HV unit. A single channel HV unit was purchased as the replacement which was connected and controlled using a Raspberry Pi computer. This enables remote monitoring of the HV voltages and for large voltage fluctuations, an email alert can be sent out. The new HV unit also provides the added bonus of making the RnCL a completely stand alone unit.

6.4.6. RnCL Calibrations

To quantify the effects of all the modifications a flow-through calibration using nitrogen was carried out with the new HV unit, cooler and radon trap. The idea of the flow-through calibration is to mimic the same conditions as a real measurement of the SuperNEMO tracker using the RnCL. The steps are as follows;

1. First attach the radon source (used previously for the spike calibration) into the RnCL setup then flush with nitrogen at 7 lpm continuously to exhaust in order to remove the built up radon.

2. Flush the source for 3 hours, to ensure all residual radon is removed, then flow nitrogen through the radon source and the detector, then out to exhaust at a constant

rate of 7 lpm. Measure the output activity for ∼24 hours to ensure the activity through the detector remains stable. This flow-rate was selected as it is the maximal flow rate which can be achieved during SuperNEMO tracker measurements.

3. After 24 hours, divert the gas from the source through the trap first before the detector and then out to exhaust, maintaining the same flowrate of 7 lpm.

4. After 20 hours of trapping seal the trap and source.

5. Start to heat the trap for the transfer, in the meantime remove the radon source and clear the detector by flushing continuously with helium for 10 volume replacements to remove any residual radon. Once cleared, seal the detector under atmospheric pressure.

6. Once the trap has reached above 200 °C, transfer the gas contents into the detector for measurement.

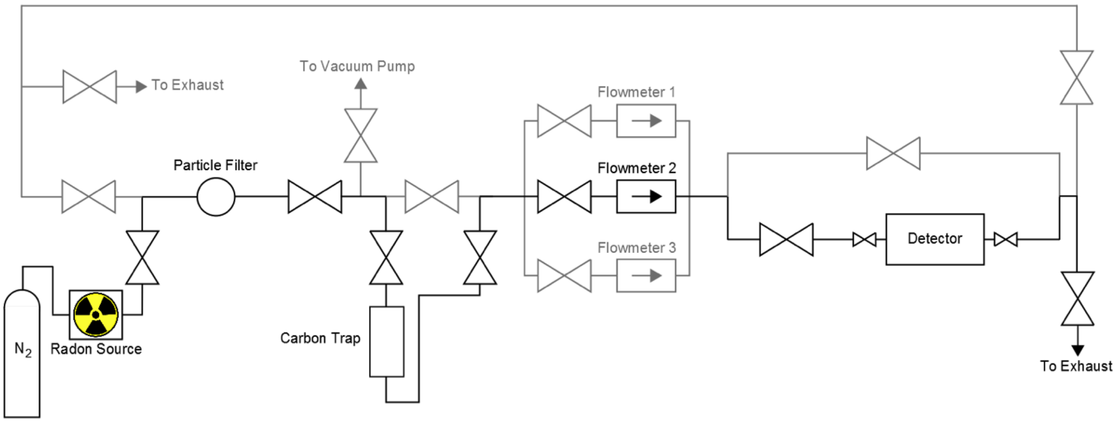

Figure 6.20: Schematic diagrams showing the RnCL setup during a flow-through calibration using a radon source. The section highlighted of the RnCL is used for trapping of radon from the carrier gas.

From this calibration all the necessary information for a tracker measurement can be extracted. The activity in the radon detector during the flow-through calibration run can be seen in Figure 6.21. The activity in the detector from steps 1 to 5 can be seen in Figure 6.21a and steps 1 to 6 in Figure 6.21c.

The result from this calibration can be compared to the same calibration measurements taken before the modifications were made to the RnCL, see Figure 6.21b and Figure 6.21d. Comparing Figure 6.21a and Figure 6.21b, in each case the radon

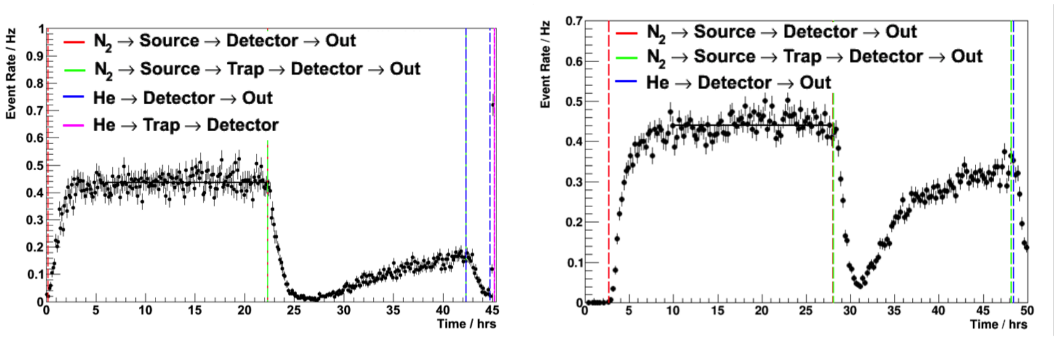

(a) New trapping efficiency **(b)** Old trapping efficiency

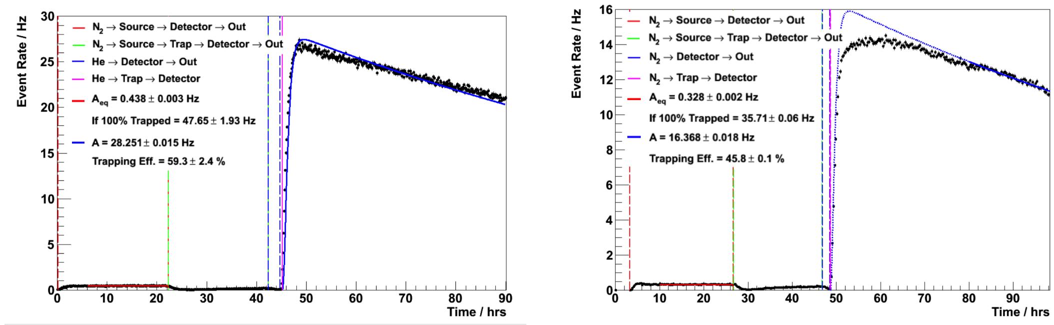

(c) New trapping/transfer efficiency **(d)** Old trapping/transfer efficiency

Figure 6.21: Comparison of the activity inside the radon detector using the new (plots a and c) and old (plots b and d) carbon trap.

activity reaches a stable level in the first 20 hours. Then when the trap is introduced into the system the level drops sharply in both cases: slightly lower in the modified system suggesting a better trapping efficiency. The key change seen after the modifications is in the rate of activity rises after the initial fall. In the case of the old trap there is almost an equally sharp rise which slightly tales off, whereas in the modified trap the rise is more gradual. The hypothesis for this loss of trapping efficiency is due to the activated charcoal becoming saturated with radon. The radon is released and then captured, in this way it is pushed along the charcoal until it is finally free to recombine with the carrier gas post-trap. By lowering the trap temperature the charcoal can hold more radon and hence takes longer to become saturated.

To quantify the trapping efficiency, the specific activity at the output of the source must first be calculated;

$$a_S^{eq} = \frac{A_S}{f_S/\lambda} = \frac{1.32 \pm 0.05\text{kBq}}{55.7 \pm 2.7\text{m}^3} = 23.7 \pm 1.5 \text{ Bq/m}^3\,, \tag{6.15}$$

where A_S is the activity of the source and f_S is the flowrate through the source, in this case 7 lpm. The equilibrium activity inside the detector can be determined using

$$A_D^{eq} = \frac{A_S}{1 + f_S/\lambda V_D} = 1.7 \pm 0.1 \text{ Bq}\,. \tag{6.16}$$

The measured event rate inside the detector at equilibrium was 0.438 Hz which translates to a detector efficiency of 27.5 ± 1.8%. This is consistent with the efficiency found during flow-through calibration of 29.3 ± 2.0%.

By monitoring the activity of the gas after it has gone through the carbon trap it is possible to then calculate the amount of radon trapped within the carbon. Taking the ratio between this value and an idealised case where 100% of the radon is trapped gives the trapping efficiency as a function of time which is shown in Figure 6.22.

From Figure 6.22 it can be seen that the initial trapping efficiency is very close to 100% but falls off with time. This could be a result of the radon retention time of the carbon material. The amount of radon after 20 hours can then be compared with what is observed inside the detector after the transfer to obtain the transfer efficiency.

It can be seen from Figure 6.22c and Figure 6.22d that the modifications to the trap have resulted in almost a factor 2 improvement in the trapping and transfer efficiency of the RnCL system.

6.5. Radon Concentration Line Sensitivity

The MDA of the electrostatic detector was defined in Section 6.2. The RnCL is able to improve upon this MDA in terms of Bq/m^3 by allowing the measurement of radon

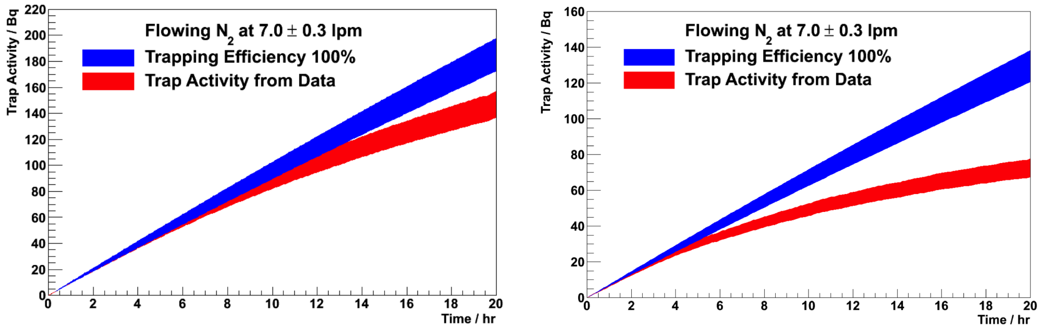

(a) Radon activity in new trap.

(b) Radon activity in old trap.

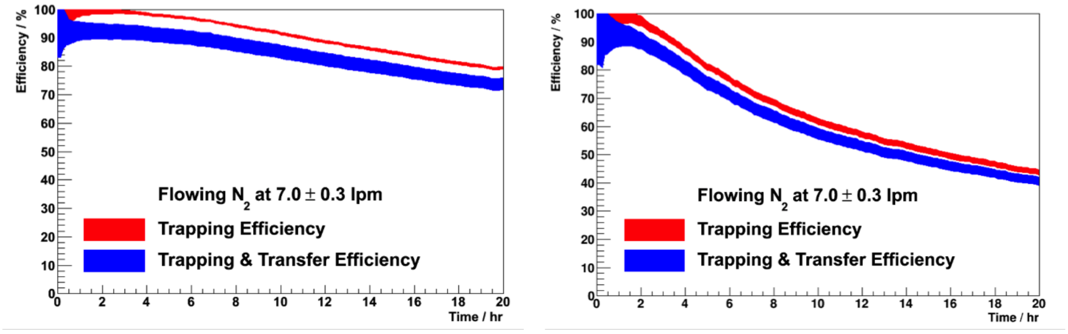

(c) Trapping and transfer efficiency.

(d) Trapping and transfer efficiency.

Figure 6.22: Comparison of trapping and trapping/transfer efficiencies of the new (plots a and c) and old (plots b and d) carbon trap.

from a larger gas volume inside the same electrostatic detector. Therefore, the MDA improves as a function of volume of gas [19], as shown in Figure 6.23.

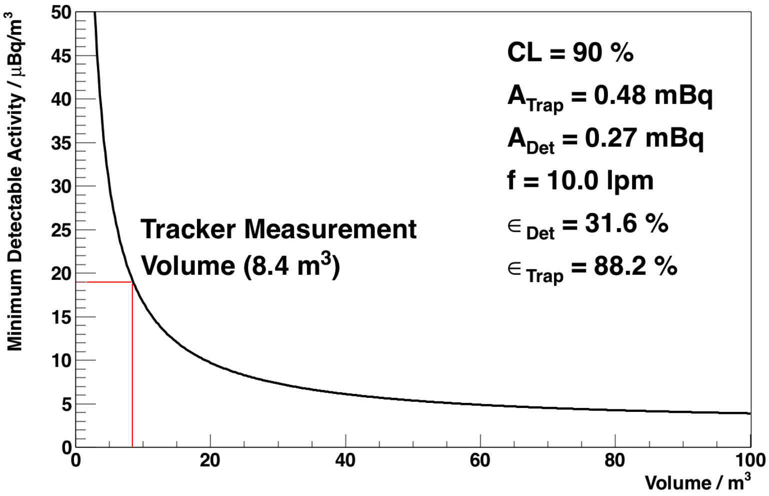

Figure 6.23: The MDA as a function of gas volume.

A significant improvement can be seen and sensitivities as low as 5 µBq/m^3 can be achieved. There is however diminishing returns as the volume of gas required to improve the MDA increases exponentially. At the calibrated volume of 8.4 m^3 a sensitivity of $<$ 20 µBq/m^3 can be reached which is more than enough to meet the SuperNEMO requirements.

Chapter 7.

Radon Measurements For SuperNEMO

The radon detector and the RnCL have both demonstrated excellent performance and, when used in conjunction, the capability to reach and surpass the target radon sensitivity required for the SuperNEMO demonstrator. The RnCL allows the monitoring of radon emanation from quarter trackers during and after construction providing essential information on meeting the radon requirement. The ability to measure a fully instrumented tracker volume is a key aim as radon emanation is area and geometry dependent.

The key measurements carried out using the radon detector alone, and in combination with the RnCL, are detailed here, including the measurement of three of the four demonstrator quarter trackers, radon emanation from the SuperNEMO gas system and the radon content of SuperNEMO gases.

7.1. Gas Cylinders

A measurement programme of gas cylinders was undertaken to quantify their radon content, under the same conditions as during a tracker measurement. This was essential in order to disentangle the radon activity of the carrier gas from radon emanated in the tracker measurements. It was shown that the gas used in the tracker measurements is one of the main contributors to the radon background.

7.1.1. Cylinder Activity

The information of interest from gas cylinders is the specific activity in Bq/m^3. As the physical volume of a cylinder remains constant but the volume of gas contained within it changes as it's emptied, if the radon is evenly distributed, the specific activity of the output gas can be modelled as;

$$\frac{dN_G}{dt} = A_G - \lambda N_G - \frac{fN_G}{(V_G - ft)}, \tag{7.1}$$

where N_G is the number of radon atoms in the gas cylinder, A_G is the specific activity of the gas, f is the flow rate and V_G is the total volume of gas (at STP) contained in the cylinder at the start of the measurement. Depending on the extraction flow rate a fraction of radon is removed from the bottle which is replaced with emanated radon. The specific activity in the cylinder as a function of the volume of gas remaining in the cylinder is shown in Figure 7.1.

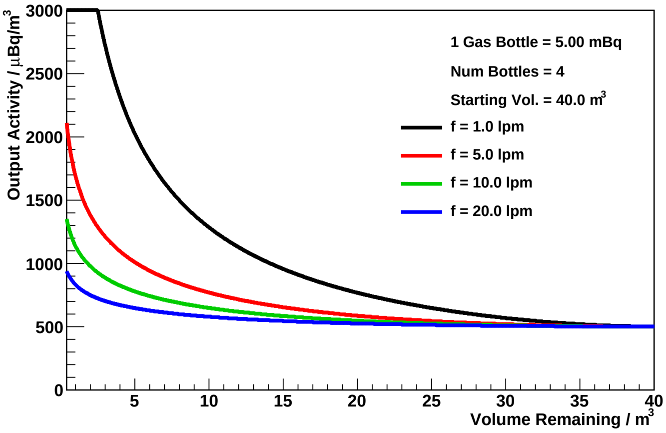

Figure 7.1: Specific activity of four cylinders, each 50 litres in volume and starting at 200 bars, as a function of the volume remaining. A combined activity of 20 mBq is used for radon emanation with a starting gas volume of 40 m^3 [19].

For SuperNEMO tracker measurements only flow rates between 7 − 14 lpm are used with full cylinders and no more than 60% of the total volume of gas used, hence the output activity is approximately uniform over time. To ensure the radon measured is emanation from the cylinder alone and not as a result of radon introduced during the filling, each cylinder was left sealed for more than 3 weeks before being measured to ensure the radon activity is at equilibrium.

7.1.2. Measuring Full Cylinders

The experimental procedure is to first heat then clear the trap of any residual radon, then cool the trap to - 45°C. Once cooled, flow the sample gas through the trap to exhaust for $\sim$ 20 hours then seal the trap. Finally, the trap is heated and the radon transferred to the detector for measurement. A typical measurement of a nitrogen cylinder is shown in Figure 7.2b.

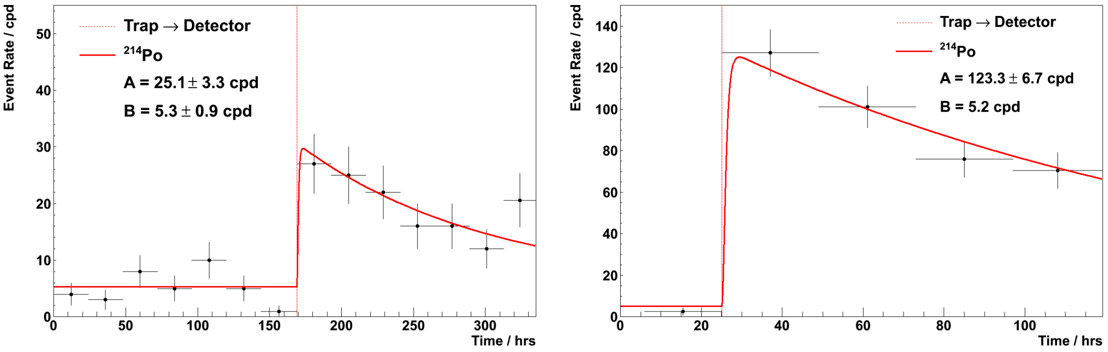

(a) Line Only

(b) Line and Gas

Figure 7.2: (a) ^{214}Po activity of both supply line and 0.075 m^3 of helium. (b) ^{214}Po activity of both line and 10.7 m^3 of nitrogen.

The activity of radon in the detector immediately after transfer from the trap is given by:

$$A_D = \epsilon_{tr} A_C \left(1 - e^{-\lambda t_C}\right) + \epsilon_{tr} \left(\epsilon_T \left(t_f\right) A_G + \frac{\epsilon_T \left(t_f\right) f a_G}{\lambda}\right) \left(1 - e^{-\lambda t_f}\right) e^{-\lambda t_{trans}} \tag{7.2}$$

where ϵ_{tr} is the transfer efficiency, ϵ_T is the trapping efficiency taken from Figure 6.21, A_C is the intrinsic activity of the RnCL carbon trap, A_G is the activity of the gas line and a_G is the specific activity of gas from cylinders [19]. The relevant timings for this measurement are as follows

- t_C: time between clearing the trap and detector transfer.
- t_f: time that the line is in contact with the trap.

- t_{trans}: time between stopping collection and detector transfer.

The measurement shown in Figure 7.2b produced a result of 4.53 ± 0.25 mBq with $t_C = 1462$ min, $t_F = 1070$ min and $t_{trans} = 128$ min. Applying the trapping and transfer efficiencies found from the flow-through calibration in Section 6.4, the specific radon activity of the gas is extracted as 957 ± 132 µBq/m^3. This translates to a mean intrinsic activity per bottle of 9.6 mBq.

The same measurement but with helium cylinders produced a result of 77 ± 13 µBq/m^3, resulting in a mean intrinsic activity per bottle of 0.8 mBq. The difference between the intrinsic activity of helium and nitrogen cylinders is surprising as the supplier states they are made from similar materials. It could be a result of the natural variation in the contamination of the steel used in producing the helium and nitrogen cylinders.

Several more cylinders of nitrogen and helium were measured to determine the variation of radon activity between cylinders. The results showed large variation between different batches of cylinders from the same supplier, as shown in Table 7.1. Since the carrier gas is the largest background during a tracker measurement, it is critical the cylinders used are measured separately in order to find the activity of the carrier gas to be subtracted from the measured result. This doubles the time required for each tracker measurement as well as introducing large uncertainties resulting from extrapolation of radon levels of the carrier gas.

7.1.3. Cylinder Gas Activity Effects On MDA

The large and variable radon content of the carrier gas can impact the MDA achievable by the RnCL. A plot of the RnCL MDA as a function of the carrier gas activity is shown in Figure 7.3. It can be seen in order to achieve better than 0.15 mBq/m^3 of sensitivity the activity of the supply gas must not exceed 1.5 mBq/m^3.

7.2. Gas Purification System

A gas purification system (GPS) was devised and constructed which is able to suppress the radon activity in a carrier gas. The system was developed to remove

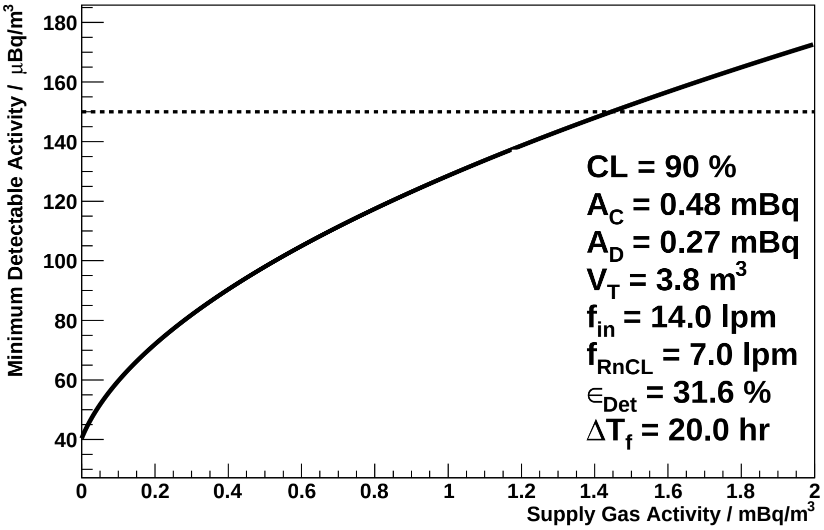

Figure 7.3: Sensitivty of the RnCL for a C-section measurement as a function of the input gas activity.

one of the greatest sources of systematic uncertainties as a result of the relatively high content and variability of radon in N_2.

The radon trap system was designed and built at CPPM which was estimated to suppress radon by a factor 20 for nitrogen and 2 × 10^{10} for helium [81]. A design schematic is shown in Figure 7.4, which essentially consists of two freezers operated at temperatures of -50°Cand -80°Ccontaining 1.5 kg and 0.5 kg of activated charcoal each respectively.

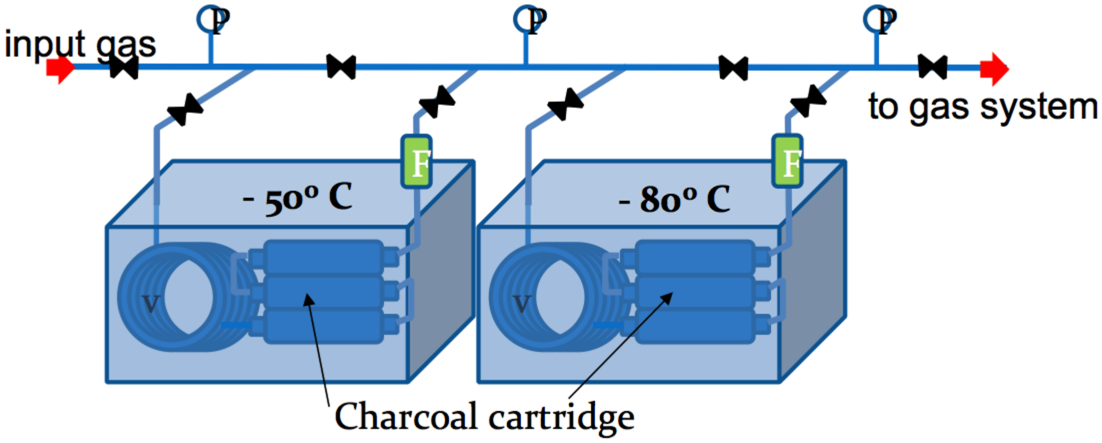

Figure 7.4: Schematic of the GPS developed at CPPM.

The system works by passing the carrier gas through the activated charcoal where radon is adsorbed. The activated charcoal is housed in stainless steel cartridges that can be replaced if necessary. The low temperature improves the radon capture efficiency of the charcoal, it also ensures that radon does not emanate from the charcoal itself so the system does not require very radio-pure charcoal to work. The GPS was delivered to MSSL and installed in May 2014. The temperature was monitored regularly to ensure it remained stable.

7.2.1. Background Measurement

The first measurement carried out after installation was the background of the GPS itself. The GPS was thoroughly flushed using helium to ensure any residual air was replaced with helium. It was then left to emanate immersed in helium under atmospheric pressure.

The system was left for 21 days to allow any residual radon to decay away and the radon level inside the trap to reach an equilibrium. The gas inside the GPS was then transferred into the radon detector for measurement. The resultant activity measurement is shown in Figure 7.5.

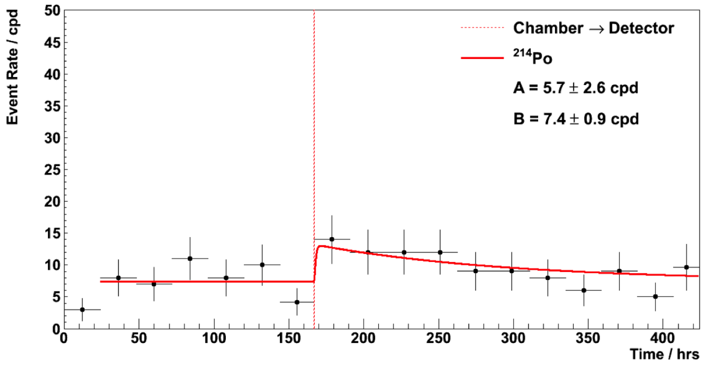

Figure 7.5: Result from the measurement background activity of the GPS after 21 days of emanation time.

From this result a contribution of 1.6 ± 0.7 cpd of background can be expected from the GPS over a 24 hour trapping and transfer measurement period.

7.2.2. Radon Suppression Measurement

In order to verify the GPS suppression of radon in the carrier gases a measurement was carried out on 4 full cylinders of zero-grade nitrogen. The procedure for this measurement is similar to that of a c-section measurement [82], as described in Section 7.4.3.

1. The trap is heated to above 210°C to clear it of any residual radon.

2. Once the trap is cooled to below -40°C, start to flow the sample gas, first through the GPS, then through the RnCL trap and out to exhaust at 7 lpm for 20 hours.

3. Seal the trap and heat to above 210°C. Once the necessary temperature is reached, transfer the gas, using helium as the carrier gas to improve efficiency, into the radon detector for measurement.

The resultant measurement of gas activity is shown in Figure 7.6.

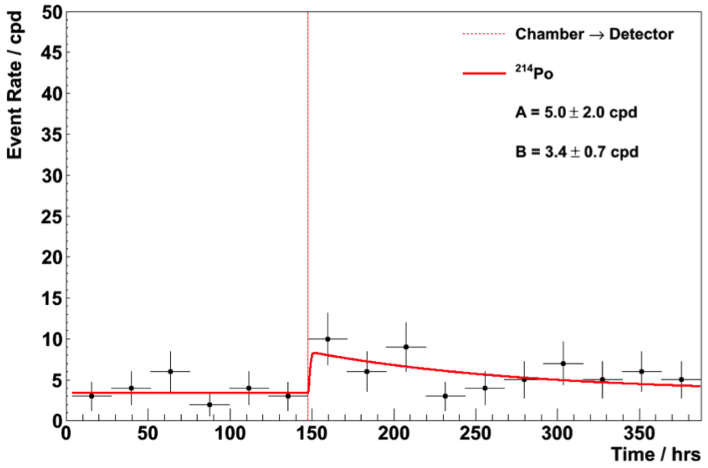

Figure 7.6: Result from the measurement of the radon content in zero grade cylindered nitrogen.

Using the trapping and transfer efficiencies from the flow-through calibration shown previously, the specific activity of the nitrogen gas, a_G can be extracted as 20 ± 13 μBq/m^3. This can be compared to previous measurements of cylindered and boil-off gas as shown in Table 7.1.

Gas	Source	Radon Level (µBq/m^3)
He	Cylinder	70-100
N_2	Cylinder	400-1000
N_2	Boil-off	90-140
N_2	GPS	20

Table 7.1: Radon activity measured from various carrier gas and containers.

Comparing the radon activity of cylindered nitrogen before and after it passes through the GPS, a suppression factor of $>$20 can be conservatively estimated which is in agreement with the predicted suppression.

7.3. Gas System Measurements

The gas system was designed and built at UCL to deliver the required gas mixture directly into the demonstrator. Since the gas mixture contains 4% ethanol, any radon emanated by the gas system cannot be filtered using a carbon trap, therefore, this radon contributes directly to the demonstrator radon budget. Hence it was essential to test it for radon emanation. Three different tests were devised to measure the radon emanation of the gas system; a flow-through measurement, a spike measurement and finally a RnCL measurement.

The gas system has already been used for commissioning the completed quarter trackers using the operational gas mixture. The high content of ethanol present would contaminate the RnCL carbon trap by significantly reducing its trapping efficiency. Even a few 100 ppm of ethanol can cause the detection efficiency to halve, rendering any measurement useless [83]. Even if it was possible to calibrate the trap for the reduction in trapping efficiency as a function of ethanol, the small carbon trap would be quickly saturated by the ethanol which would severely reduce the volume of gas measurable which is directly related to the sensitivity achievable. The ethanol would also cause deionisation of the radon decay daughters hence affecting the detection efficiency of the electrostatic radon detector.

7.3.1. Ethanol Removal

It was decided the best way to disentangle the radon emanation from the gas system would be to drain the ethanol completely. This would essentially turn the gas system into a similar setup as the radon emanation chamber described above.

Although it is possible to quickly drain the main chamber of ethanol, for the RnCL measurement, the level of ethanol within the output gas has to be at a level below 10 ppm. A residual gas analyser was acquired to monitor the content of the gas system exhaust before and after it was drained of ethanol. The ambient cleanroom air was measured along with the ethanol content set to 1-4% to calibrate the residual gas analyser.

After the main chamber was drained, 150 m^3 of standard grade cylindered nitrogen was flushed through the gas system at a flow rate of 10 lpm and the exhaust was continually monitored to track the reduction in ethanol levels. After 10 days of flushing, the ethanol levels in the gas stabilised at 6 ppm. This level was higher than expected and likely due to the fact that standard grade cylindered nitrogen contains trace amounts of impurities which could contribute to the observed levels of ethanol.

To establish if this was indeed the cause, the gas system was flushed with a higher purity nitrogen which has known levels of contamination, 2000 ppm of oxygen, CO, CO_2, hydrocarbons, hydrogen and water. The levels of observed ethanol did drop to 5 ppm but once again plateaued.

A third flushing attempt was performed using a cleaner, higher purity helium containing 700 ppm of O, 200 ppm of water, 100 ppm of CO, CO_2, hydrocarbons and hydrogen. The ethanol content again dropped and stabilised at 4 ppm, the remaining observed ethanol was likely as a result of the impurities from the gas itself instead of contribution from the gas system.

7.3.2. Flow-Through Measurement

The flow-through measurement requires the carrier gas to pass directly through the electrostatic radon detector which is in situ taking data. The gas system was setup to flow at 4.2 lpm instead of the nominal 14 lpm to increase the sensitivity of this measurement.

The gas system was purged using zero-grade nitrogen 24 hours prior to the start of the measurement. The nitrogen was then replaced with zero-grade helium which improves detection efficiency of the detector. The helium was flowed through the gas system, the electrostatic detector and finally to exhaust. This was carried out over 3 days and the resultant plots are shown in Figure 7.7.

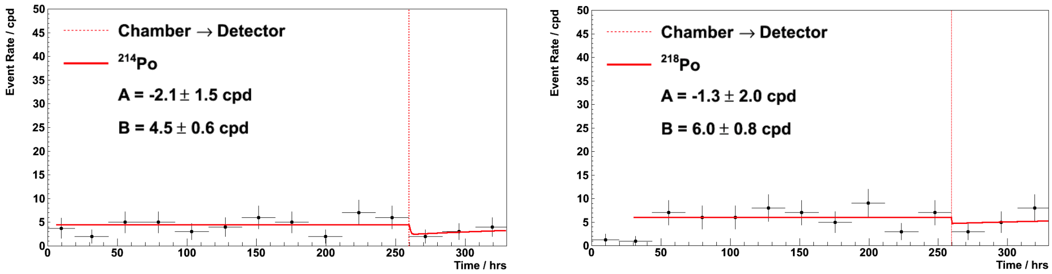

(a) ^{214}Po Rate. **(b)** ^{218}Po Rate.

Figure 7.7: Activity from the flow-through measurement of the gas system.

To extract a limit from this measurement the suppression factor due to the gas flow must first be taken into account. This can be calculated as;

$$A_D = \frac{A_0}{1 + \frac{\phi}{\lambda V}} + A_B \tag{7.3}$$

where

- A_D is the detected activity
- A_0 is the true activity
- A_B is the intrinsic detector background activity
- ϕ is the flowrate
- λ is the decay constant for radon
- V is the volume (combining the gas system, 50 litres, and the radon detector, 70 litres)

From a flow rate, ϕ, of 4.2 lpm and a volume, V, of 120 litres a suppression factor of 280 can be calculated. Taking this into account and using the uncertainty on the activity detected, A, a limit can be set at < 25 mBq at 90% CL. This confirms there is no major radon emission inside the gas system. This measurement also further purged the pipework of any residual ethanol.

7.3.3. Spike Measurement

The setup for this measurement is similar to that of a radon emanation chamber measurement. The gas system is treated as essentially a large emanation chamber. Due to its volume, the gas cannot be transferred in its entirety to the radon detector for measurement without creating a large overpressure inside the electrostatic detector. Such overpressure can affect the detection efficiency as well as putting pressure on the detector seals, the detector is not certified above 2 bar.

To begin, the gas system was purged using zero-grade helium which had been further purified using the GPS. The system was then sealed to allow for emanation at atmospheric pressure. After the emanation period, and immediately prior to gas transfer, the gas lines before and after the sealed system were flushed in order remove any possible background contribution.

The transfer was done by flowing 25 litres of helium into the gas system which displaces 25 litres of gas into the electrostatic detector for measurement. There is some uncertainty regarding the transfer efficiency and a conservative estimate of 35% was used presuming 50% of the gas is transferred from the gas system with a transfer efficiency of 70% as previously measured [84]. The detector is sealed and the results are shown in Figure 7.8, which corresponds to an activity of 1.97 ± 0.31 mBq, based on the ^{214}Po result. The observed difference in activity of ^{214}Po and ^{218}Po could be due to trace levels of ethanol affecting the detection efficiency, even for ethanol at levels of less than 10 ppm.

7.3.4. RnCL Measurement

The setup for this measurement is similar to the measurement of the gas cylinders (Section 7.1.2) but requires the gas system to be purged continuously for 50 hours prior to starting the trapping. This ensures the radon level inside the gas system reaches an equilibrium state. After purging, the gas is flowed at a constant rate

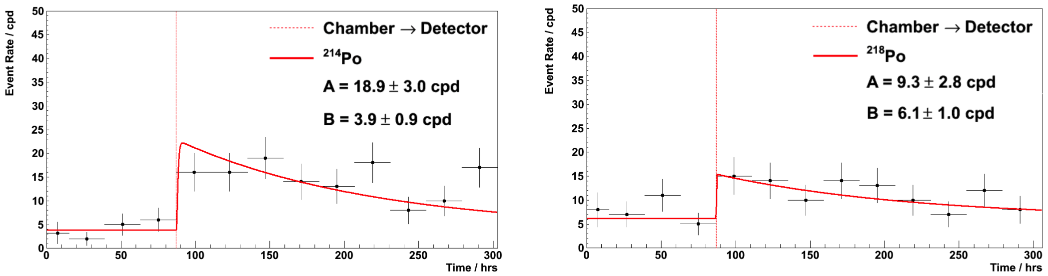

(a) ^{214}Po Rate. (b) ^{218}Po Rate.

Figure 7.8: Activity from the spike measurement of the gas system.

through the RnCL carbon trap which has been cooled to -35°C. After 20 hours of trapping, a total gas volume of 10 m^3 was sampled. The carbon trap is then sealed and heated to 210°C before the gas is transferred from the trap into the detector using 25 litres of helium.

The detector is sealed and the results are shown in Figure 7.9.

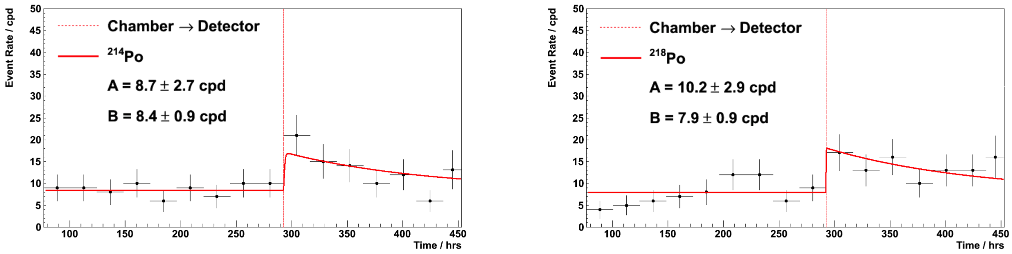

(a) ^{214}Po Rate. (b) ^{218}Po Rate.

Figure 7.9: Activity from the RnCL measurement of the gas system.

Using Equation (7.2) an activity of 1.21 ± 0.38 mBq was found.

7.4. Tracker Measurements

The RnCL has been shown to be able to measure a supply of gas, of uniform activity, at a sensitivity below the SuperNEMO radon requirement. This is important since the main quantity the RnCL must be able to verify was the SuperNEMO tracker had achieved a radon emanation level < 0.15 mBq/m^3. The tracker for the demonstrator module is composed of four segments each in the shape of a C, hence frequently referred to as C-Sections (see Figure 7.10). Each individual tracker section is constructed at MSSL where it must then be sealed and tested for radon emanation before being transported to the LSM for assembly. In total each quarter tracker is composed of a stainless steel frame, 32 x-wall and 16 veto PMTs. There are 504 octagonal drift cells inserted as cassettes of 18 cells at a time.

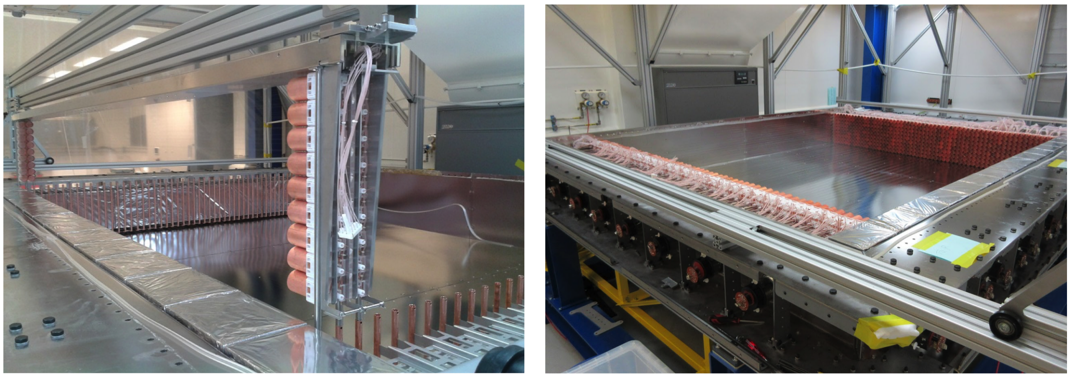

(a) Single cassette installation. **(b)** Complete quarter tracker.

Figure 7.10: Quarter tracker construction inside the MSSL cleanroom.

The first two C-Sections were measured, before the tracking cells were inserted, half way through cell insertion and, finally, measured again after construction was complete. This provided the necessary information to disentangle any source of radon emanation so it might be pin pointed and removed.

Prior to full Demonstrator assembly, the C-Section must be sealed without the calorimeter walls to enable radon testing and commissioning of the tracker cells. Customised gas-sealing plates were designed, which are fixed in place of the calorimeter wall, source foil and the point at which two C-Sections join together.

7.4.1. Measurement Starting Point

In an ideal scenario the C-section would be left perfectly sealed for an extended period prior to the measurement in order to allow for the radon to build up. However, in reality, a C-section is not a sealed unit as it has small leaks. These leaks means that it must retain a constant small overpressure to prevent environmental radon diffusing inside. The number of radon atoms inside a C-section, N_T can be modelled by:

$$\frac{dN_T}{dt} = A_T + A_G - \lambda N_T - \frac{f_{in} N_T}{V_T} + \frac{f_{in} a_G}{\lambda} \tag{7.4}$$

where A_T and A_G are the intrinsic activity of the C-Section and gas supply line respectively, f_{in} is the input flow rate of gas, $V_T = 3.8$ m^3 is the volume of one C-section and a_G is the activity of gas per unit volume.

Since the C-Section was exposed to the cleanroom air prior to being sealed and the seal is not perfect it is expected some residual radon from the atmosphere is housed inside detector components, as indicated from the radon harbouring hypothesis, shown in Section 6.3.2. Therefore, after the C-Section is sealed it must be kept under a constant overpressure by actively purging with cylindered nitrogen at 3 lpm, creating an overpressure of 2 mBar inside the tracker for 18 days before a measurement can be carried out.

7.4.2. The Anti Radon Tent

To isolate each tracker module from the environment, whilst the C-Section is kept under constant gas-flow, an anti radon tent was devised which will surround the C-Section and be purged constantly with pure nitrogen. Several designs for the tent were trialled, with the final design being made from large double layered polyethylene sheets heat sealed together. The tent is then draped over each C-Section and sealed securely to the floor. Four flushing points were fitted to the tent, equally spaced apart, and purged at a rate of 3.6 m^3/hr. A clear overpressure is established within the tent as can be seen by the clear bulge of the tent both above and around the C-Section, as shown in Figure 7.11.

A commercial radon detector (RAD7 [85]) was used to confirm and monitor the reduced radon levels inside the tent at all times during a C-Section measurement. The radon levels of the cleanroom was monitored closely and varies from $2-3$ Bq/m^3 to $20-30$ Bq/m^3. This compared to the radon level measured inside the anti radon tent of ~ 0.1 Bq/m^3 (Figure 7.12): a reduction of more than 2 orders of magnitude. Since the tent is purged with cylindered nitrogen there was also a visible reduction in the humidity levels inside the tent as shown in Figure 7.12b. The tent was used for each C-Section radon emanation measurement.

Figure 7.11: Photograph of the anti-radon tent covering the C-section.

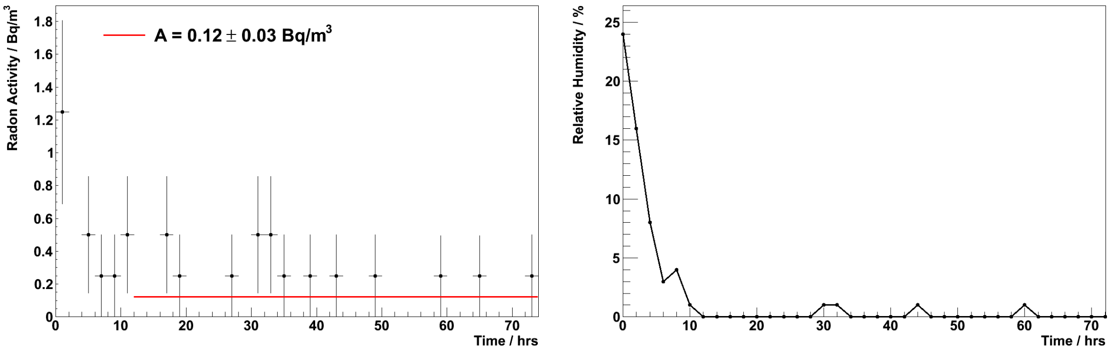

(a) Radon Activity **(b)** Humidity

Figure 7.12: Measurements made by the RAD7 device inside the anti-radon tent during a C-section measurement. Radon activity and humidity measurements are shown.

7.4.3. Measurement Procedure

For the C-Section measurement, the RnCL was connected to the C-Section as shown in the schematic in Figure 7.13. The connections were made using 6 mm wide and 2 mm thick nylon pipes which were tested for radon emanation and showed no excess contribution. Due to the low overpressure inside the C-Section, a diaphragm pump was attached at the exhaust of the RnCL in order to achieve sufficient flow rate for the measurement.

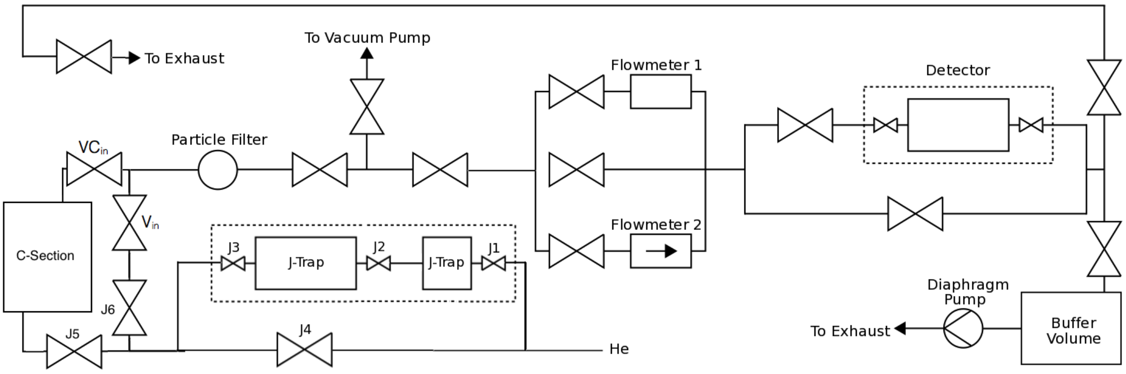

Figure 7.13: System setup for a C-Section measurement.

Before the start of a measurement, the flushing rate into the C-Section is increased from the purging rate of 3 lpm to 14 lpm. This flow rate was chosen to maximise gas flow through the RnCL whilst maintaining a healthy overpressure inside the tracker module. The output activity of the gas from the tracker can be modelled as:

$$A(t) = \frac{A_T + A_G + f_{in} a_G/\lambda}{\lambda'_T/\lambda}\left(1 - e^{-\lambda'_T t}\right) + A_0 e^{-\lambda'_T t} \tag{7.5}$$

where A_0 is the measured activity and

$$\lambda'_T = \lambda + \frac{f_{in}}{V_T}\,. \tag{7.6}$$

It can be seen from Figure 7.14 that after 50 hours the output activity reaches an equilibrium even with high intrinsic activities. Therefore, each C-Section was flushed at 14 lpm 50 hours prior to the start of a measurement with 7 lpm going through the RnCL and the rest exhausted through leaks.

After 50 hours the trap on the RnCL is heated to clear it of any residual radon, setting time zero of t_C. Once the trap is cleared it is sealed under atmospheric pressure and cooled to -35°C. Once the trap is cooled, the nitrogen from the C-Section is diverted through the trap, at 7 lpm, and out to the exhaust. After 20 hours the trap is again sealed under atmospheric pressure and allowed to warm. Finally, the trap is heated to 220°C before the gas inside is transferred into the radon detector for measurement.

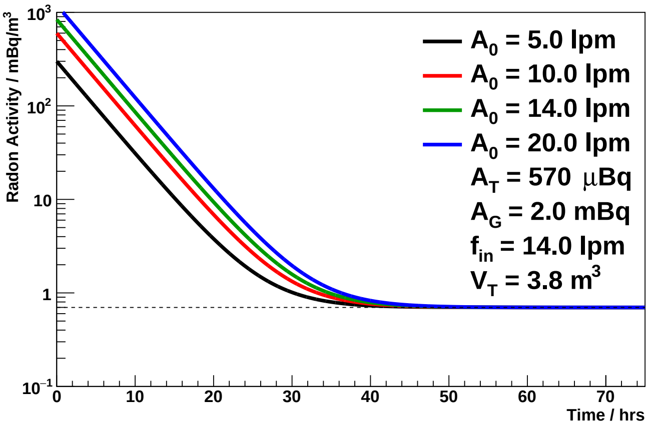

Figure 7.14: Activity inside the C-section whilst flushing prior to a radon measurement, as modelled by Equation (7.5).

7.4.4. C-section Activity Calculation

Since each C-Section is not perfectly sealed and radon is lost through the leaks modelling is required to extract the intrinsic radon activity of the C-section from background components. Before starting any measurement the C-section is flushed at ~ 14 lpm for 50 hr. At this point, the equilibrium activity, a_T^{eq}, inside the C-section is given by:

$$a_T^{eq} = \frac{A_T + A_G + f_{in} a_G/\lambda}{V_T + f_{in}/\lambda}\,. \tag{7.7}$$

The activity, A_T, of the C-Section can be extracted by rearranging Equation (7.7) to give:

$$A_T = \left(1 + \frac{f_{in}}{\lambda V_T}\right) V_T a_T^{eq} - A_G - \frac{f_{in} a_G}{\lambda}\,. \tag{7.8}$$

7.4.5. Background Measurement

In order to better estimate the background radon contribution during a C-Section measurement a "blank" measurement was carried out. This measurement has the same setup as the gas cylinder measurement but with the addition of 60 meters of gas line used during the C-Section radon measurements. A total volume of 6.73 m^3

was used producing a result of:

$$a_G^{used} = 0.044 \pm 0.015 \text{ mBq/m}^3\,. \tag{7.9}$$

The cylinders used were only half full compared to the start of C-Section measurements with a starting pressure of 90 bar instead of 180 bars, as used during C-Section measurements. Therefore, the specific activity of the gas with a full cylinder can be estimated using:

$$A(T_2) = \left(1 - e^{-\lambda(T_2 - T_1)} + \frac{V(T_1)}{V(0)} e^{-\lambda(T_2 - T_1)}\right) A_B\,. \tag{7.10}$$

The resulting specific activity of the nitrogen was:

$$a_G = 23 \pm 8 \text{ µBq/m}^3 \tag{7.11}$$

This result is in good agreement with the previously measured gas activity after passing through the GPS.

7.4.6. C-Section Measurement Results

The results from the measurements of each C-Section are presented here. For each test the setup was identical with the C-Section enclosed by the gas sealing plates and then tested for gas tightness. The sealed C-Section is then enclosed within the anti radon tent where it is purged continuously for 18 days prior to a measurement.

First Quarter Tracker

The result from the measurement of the first fully populated C-Section, C0, is shown in Figure 7.15. From this result, a_T^{eq} was calculated to be 0.118 ± 0.018 mBq/m^3 which translates to a C-Section activity (A_T) and specific activity (a_T) of:

$$A_T = 11.37 \pm 1.44 \text{ mBq}, \qquad a_T = 2.99 \pm 0.38 \text{ mBq/m}^3\,. \tag{7.12}$$

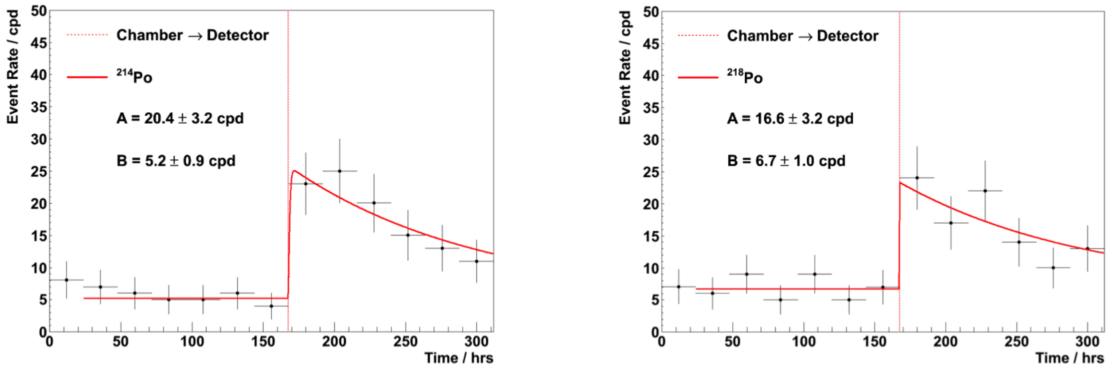

(a) Activity of ^{214}Po **(b)** Activity of ^{218}Po

Figure 7.15: Result from the RnCL measurement of C0.

Second Quarter Tracker

The result from the measurement of the fully populated C1, is shown in Figure 7.15. From this result, a_T^{eq} was calculated to be 0.152 $^{+0.019}_{-0.034}$ mBq/m^3 which translates to a specific activity of:

$$A_T = 15.26^{+2.50}_{-3.82} \text{ mBq}, \qquad a_T = 4.02^{+0.66}_{-1.01} \text{ mBq/m}^3 \tag{7.13}$$

The uncertainties associated with these results are asymmetrical due to a period of background instability, in which the background was observed to fluctuate to a higher baseline, after a period of 5 days or more. However, the detector background stabilised to its original lower level after a period of few months.

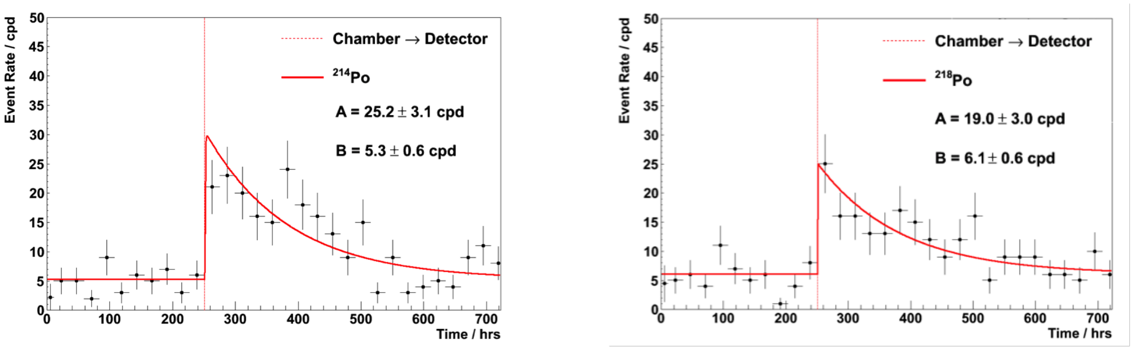

(a) Activity of ^{214}Po **(b)** Activity of ^{218}Po

Figure 7.16: Result from the RnCL measurement of C1.

Third Quarter Tracker

During the construction of C0 and C1, radon emanation measurements of the geiger cell carriers showed a positive contribution to the tracker gas. This component was replaced for the construction of C2. From emanation results the contaminated component was estimated to contribute an activity of 4 ± 1 mBq per C-Section.

The result from the measurement of the fully populated C2, is shown in Figure 7.15. As expected the radon level for C2 was reduced. From this result, a_T^{eq} was calculated to be 0.057 ± 0.017 mBq/m^3 which translates to a specific activity of:

$$A_T = 4.36 \pm 1.31 \text{ mBq}, \qquad a_T = 1.15 \pm 0.34 \text{ mBq/m}^3 \tag{7.14}$$

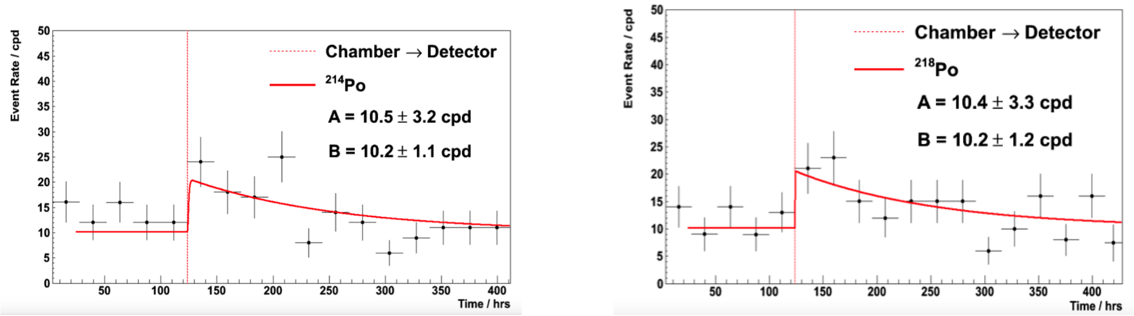

(a) Activity of ^{214}Po

(b) Activity of ^{218}Po

Figure 7.17: Result from the RnCL measurement of C2.

Summary

The results from radon emanation measurements of demonstrator construction component are shown in Table 7.2. The result from radon activity measurements of the first three C-Sections of the SuperNEMO Demonstrator are shown in Table 7.3. Taking the average radon emanation value for each of the fully populated C-Sections and extrapolating it to the final Demonstrator module would result in a specific activity of:

$$A_D = 41.0 \pm 4.6 \text{ mBq}, \qquad a_D = 2.7 \pm 0.3 \text{mBq/m}^3 \tag{7.15}$$

Sample	Activity (mBq)	Extrapolated to Demonstrator (mBq)
End-cells (1-wire, 27 pcs)	0.4 ± 0.1	13.3 ± 3.3
Cut-up Cell Carriers (0.73kg)	<0.09	<18.3
Cell Carriers (572 pcs)	<3.0	<21.3
End-cells (7+10 wire, 1042 pcs)	<2.9	<11.2
Modified End-cells (1-wire, 29 pcs)	0.16 ± 0.09	4.9 ± 2.8 (896 pcs)
Feedthrough (28 pcs)	0.31 ± 0.11	1.9 ± 0.7 (170 pcs)
Internal Cable Harnesses (1031 g, old)	<0.89	<1.9 (2.15 kg)
Internal Cable Harnesses (192 g, new)	0.46 ± 0.13	0.84 ± 0.24 (0.35 kg)
Gas System Contribution	N/A	1.97 ± 0.31

Table 7.2: Results of the radon emanation measurements of the tracker components. Limits are at 90% CL.

	C0	C1	C2
Activity (mBq)	11.37 ± 1.44	$15.26^{+2.50}_{-3.82}$	4.36 ± 1.31

Table 7.3: Summary of C-Section radon measurement results.

The total activity of measured tracker components sum to 13.8 ± 4.3 mBq or 0.9 ± 0.3 mBq/m^3 which accounts for half of the observed radon emanation of the Demonstrator. This result only considers the tracker components which produced a positive result. Since only half of the tracker is constructed with end-cells and and the remaining half with the modified end-cells, only half of the "extrapolated to Demonstrator" activity results were used for each.

These results presented above demonstrate that the stringent SuperNEMO radon requirements can be achieved by applying a flushing rate of 33.3 lpm, hence suppressing the radon activity by a factor 18.4, as shown in Figure 5.4. The resulting specific activity inside the tracker gas would be on target at 0.147 ± 0.016 mBq/m^3.

Chapter 8.

Gamma Ray Spectroscopy at Boulby Underground Laboratory

Gamma ray spectroscopy is essential for the determination of nuclear contamination. The ideal detector for gamma ray spectroscopy would have excellent;

- Detection efficiency (large Z for high absorption coefficient);
- Resolution (accurate measurement of energy deposited);
- Stability (over time, temperature, pressure etc);
- Readout (easy access to signal);
- Background (as low as possible);

The one semiconductor material which best fits all the requirements is germanium. It has a relatively high Z, suitably large crystals, can be made at reasonable costs to a very high purity and crystal perfection which is important for low background measurements. The charge carrier mobility is more than an order of magnitude better than HgI_2, CdTe and CdZnTe, in particular for holes it is more than 2 order of magnitude higher. It has good energy resolution, as germanium produces a high number of electron-hole pairs per unit energy deposited;

$$n = \frac{E_{abs}}{\varepsilon} \tag{8.1}$$

where n is the number of electron-hole pairs produced, E_{abs} is the absorbed gamma energy and ε is the average energy needed for electron-hole pair creation. Germanium has one of the lowest ε of all the semiconductor materials. The only disadvantage of germanium is the low band gap. Hence, germanium detectors must be cooled in order to reduce thermal generation of charge carriers, otherwise the energy resolution is washed out by leakage-current induced noise.

A new low background germanium facility has been established at the Boulby Underground Laboratory, located in the North East of England. It is located within a working potash and rock salt mine, the deepest in the UK at 1070 metres (2805 m w.e.) below ground [86]. The air inside the laboratory has a naturally low level of radon content due to the low levels of uranium and thorium in the surrounding salt tunnel. At the start of this PhD project, a single germanium detector was resurrected for material screening purposes. Since then the single detector has been completely refurbished, replacing all components except for the high purity germanium crystal. Three more new low background germanium detectors have been installed with customised shielding constructed for each detector. The four detectors are now housed in a dedicated gamma-ray spectroscopy suite, which is maintained as a class 1000 cleanroom. Several other detectors are planned to be located at Boulby over the next year, establishing Boulby as a world class low-background germanium measurement facility.

8.1. Germanium Detectors

Germanium detectors are semiconductor diodes with a p-i-n structure in which the intrinsic (i) region is sensitive to ionisation radiation, particularly x-rays and gamma rays. Germanium doped with five valent impurities will have one excess electron at the impurity lattice site. Such impurities are known as donor impurities and will introduce donor states just below the conduction band, such germanium is called n-type germanium (‘n’ for negative donor impurities). Therefore, germanium doped with three valent impurities have one too few electron. Such impurities are known as acceptor impurities which introduce acceptor states just above the valence band. Germanium doped with such impurities is called p-type germanium (‘p’ for positive acceptor impurities).

High purity germanium (HPGe) detectors are typically constructed using a block of high purity p-type germanium with an n+ layer on one face, shown in Figure 8.1. When a reverse bias is applied to the detector, a depletion layer is then created throughout the p-type material. The interaction of gamma-rays with the material inside the depleted volume creates charge carriers (electrons and holes) which migrate to the p and n electrodes as a result of the electric field.

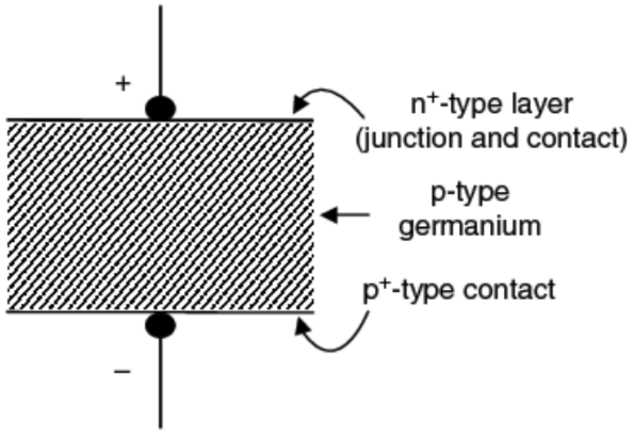

Figure 8.1: The layout of a p-type germanium detector.

8.1.1. Types of Germanium detectors

There are a number of different configurations of germanium detectors optimised for different applications. The standard geometries and their detection efficiencies over the energy range 0-1000 keV are shown in Figure 8.2. The detection efficiency curves shown are only indicative; the actual efficiency depends on the exact geometry of the Ge crystal and the sample used for the measurement.

At low energies the efficiency is limited due to the absorption of gamma-rays by various detector components before they reach the Ge crystal. At high energies, the efficiency is limited by the Ge crystal size and the drop in absorption coefficient as energies increase. Leading Ge detectors with large crystals are capable of detecting gamma-ray energies of up to 10 MeV.

The four germanium detectors which have been commissioned at Boulby include; a coaxial detector (Lunehead) for large samples, a well detector (Lumpsey) optimised to produce high detection efficiency for small samples, a BEGe detector (Chaloner) for

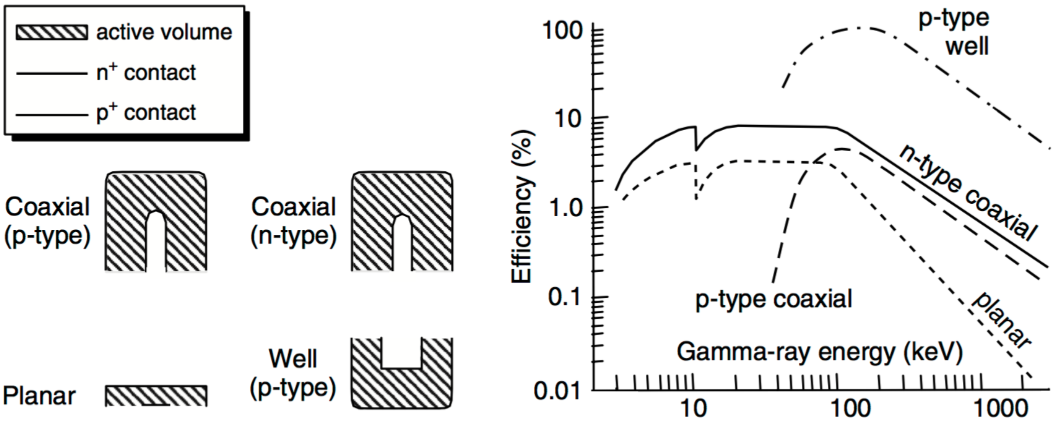

Figure 8.2: The 4 standard HPGe detector configurations and an indication of efficiency for each geometry [87].

detection of low energy gammas and a pre-screening BEGe (Wilton) for highlighting samples with a high radiation content. Together the four complimentary detectors are able to measure a diverse range of samples.

8.1.2. Detector schematic

Typical HPGe detectors are very sensitive to any external gamma-rays and need to be shielded in order to achieve suitable background levels for low activity material measurements, such a shield is also called a castle. Ideally the shielding would be made of a material of high atomic number and low intrinsic activity. There are many factors to consider when building a castle to house HPGe detectors:

- Lead is usually the most popular choice of shielding against external gammas. For general purposes 50 mm of lead wall on all sides should be sufficient, ideally using interlocking bricks to prevent any gaps which can offer a line of sight for gammas. There are many different grades of lead which have varying levels of radioactivity. Fresh mined lead is usually more radioactive because although uranium and thorium are removed in the processing of lead, ^{210}Pb with its high half-life, 22.2 years, remains which undergoes low energy beta decays. Certified low activity lead, <50 Bq/kg, can be purchased at increased cost and archeological lead from sunken roman ships offer lead of even greater radio-purity, as the water shields the lead from cosmic rays and man-made isotopes.

- Oxygen-free, high conductivity (OFHC) copper is often used as the core shielding, as the process to remove oxygen also eliminates other radioactive contaminates. However, it is expensive and has a high cross section for thermal neutron capture and for the cosmogenic production of radioactive nuclei.
- Cadmium was also used as an internal shielding specifically for neutrons, however due to its extremely high toxicity it is no longer used.
- Steel can be used, however it can contain high levels of ^{60}Co.
- Aluminium is sometimes used as internal lining, however it usually contains uranium and thorium, so should not be used for extremely low background detections.
- Mercury would also make excellent shielding as it can be readily purified via distillation. However, it is expensive, difficult to contain and shares the similar issue of toxicity as cadmium.

There is no single perfect design for HPGe shielding, it depends on background requirements and costs. A standard configuration usually involves 50 - 100 mm of lead followed by 20 - 100 mm of copper all surrounded by an anti-radon tent, as shown in Figure 8.3. The copper is essential to remove low energy gammas and fluorescent x-rays in the background spectra. If using roman lead or a combination of cheap lead with a inner lining of roman lead then less copper is required.

The detector shielding should also be configured to allow for a large sample capacity. Keeping a large distance between the end cap and the castle wall to create the large capacity also has the added benefit of minimising the effects of backscattering which can contribute to the background spectra. The detector end cap is usually made of either magnesium or carbon fibre 0.9-1 mm in thickness and extremely radio-pure.

The Boulby detector castles were designed with 100 mm of lead, selected through screening to have the lowest ^{210}Pb content and has been underground for more than 20 years. Inside the lead shielding is 100 mm of high-purity copper which is used to reduce the remaining ^{210}Pb gammas, ^{210}Bi bremsstrahlung as well as the fluorescent X-rays from the lead. In order to remove electronic noise, the detector and the

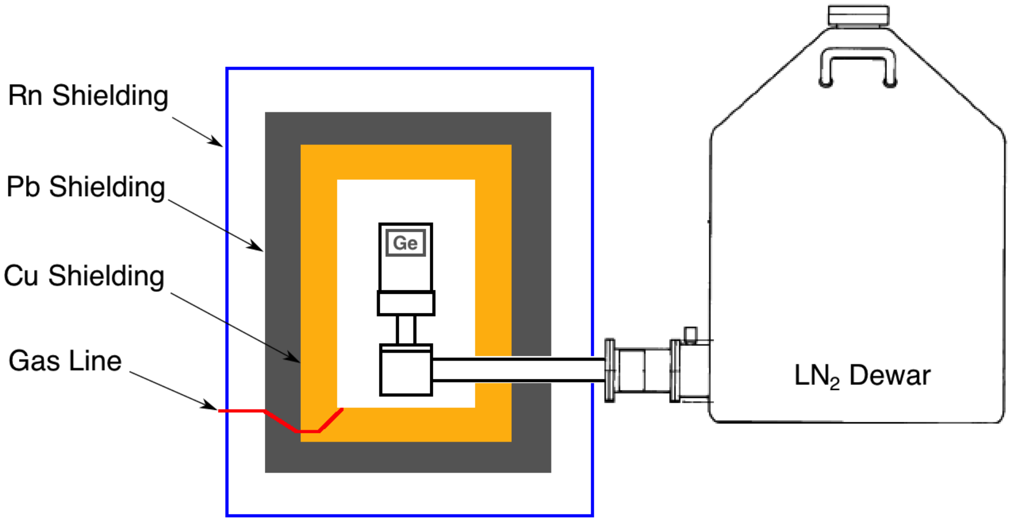

Figure 8.3: Typical HPGe detector schematic, the crystal is mounted inside a vacuum endcap and cooled using a cold finger which is in thermal contact with a liquid nitrogen dewar.

cryostat were kept electrically isolated from the shielding by inserting insulation around the stem of the detector. For radio-purity purposes the preamplifier is also placed outside the detector shielding.

The copper layer was cleaned using diluted acidic solution to remove any residual surface contamination then wiped down using deionised water before installation. The surface contaminates which were removed include residual ^{210}Pb from radon decay daughters which plate out on exposed surfaces. Also, as Boulby is located inside an active salt mine, there was a significant level of contamination from dust brought into the lab which contains ^{40}K, ^{238}U and ^{232}Th. The lead was cleaned using an alkaline solution to again remove dust contaminations on the surface and was then wiped down using IPA before reassembly.

8.2. Detector Calibration

There are three main calibrations required in order to interpret the gamma-ray spectra obtained by the HPGe detectors in terms of measured activity;

- Energy calibration - to convert from ADC to energy;

- Resolution calibration - to determine the variation of peak width as a function of energy;
- Efficiency calibration - the ratio of counts observed to the number of decays in the sample as a function of energy.

The detectors are calibrated regularly with radioactive sources such as ^{137}Cs, ^{60}Co, ^{57}Co and a Multi-Gamma Source (MGS) containing ^{65}Zn and ^{155}Eu. The MGS activity is known and is certified by Canberra to within 5% accuracy. An IAEA-385 source is also used as the main calibration source with isotope activities known to better than 5% accuracy [88]. The following calibrations are for the Lunehead detector but the procedure is the same for all four HPGe detectors.

8.2.1. Energy Calibration

The raw data is recorded using a 13 bit ADC which is used in conjunction with the amplifier and a multichannel analyser (MCA), Lynx for Canberra detectors and DSPEC for Ortec detectors, to generate a 8192 bin spectrum. This can be converted to energy by taking spectra of known gamma sources, such as ^{60}Co, which emits 1173 keV and 1332 keV gammas, and recording the peak positions in ADC units. Then a plot of the true energy against the mean energy peaks in ADC can be made as shown in Figure 8.4.

8.2.2. Resolution Calibration

The resolution of the detector at a particular peak energy is define by applying a gaussian fit to the peak energy region. The $\pm 3\sigma$ region is then used to determine the number of counts at a peak, i.e. for particular isotope. The width of peaks at the various energies were measured and the ratio of the σ to the mean energy of the gamma peak and can be plotted as shown in Figure 8.5.

8.2.3. Efficiency Calibration

In this case, efficiency refers to the detection efficiency, ε, of a particular gamma line which is defined as the ratio between the number of counts detected in a peak to the

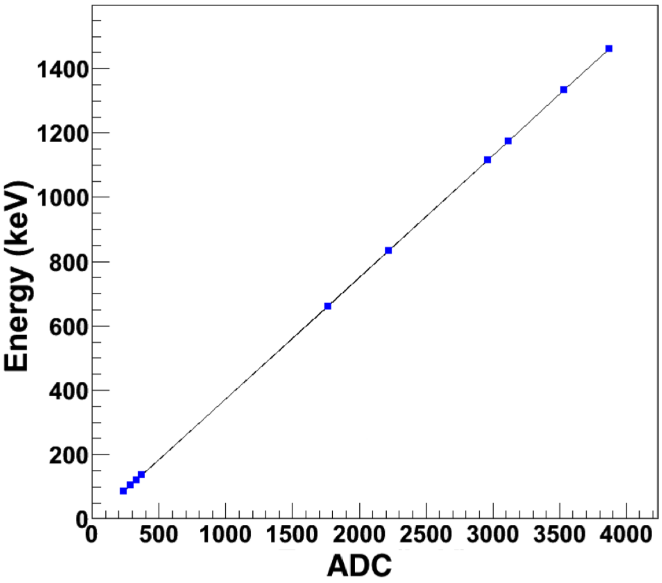

Figure 8.4: Energy calibration using ^{137}Cs, ^{60}Co, ^{57}Co and the MGS fitted to obtain the energy to ADC conversion for the Lunehead detector.

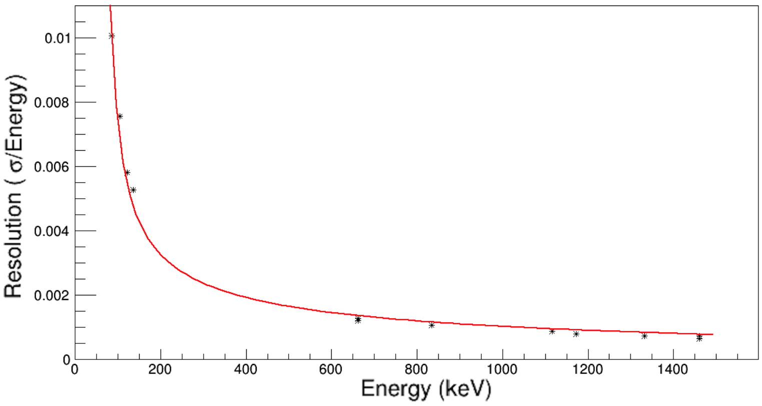

Figure 8.5: The detector energy resolution plotted as a function of the mean energy. The red line shows the fit of the data points which is then used to estimate resolution at any given energy.

number of gamma of that energy emitted by the source. It is calculated from Monte Carlo (MC) simulations using GEANT4 [89]. To verify the detection efficiency, the MC, simulated efficiency was compared to a measured detection efficiency of certified calibration sources with known number of gamma ray emissions and energies.

To ensure the MC was reliable, a detailed description of the internal schematic of the magnesium endcap including cooling pin and their exact composition was obtained from the detector manufacturer. This was then added into the simulations. The shape, position and geometry of the calibration samples were measured and simulated using GEANT4 to improve accuracy of simulation. The IAEA calibration sample is uniformly distributed inside the petri dish as shown in Figure 8.6.

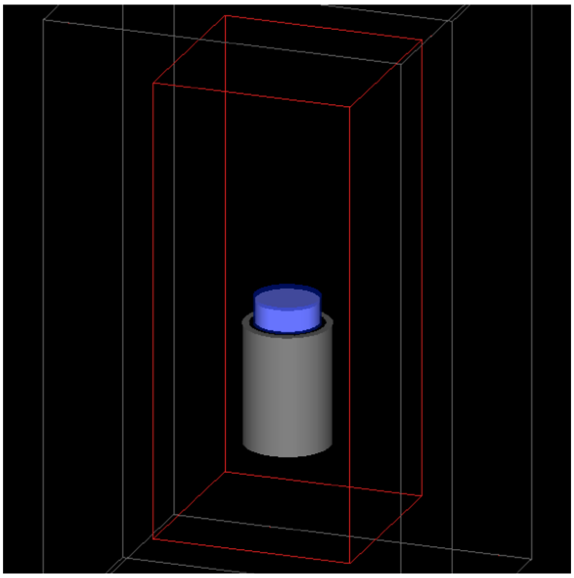

Figure 8.6: Simulated IAEA on detector endcap for MC of detection efficiency.

The measured activity of the calibration sample is compared to the certified value by IAEA and the resulting ratio is shown in Figure 8.7. Although the agreement at higher energies for the MC is not within 10% to the IAEA sample, the same IAEA sample was measured at several other detector facilities and there is agreement to less than 10% between the cross calibrations. This result suggests there is some inaccuracies to the certified values of the IAEA sample. The detector also took part in cross calibration programmes of a standard candle and the results are within 10% of the measured average [90].

The simulated efficiency as a function of energy is shown in Figure 8.8 for a hypothetical point source placed 5mm above the detector.

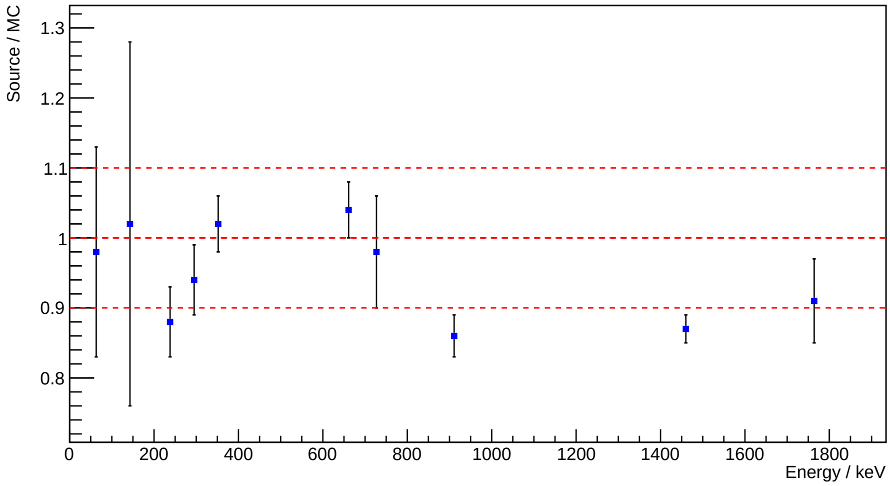

Figure 8.7: Comparison of measured source activity to MC results.

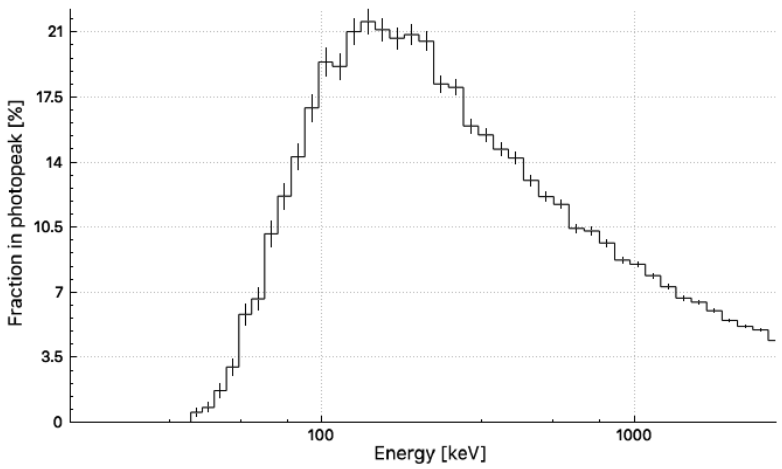

Figure 8.8: The simulated detector efficiency for a point source placed directly above the detector.

The reference data for gamma ray energies, the branching ratio of each decay process and the nuclide half-life used for generating the MC were sourced from the National Nuclear Data Center [77]. The MC for each sample measurement must be tailor made as it is heavily dependent on the sample geometry and location relative to the detector.

The achievable sensitivity depends on the inherent background in the detection volume and the detection efficiency of the measured sample. The detection efficiency of a source can be maximised using MC simulation to determine the optimum sample geometry. Hence, each sample can be optimised for measurement.

8.3. Minimum Detectable Activity

The MDA is the minimum amount of radioactive nuclide which can be confidently detected, at a given confidence interval, of a specific measured spectrum. The method used to find the MDA of a germanium detector is the same as was outlined in Section A.1.

Using this relationship the MDA of each HPGe detector to ^{238}U and ^{232}Th as a function of time was calculated using the ^{214}Bi and ^{212}Pb lines respectively, the results are shown in Figure 8.9. The detection efficiency used to estimate the sensitivity was taken from a GEANT4 simulation result of a 100 g IAEA-385 calibration source placed directly at the centre of the detector end cap.

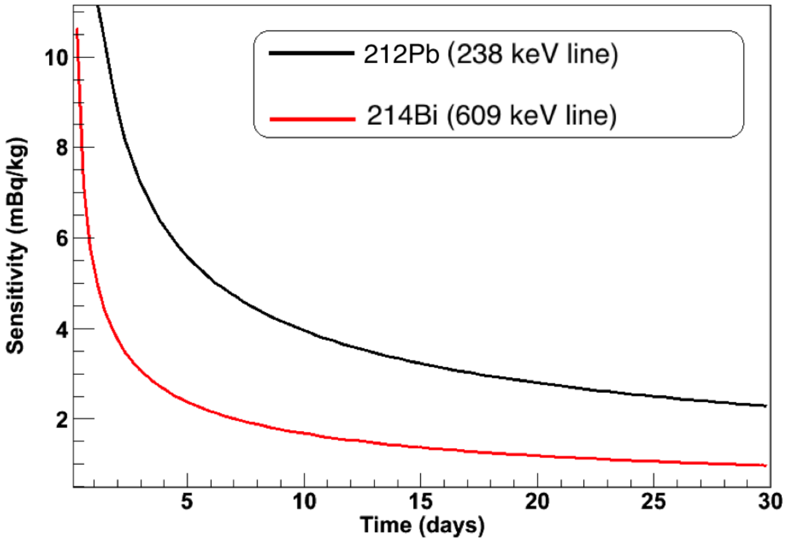

Figure 8.9: Sensitivity for ^{238}U and ^{232}Th using the ^{214}Bi and ^{212}Pb lines respectively

8.4. Analysis method

For SuperNEMO, there are 13 gamma energies of interest, mainly as a result of the ^{238}U/^{232}Th decay chains and in particular ^{214}Bi and ^{208}Tl which form the main background to the SuperNEMO detector as summarised in Table 8.1.

Decay Isotope	Energy (keV)	Chain/Nuclide	Branching Ratio
^{238}U	63	^{234}Th→^{234}Pa	0.037
	92	^{234}Th→^{234}Pa	0.042
	295	^{214}Pb→^{214}Bi	0.184
	352	^{214}Pb→^{214}Bi	0.356
	609	^{214}Bi→^{214}Po	0.455
^{235}U	186	^{235}U→^{231}Th	0.572
^{232}Th	238	^{212}Pb→^{212}Bi	0.436
	338	^{228}Ac→^{228}Th	0.113
	911	^{228}Ac→^{228}Th	0.258
^{137}Cs	662	^{137}Cs→^{137}Ba	0.851
^{60}Co	1173	^{60}Co→^{60}Ni	0.999
	1332	^{60}Co→^{60}Ni	1
^{40}K	1461	^{40}K→^{40}Ar	0.107

Table 8.1: Energies regions of interest for use in determining U, Th and K contamination during SuperNEMO material screening

The energy spectra are saved as individual hourly files over the measurement period. This provides the ability to isolate and remove outlier files from periods of high detector noise such as during nitrogen refills. The remaining files are then combined into a single file containing the full spectra for analysis.

The spectra were analysed using ROOT [91] and the gamma peaks were fitted to gaussian with more details described in Section 8.4.2. The integrated counts in the $\pm 3\sigma$ energy region were calculated, then using ROOT, the background continuum was fitted and subtracted from the peak areas as shown in Figure 8.10. The same spectra was also analysed a second time, see Section 8.4.1, using analysis software provided by the manufacturer of the HPGe detector as a cross check.

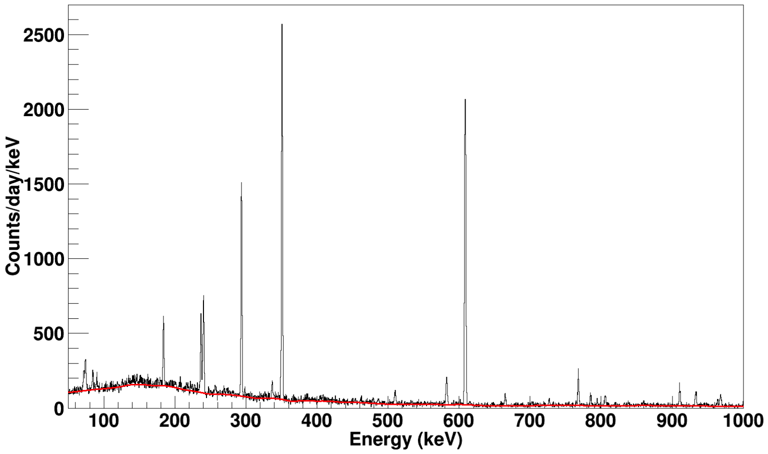

Figure 8.10: A PMT spectrum is shown to demonstrate the background continuum subtraction applied using ROOT. The spectrum is shown in black and the modelled background continuum in red.

From MC, the detector efficiency at each of the energies can be determined allowing the actual number of gammas emitted at each energy to be calculated. Then, taking into account the branching ratio, the sample's activity can be determined, usually expressed as Bq/kg. The equation is as follows:

$$A = \frac{N}{\varepsilon \cdot BR \cdot M \cdot t} \tag{8.2}$$

where A is the sample specific activity measured as Bq/kg, N is the background subtracted number of counts, ε is the detection efficiency, BR is the branching ratio, M the sample mass and t the total measurement time in seconds. The sample activity can be converted to concentrations of radioactive nuclides using the isotope mass (g/mol) and the isotope half-life.

The ^{238}U decay chain equilibrium is often broken due to long lived isotopes such as ^{226}Ra, see Figure 8.11. However, for SuperNEMO the most critical backgrounds come from isotopes after ^{226}Ra so the gamma-lines from the decay of ^{214}Pb and ^{214}Bi were used as samples to be measured. For the measurement of the contamination at the early uranium decay chain, which can also be important (i.e. neutrons from ^{238}U), the 63 and 92 keV gammas from ^{234}Th were used. For ^{232}Th the gamma-lines from ^{228}Ac, ^{212}Bi and ^{208}Tl were used.

8.4.1. Leading Industry Analysis Method

Canberra has developed software called Laboratory SOurceless Calibration Software (LabSOCS) in order to determine sample activity and contamination. It uses a MC based analysis which includes a list of fully characterised Canberra detectors which can be selected and incorporated into simulations of detection efficiency. The characterisation procedure involves determining the detector response to a point source being placed within a 500 m radius, centred around the detector in free space, over an energy range from 10 keV to 7 MeV [92]. The software allows the selection of the sample geometry based on commercially available containers as well as providing the ability to enter details of bespoke geometry designs made of materials which can be selected from a pre-defined library or constructed by the user, based on the chemical composition.

For each sample measurement the software requires; the sample geometry, composition and its location in the detector to produce an efficiency curve. The software is able then to take a measured spectrum, fit the energy peaks and subtract the background spectrum. Then taking into account the efficiency curve it is able to produce a value for the activity of the various peaks and convert this into a measurement of the radioactive contamination.

The LabSOCS software is integrated in the Genie 2000 gamma-ray spectrometry system used for spectrum capture of Canberra HPGe detectors. This allows the entire process of data capture, detector calibration, efficiency calculation and spectrum analysis to be completed using one software in a quick and fully automated way and offers a good cross check.

However, LabSOCS use is limited to characterised detectors only. Even for those characterised detectors the efficiency calculation is simulated using a parametrised response instead of GEANT4 and in free space with the sample and detector only and doesn't include a description of the detector shielding. Therefore, this detection efficiency calculation is a black box and does not take into consideration any gamma-ray interaction with materials surrounding the detector and the sample, which can result in missing backgrounds, such as backscattering and Compton scattering.

The efficiency calibration curve generated by LabSOCS also requires the user to enter the associated uncertainties. The manufacturer recommended uncertainties for standard laboratory conditions ranges from 7% at low energies (50-100 keV), 6% at medium energies (100-400 keV) and 4% at high energies (400-7000 keV). These values are significantly higher than what is achievable with standard source based calibrations, hence it cannot yet be used for very high quality measurements.

8.4.2. Automated Analysis

Motivated by the near autonomous LabSOCS, the analysis steps and codes described in the first section of this chapter were integrated into one single analysis code, detailed here. Firstly all data files are selected and the noise files, based on low energy counts, are removed. Then a energy calibration is run based on the peaks in the data. The detection efficiency must be determined separately for each measured sample using a separate GEANT4 simulation.

A file analysis script is called to sum the individual files, plot the energy spectrum and fit the pre-determined energy peaks. The background continuum is fitted using the TSpectrum class spectra processing functions as part of ROOT and subtracted. Next the background peaks in the $\pm 3\sigma$ region are fitted, using again the TSpectrum class, and subtracted from the measured spectrum, the peaks are found using the same ROOT class. The code then takes the efficiency determined by MC and the branching ratio to give the activity in Bq/kg which is then converted to a uranium, thorium and potassium contamination for each sample. The fitted plots are then written out as a PDF file, with each analysed peak saved in the format shown in Figure 8.11.

This analysis resembles the LabSOCS system, the crucial difference being an efficiency determination performed using GEANT4, taking into account the shielding effects around the detector and source, which produces a more accurate estimate of the detection efficiency. This analysis has been used for all four current Boulby detectors.

8.5. Background Measurements

Stable and repeatable low backgrounds are essential to achieving the minimum detectable activity (MDA) for a HPGe detector. The background of each detector

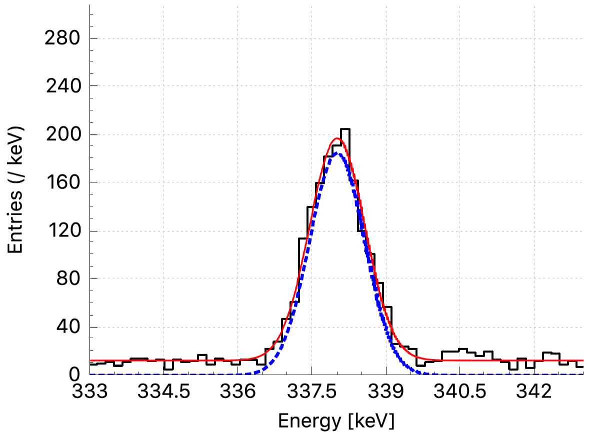

Ac-228: 338.3 keV

Fit Energy (keV)	(338.00 ± 0.02)
Fit Sigma (keV)	(0.558 ± 0.013) - (0.165%)
Chi Squared	1.609
Total Counts	(258.52 ± 16.08)
Background Counts	(1.53 ± 1.24)
Efficiency	0.0690
Branching Ratio	0.1130
Activity (Bq)	(0.37 ± 0.02)
Specific Activity (Bq/kg)	**(3.55 ± 0.22)**

Figure 8.11: The ^{214}Pb decay peak at 295 keV. The red and blue curves shows the peak fit before and after subtraction of the background continuum respectively.

was periodically measured to monitor the stability and active measures were taken to modify the detector to achieve the best possible detector MDA. After each modification to the detector and shielding, the background was remeasured to determine if any changes had occurred.

8.5.1. Radon Effects and Measurements

One of the main sources of unstable backgrounds in low-background gamma-ray spectroscopy is the presence of radon isotopes in the air which vary depending primarily on ventilation as well as other conditions such as temperature, pressure and time of the day. The radon isotopes in the air results from the emanation of trace amounts of ^{238}U and ^{232}Th producing ^{222}Rn (radon) and ^{220}Rn (thoron) respectively. Although individually neither have significant gamma-ray emissions, their decay daughters do, as summarised in Table 8.2;

There are three steps which can be taken to reduce the effects of radon isotopes inside the detector volume:

- make the detector shielding as air-tight as possible to prevent radon diffusion into the detector volume;
- reduce the volume of air inside the detector volume by filling it with sealed containers filled with radon-free air such as nitrogen or helium;

Radon Isotope	Chain/Nuclide	Energy (keV)
^{222}Rn	^{214}Pb→^{214}Bi	295
	^{214}Pb→^{214}Bi	352
	^{214}Bi→^{214}Po	609
^{220}Rn	^{212}Pb→^{212}Bi	238

Table 8.2: The daughter nuclides of radon isotopes which emit gamma-rays and their respective energies.

- flushing the central detector volume with radon-free gas such as nitrogen to actively remove the radon isotopes whilst creating an overpressure to suppress radon diffusion.

All three options would require, to some degree, a reduction in accessibility to the detector. Given the relatively long half-life of ^{222}Rn and its high diffusibility, it would be difficult to construct a seal sufficiently air tight to prevent diffusion. In particular, there is a path in the current shielding configuration for the stem of the detector to pass through into the central volume. Even if this were possible, there would still be a significant contribution of radon as a result of emanation from the Pb and Cu. Even ^{220}Rn which has a relatively short half-life of just 55 seconds, can still diffuse through the outer shielding into the central volume before decaying into daughter isotopes.

Placing sealed containers to displace the air inside the detector has been shown to result in a significant reduction in radon contributions to background measurements. However, this requires the containers to have very low radon emanation themselves as well as developing a method to fill and seal them to a satisfactory quality.

Continuous flushing offers the most practical solution in reducing radon isotopes inside the central volume. All four detector castles were designed to be as air tight as possible and to accommodate an active purging line to flush the detection volume using either cylindered or boil off nitrogen.

8.5.2. DURRIDGE RAD7 Study and Measurements

The RAD7 made by 'Durridge Radon Instrumentation' is a portable, fast radon detector with sensitivity of ∼0.1 mBq/m^3. It consists of a 0.7 litre spherical detection volume which has an electrical conductor coated on the inside surface. The centre of the volume consists of a solid-state, ion-implanted, planar, silicon alpha detector [85].

The RAD7 detector does not measure ^{222}Rn directly, instead it measures the daughter isotopes ^{218}Po, ^{214}Po and ^{210}Po. The ^{218}Po, which is positively charged, is plated onto the detector as a result of the electric field. It also detects the ^{220}Rn daughter isotopes ^{216}Po and ^{212}Po for thoron measurements. The data is recorded and can be analysed using the software CAPTURE [93]. Other than the number of polonium counts detected, the RAD7 device also records the temperature and humidity of the air it measures.

A separate analysis code was written in order to analyse the RAD7 data using ROOT independently of CAPTURE. This is in part due to the lack of clarity as to the statistical methods applied by the CAPTURE software in processing the data. This required an extensive study of the RAD7 detection efficiency to the radon decay daughters as well as the humidity correction factor.

RAD7 Intrinsic Background

The RAD7 was placed inside a sealed air tight stainless steal container which was flushed using cylindered nitrogen, at a rate of 5 lpm, in order to determine its absolute sensitivity. A fan was installed on the inside of container to ensure uniform distribution of nitrogen.

A measurement was made over an 18 hour period and the resultant radon levels are shown in Figure 8.12. The detected radon level demonstrates an intrinsic background of 0.1 Bq/m^3 for the RAD7 detector.

Radon Level Measurements

Having measured the intrinsic background of the RAD7 and tested the analysis code. The detector was brought underground to monitor and measure the radon levels

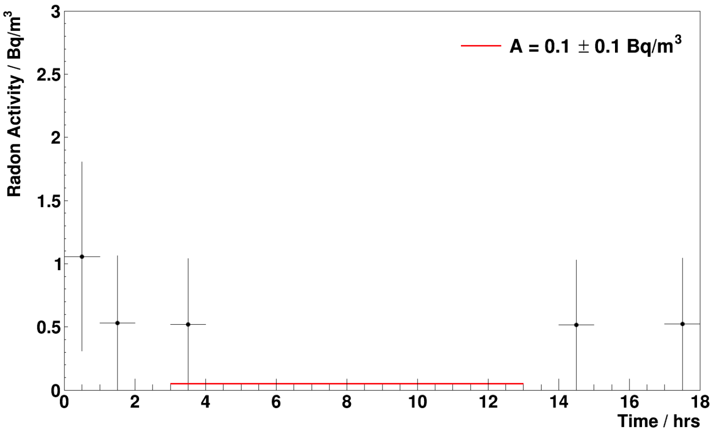

Figure 8.12: RAD7 background measurement, operating without the desiccant column, over 18 hours. Uncertainty associate with the measurement results were determined by the CAPTURE software.

inside the underground laboratory, in particular the areas around the germanium detector.

The RAD7 was setup with a desiccant drying column to reduce the humidity, and placed on a table top next to the HPGe detector. A 2 day background measurement was taken and the result is shown in Figure 8.13. There appears to be a spike in radon levels in the morning from 6 am to 11 am with unknown origin. However, analysing the data before and after the spike separately, the results are relatively consistent and agree with each other within uncertainties.

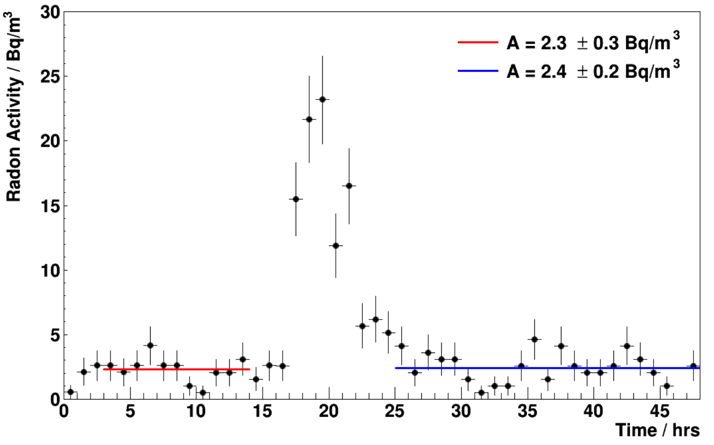

Figure 8.13: RAD7 measurement with the standard setup up over 2 days.

Following this measurement, a second measurement was made over a 10 day period giving much greater statistics. The resultant plot is shown in Figure 8.14, and the radon levels appear to be much more stable for the duration of the measurement.

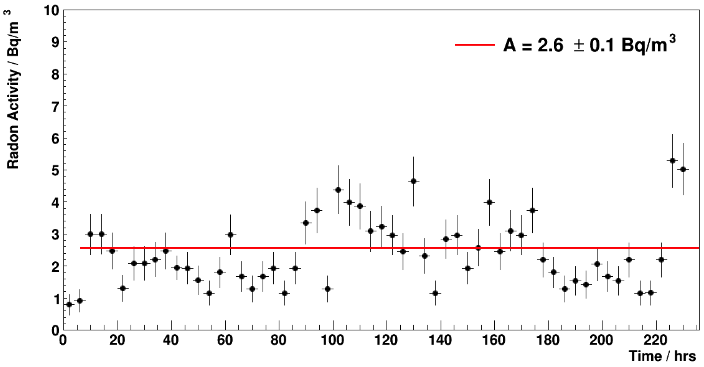

Figure 8.14: RAD7 measurement with the standard setup up over 10 days.

Combining the three data sets, taking into account the associated uncertainties, gives a radon level of 2.5±0.1 Bq/m^3 inside the laboratory.

8.5.3. Nitrogen Flushing

The customised shielding allows nitrogen to be directly flushed into the central detection volume. Cylindered nitrogen was used as the flushing gas as it has extremely low levels of radon. Since the castle is built to millimetre precision an additional anti-radon tent was not required. The detection volume is purged at a rate of 1 lpm and the excess nitrogen is allowed to leak out, creating an active flow suppressing radon diffusion. This gives much better accessibility to the detector for sample insertion and extraction.

The effectiveness of the nitrogen flushing system was tested by comparing the background spectrum before and after purging and comparing the gamma lines which resulting from the radon decays.

Nitrogen flushing at 1 lpm

Firstly, a background measurement was taken over 2 weeks with the nitrogen flushing set at 1 lpm. This rate was chosen as it is used by the LSM germanium facility for radon purging. A comparison of the resultant spectrum with the pre-flushing background spectrum is shown in Figure 8.15. This shows a reduction in the radon daughter decay peaks by a factor of 4, Table 8.3.

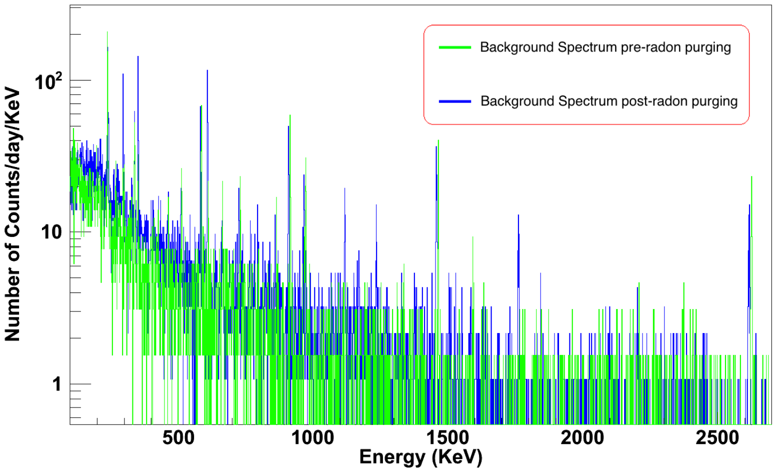

Figure 8.15: Two superimposed background spectrums taken before and after radon purging shown in green and blue respectively. The three labelled peaks are a result of radon decay isotopes.

The integrated rate between 100-2700 keV was measured to be 0.751±0.001 events/min, a reduction on the pre-radon purging rate by more than 30%. The results also show a slight reduction in the 238 keV energy peak, more than that expected from purging purely radon. This result suggests thoron was also present inside the detection volume and was also removed as part of the purging process, which could explain why only the 238 keV peak was reduced and not the 338 and 911 keV peaks.

Nitrogen flushing at 5 lpm

The flow rate was then increased to 5 lpm in order to test if a further reduction could be achieved. A new flow meter, by Key Instruments, was installed to monitor the flow rate. The results after a one week measurement are shown in Table 8.4.

The results show a slight improvement from the 1 lpm flushing results. However, there also appears to be an increase in the previously reduced ^{212}Pb peak. Given the ^{228}Ac peak has not increased this could suggest contaminates were introduced into the detector volume which emanates thoron. Given these results, a nominal flushing

Chain/Nuclide	Energy (keV)	Boulby HPGe (cpd ±3σ)	Simulated ^{222}Rn (cpd ±3σ)	Boulby HPGe with purging (cpd ±3σ)
^{234}Th→^{234}Pa	63	16.7±1.6	3.85±0.11	10.3±0.9
^{234}Th→^{234}Pa	92	18.8±1.7	4.41±0.12	13.9±1.1
^{214}Pb→^{214}Bi	295	31.3±2.2	27.50±0.29	9.0±0.9
^{214}Pb→^{214}Bi	352	39.9±2.5	46.00±0.38	9.8±0.9
^{214}Bi→^{214}Po	609	34.4±2.3	38.54±0.35	8.2±0.8
^{235}U→^{231}Th	186	21.3±1.8	7.60±0.15	14.4±1.1
^{212}Pb→^{212}Bi	238	84.9±3.7	5.32±0.13	71.3±2.4
^{228}Ac→^{228}Th	338	22.7±1.9	2.24±0.08	22.2±1.4
^{228}Ac→^{228}Th	911	21.8±1.9	0.72±0.05	18.8±1.3
^{137}Cs→^{137}Ba	662	6.8±1.0	1.02±0.06	6.6±0.7
^{60}Co→^{60}Ni	1173	0.5±0.3	0.39±0.04	1.7±0.4
^{60}Co→^{60}Ni	1332	1.7±0.5	0.30±0.03	1.4±0.3
^{40}K→^{40}Ar	1461	17.2±1.6	0.30±0.3	15.1±1.1

Table 8.3: Comparison of results taken before and after nitrogen flushing at 1 lpm. The areas in grey are the radon daughter isotope decays. The simulated radon is based on a specific activity of 2.5 Bq/m^3 [94].

Chain/Nuclide	Energy (keV)	Boulby HPGe (cpd ±3σ)	Boulby HPGe with purging (cpd ±3σ) 2 weeks at 1 lpm	Boulby HPGe with purging (cpd ±3σ) 1 week at 5 lpm
^{234}Th→^{234}Pa	63	16.7±1.6	10.3±0.9	12.0±1.3
^{234}Th→^{234}Pa	92	18.8±1.7	13.9±1.1	19.5±1.6
^{214}Pb→^{214}Bi	295	31.3±2.2	9.0±0.9	8.0±1.1
^{214}Pb→^{214}Bi	352	39.9±2.5	9.8±0.9	8.3±1.1
^{214}Bi→^{214}Po	609	34.4±2.3	8.2±0.8	5.5±0.9
^{235}U→^{231}Th	186	21.3±1.8	14.4±1.1	13.4±1.4
^{212}Pb→^{212}Bi	238	84.9±3.7	71.3±2.4	81.7±3.4
^{228}Ac→^{228}Th	338	22.7±1.9	22.2±1.4	16.6±1.5
^{228}Ac→^{228}Th	911	21.8±1.9	18.8±1.3	17.8±1.6
^{137}Cs→^{137}Ba	662	6.8±1.0	6.6±0.7	5.0±0.8
^{60}Co→^{60}Ni	1173	0.5±0.3	1.7±0.4	2.2±0.6
^{60}Co→^{60}Ni	1332	1.7±0.5	1.4±0.3	2.2±0.6
^{40}K→^{40}Ar	1461	17.2±1.6	15.1±1.1	15.5±1.5

Table 8.4: Comparison of results taken during nitrogen flushing at 1 lpm and 5 lpm. The areas in grey are the radon daughter isotope decays [94].

rate of 1 lpm was established for all Boulby detectors as they have similar internal volume.

Improvements to Sensitivity

The reduction of radon and its daughter isotopes translates to an improved sensitivity for the ^{238}U lines. This can be seen in Figure 8.16, where the sensitivity is plotted as a function of time for the ^{214}Bi, 609 keV, line.

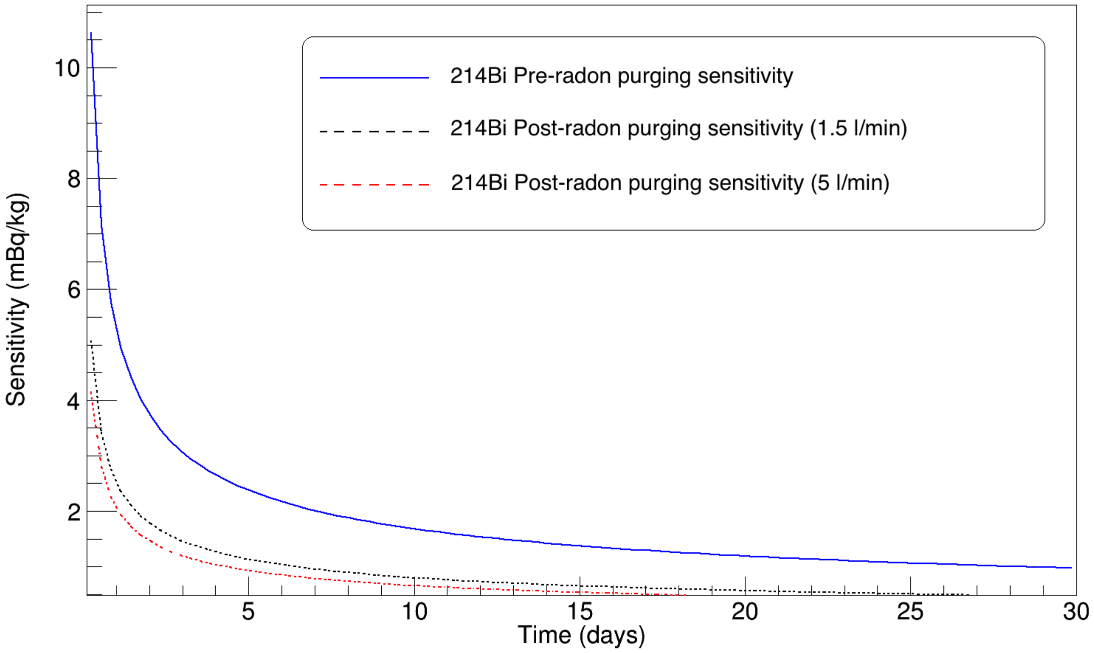

Figure 8.16: Sensitivity plot of the ^{214}Bi line for no nitrogen flushing, 1 l/min and 5 l/min shown as blue, black and red respectively. All limits set at 90% CL.

8.5.4. Shielding improvements

The first version of shielding constructed used interlocking lead bricks, 100 mm thick, followed by plates of copper, also 100 mm thick. The lid was made from a single lead block which had to be removed using a crane. Nitrogen flushing was achieved by feeding a gas line through the gap at the neck of the detector and an anti-radon shield was built around the castle. This design was impractical due to the time required to open and close the detector per sample insertion, in particular for calibration samples.

A new castle was designed with millimetre precision with the same thickness of lead and copper. The advantage of the new castle design is complete replicability of the castle geometry, ease of access to the detector and allows for a built-in nitrogen purging system. Care was taken to clean both the lead and copper before assembly. A comparison of the old and new castles are shown in Figure 8.17.


(a) Old Shielding **(b)** New Shielding **(c)** New Shielding Lid Open

Figure 8.17: Comparison of old and new shielding for Boulby germanium detectors.

After the detectors were installed into the new castle, they were calibrated and a background measurement was taken. From this the integrated counts from 100-2700 keV were determined and compared with data taken before the shielding modifications showing a factor 2 improvement. The result are shown in Table 8.5. There is still a factor 2 difference in backgrounds when compared against other world leading low background detectors such as Gator currently being operated at Gran Sasso underground laboratory [95]. However, presently it is unknown if this difference is dominated by external or internal backgrounds, since the Lunehead detector is not made to the same ultra-radio pure standard as the Gator facility detector.

The new shielding design allows all current and future detectors to interchange shielding depending on the measurement requirements. This means a detector is not limited to a single detection volume and can be placed in a larger castle if required by the sample's dimensions.

Detector Configuration	Events / min
Boulby initial state	1.303 ± 0.005
Boulby + cleaning	1.081 ± 0.003
Boulby + nitrogen flushing	0.751 ± 0.001
Boulby + shielding modification + nitrogen flushing	0.35 ± 0.004
The Gator facility (LNGS)	∼0.16

Table 8.5: Comparison of integrated counts over the range 100-2700 keV between stages of detector improvement of Lunehead at Boulby and the world leading ultra low background germanium detector.

8.6. Detector Relocation

A new underground facility was constructed at Boulby to replace the old laboratory building. The building of the new facility gave the opportunity to construct a dedicated low background measurement space called the Boulby Underground Germanium Suite (BUGS). BUGS is designed as a class 1000 cleanroom with; air conditioning to maintain stable temperature, a nitrogen gas line to deliver purging gas for HPGe detectors and a sample preparation area. The cleanroom further minimises variation in background as it reduces the level of contaminates in the air. All four detectors have been relocated inside the new facility and have been fully operational since April 2016.

8.7. Material Screening

Several samples have been measured for SuperNEMO. The most critical were the tracker high tensile screws and external tracker cables. The results allowed the collaboration to proceed with these components. One such measurement is presented below as an example of a standard germanium measurement.

Prior to preparing a sample for screening it is important to determine which detector is best suited for taking the measurement. The key factors are: the gamma lines of interest, sample mass and geometry.

8.7.1. Sample Preparation

The sample measured was the high tensile screws used in the construction of the SuperNEMO tracker module. The sample was first ultrasonically cleaned using Leksol, an industrial degreasing solvent. The container selected to hold the sample was a 1.46 litre marinelli beaker which are the standard sample holder for maximising counting efficiency, see Figure 8.19b. The marinelli beaker was cleaned using IPA prior before a total of 6.09 kg of the screws sample was inserted and sealed for the measurement, as shown in Figure 8.18. All sample preparations were carried out inside a cleanroom environment. Once the sample was prepared, it was wrapped and taken underground for measurement.

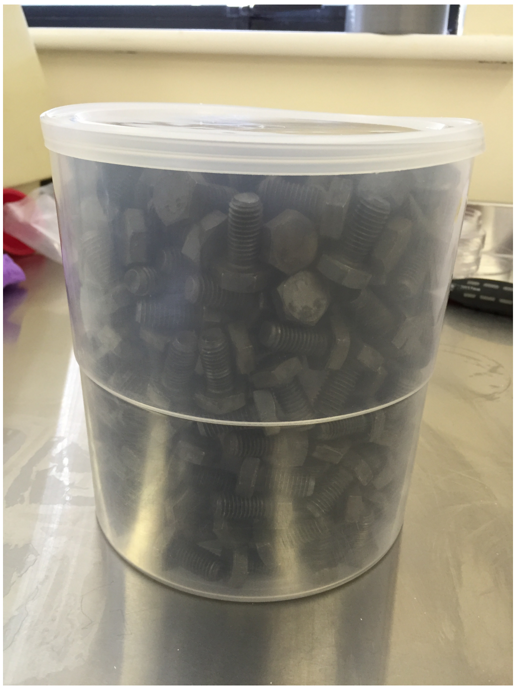

Figure 8.18: SuperNEMO external screws in a Marinelli beaker for measurement.

8.7.2. Simulation and Measurement

Once inside BUGS, the sample was unwrapped and the outside of the marinelli was wiped down using IPA to remove any contaminants. The sample was then placed directly on top of the Lunehead (coaxial) detector end cap for measurement, as shown in Figure 8.19a. This configuration was then be simulated using GEANT4, as shown in Figure 8.19b, to extract a detection efficiency, as shown in Figure 8.20.

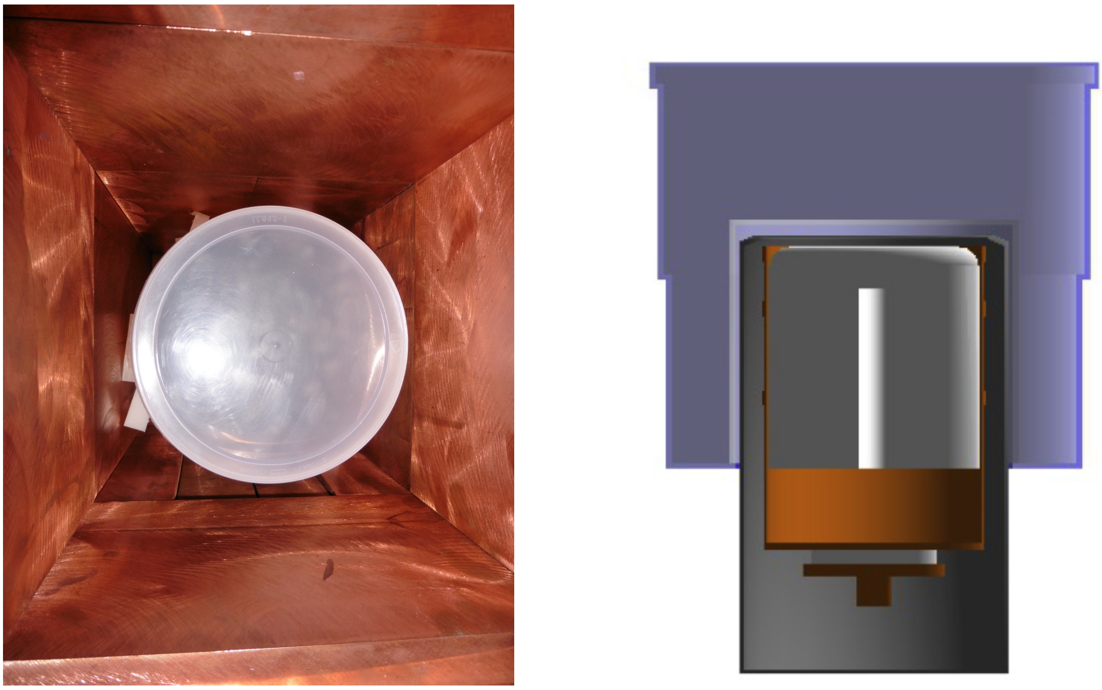

(a) Sample on HPGe detector for measurement.

(b) Simulation of sample on HPGe detector.

Figure 8.19: Sample of SuperNEMO external screws during HPGe measurement and the simulated sample geometry.

Using the detection efficiency and the known detector background, it is possible to calculate the duration of the measurement necessary to screen a sample below a desired level of sensitivity, in this case <10 mBq/kg.

8.7.3. Analysis and Results

After a 10 day measurement, the resultant spectrum was analysed and the net count of individual gamma peaks in the $\pm 3\sigma$ region of interest were fitted. The specific activity of each gamma line was then be calculated using Equation (8.2) and the main results are summarised in Table 8.6.

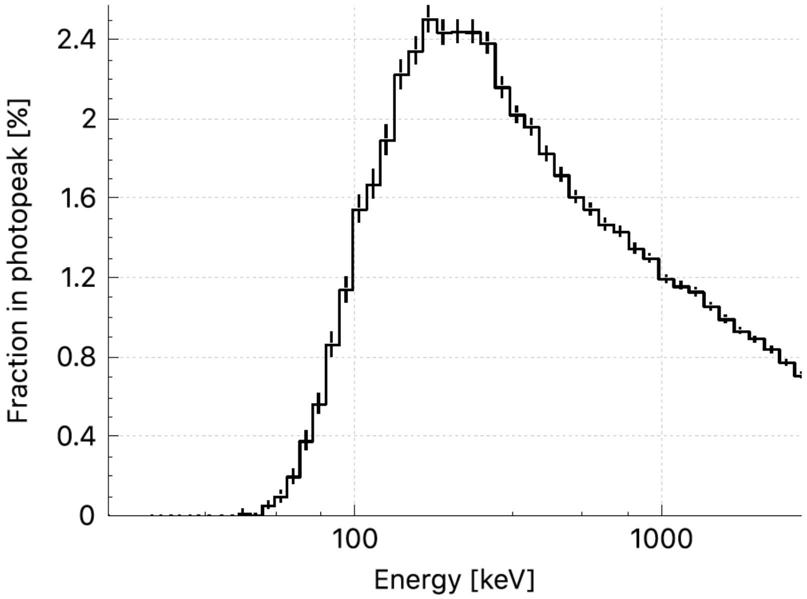

Figure 8.20: Simulated detection efficiency of the SuperNEMO external screw sample as a function of energy. Fraction in photopeak is the detection efficiency in the $\pm 3\sigma$ region.

Isotope	Specific Activity (Bq/kg)	Extrapolated (Bq)	Requirement (Bq)
^{234}Th	18.66 ± 3.94	1.87 ± 0.39	100
^{214}Bi	3.09 ± 0.37	0.31 ± 0.037	12.0
^{208}Tl	0.86 ± 0.38	0.09 ± 0.038	2.2
^{40}K	13.04 ± 3.63	1.30 ± 0.036	30

Table 8.6: Results from the SuperNEMO high tensile screws measurement with statistical uncertainties only given at 1 σ. There is also a 10% systematic uncertainties associated with all HPGe measurement results which has not been included. The extrapolated results show a total contribution of sample to the Demonstrator radon activity which can be compared to the requirement levels which are based on 10% of SuperNEMO PMT activity [96].

The total mass of the screws in the Demonstrator is ~100 kg. This activity was approximately equivalent to $< 10\%$ of the required level which meant the screws met the required level for Demonstrator construction.

8.7.4. Summary

A new underground gamma ray spectroscopy facility (BUGS) has been established at the Boulby Underground Laboratory. BUGS currently consists of 4 HPGe detectors which have undergone extensive improvements to reduce detector backgrounds, as demonstrated in Table 8.5, to reach world class screening capabilities. Automated analysis software has been developed to process data from each detector, this surpasses the current industry leading software. All detectors are fully operational with an occupancy rate of >80% and are being currently used for material screening for the SuperNEMO and LZ experiments.

Chapter 9.

Sensitivity Studies of the ^{96}Zr Double Beta Decay to the 0^+_1 Excited State of ^{96}Mo

The current uncertainty associated with NME calculations contributes the largest uncertainty on the determined effective neutrino mass. Results of $2\nu\beta\beta$ decay half-lives from experiments such as NEMO-3 provide information to validate and modify NME calculation parameters. Most isotopes capable of undergoing double-β decay to the ground state are also able to decay to 0^+_1 and 2^+_1 excited transition states. The measurement of decay modes to excited states can offer more insight in the nuclear structure of the decay process and provide additional input to the NME models which can further reduce problems associated with precise calculations as described in Section 2.9. In the case of QRPA models, the g_{pp} parameter (see Section 2.9.2) is different for transitions to ground or excited states [97, 98], therefore, a measurement of a decay to an excited state will test different aspects of the calculation method. The measurement of decay modes to excited states may also be used as a consistency check for single isotope $0\nu\beta\beta$ experiment to discriminate between true signal and unknown background [99].

The decay to excited state modes are suppressed due to the smaller transition energies and in the case of 2^+_1 it is further suppressed by angular momentum resulting in an even longer predicted half-live. There are 12 isotopes which have been observed to undergo $2\nu\beta\beta$ decay to the ground state, however, there has only been two (^{100}Mo [100] and ^{150}Nd [101]) which have been observed to undergo a $2\nu\beta\beta$ decay to the first excited 0_1^+ state. A good candidate for a third observation of a decay to the first excited state would be ^{96}Zr in light of its high phase space and Q value.

9.1. Double Beta Decay to Excited State of ^{96}Zr

The decay of ^{96}Zr to the ground state has been measured by the NEMO-3 collaboration [102]:

$$T_{1/2} = 2.35 \pm 0.14(stat.) \pm 0.16(syst.) \times 10^{19}\ \mathrm{yr}\,. \tag{9.1}$$

The ^{96}Zr isotope can also decay to excited states which is followed by a decay to the ground state via γ-ray emissions. The large Q value of the decay of ^{96}Zr means that several excited states of ^{96}Mo could exist, as shown in Figure 9.1. The main decay mode of interest are gammas emitted from the de-excitation of ^{96}Mo from the excited state, $0_1^+ \rightarrow 2^+ \rightarrow 0^+$, which will produce two gammas at 369.8 and 778.2 keV respectively. These de-excitation gammas can then be detected using a HPGe detector such as the detector described in Section 8.1.1. The Q values of the ground and first excited state are:

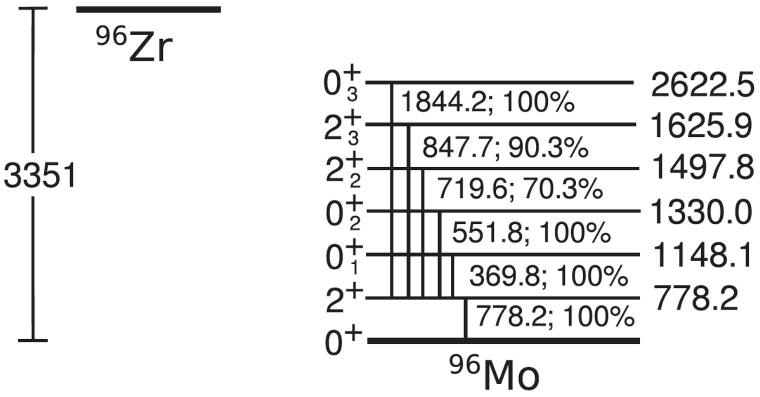

Figure 9.1: The decay states for ^{96}Zr to ^{96}Mo [103].

$$Q_{\beta\beta}(0_0^+) = 3.35\ \mathrm{MeV} \qquad \text{and} \qquad \mathrm{Q}_{\beta\beta}(0_1^+) = 2.20\ \mathrm{MeV}\,. \tag{9.2}$$

Therefore, the phase space of the decay to the first excited state is greatly reduced as a result of the lower Q value.

There has been no observation of the ^{96}Zr double-β decay to excited states so far. Theoretical calculations of the corresponding NME predict a half-life to the 0_1^+ state in the region of 2-4 $\times 10^{21}$ yr [104]. Another calculation provided a much lower half-life prediction of 2.59×10^{20} yr [105] that was however excluded by a recent experimental study that produces a lower bound on the half-life of $T_{1/2} > 3.1 \times 10^{20}$ yr (90% C.L.) [103].

Therefore, despite significant uncertainties in the theoretical calculations there is a clear motivation to study the ^{96}Zr double-β decay to the 0_1^+ excited state with a sensitivity at the level of 10^{21} yr. Below we investigate the sensitivity that can be reached with a large coaxial HPGe detector hosted at the Boulby underground laboratory. This method utilises the superb energy resolution of HPGe detectors to look for two gamma with the energies corresponding to the excited states of ^{96}Mo. Because only the gamma rays are detected this method cannot distinguish between the 2ν and 0ν modes of the decay but for obvious reasons it is essentially a search for the $2\nu\beta\beta$ decay to excited sates.

9.2. Experimental Method

9.2.1. The Detector

The proposed experiment consists of a single ultra-low background Canberra Lingolsheim coaxial detector with a crystal volume of 600 cm^3. In the simulations of the achievable sensitivity in this chapter, the detector simulations are based on a real LSM detector with known background levels.

This detector will be surrounded on all sides by a custom made castle consisting of 5 cm of ultra radio-pure electro-formed copper followed by 5 cm of high purity copper and then 15 cm of low radio-activity lead. The central volume will be purged continuously with nitrogen to suppress radon levels. The entire experimental setup would be located at the Boulby Underground Laboratory.

9.2.2. The sample

In order to improve on the current world limit a substantial mass of isotope is required for measurement. In its natural form zirconium only contains 2.8% of the isotope ^{96}Zr, so to increase isotope mass, the sample must either be enriched or increased in mass. Enrichment can increase isotope abundance to above 90%, this also has the added bonus of increasing the radio-purity of the sample as the enrichment process also eliminates most of the nuclear contaminants. Presently, only electromagnetic separation is available for ^{96}Zr enrichment, which is expensive and also has a low production rate. The simplest way to gain extra ^{96}Zr mass is by increasing the mass of zirconium measured which is also relatively cheap. However, it is essential to select a sample which is as radio-pure as possible, otherwise the sensitivity will be severely limited by background.

For this measurement several samples of zirconium oxide (ZrO_2), 100 grams each, were purchased from various suppliers to be screened for radio-purity. Zirconium oxide was used instead of pure zirconium as the sample was needed in its powdered form for preparation into containers and pure zirconium in powdered form is highly flammable and may spontaneously ignite in air.

A special container, as shown in Figure 9.2, was selected, due to its radio-purity, to house the sample for HPGe measurements. The container was cleaned using an ultrasonic bath filled with IPA then left to dry in a class 10,000 cleanroom. The samples were delivered in nitrogen sealed bottles which were only opened once inside the cleanroom. The samples were packaged inside the container which was weighed before and afterwards, as shown in Figure 9.2.

9.2.3. Zirconium Oxide Selection Result

A screening programme was carried out to screen four separate samples of ZrO_2 using the Boulby well detector. The results showed a high level of U and Th contamination for all the samples, as shown in Table 9.1.

The observed activities are higher than the required (10 μBq/kg for U and 2 μBq/kg for Th) radio-purity, to have an order of magnitude lower contribution to the background compared to that from the intrinsic HPGe background. However, there

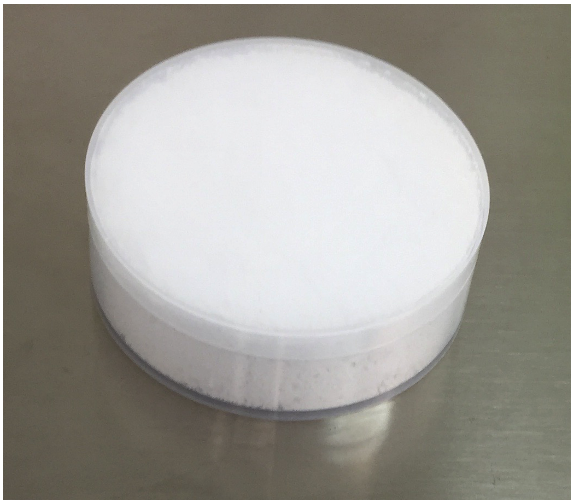

Figure 9.2: Sample of ^{96}Zr for measurement.

Sample	mass (g)	^{234}Th (U) (Bq/kg)	^{214}Bi (Bq/kg)	^{228}Ac (Th) (Bq/kg)	^{208}Tl (Bq/kg)
1	103.19	4.88±0.37	0.21±0.03	3.48±0.16	2.49±0.08
2	101.07	11.25±0.26	0.48±0.02	2.23±0.06	1.27±0.03
3	74.13	2.78±0.27	12.97±0.18	2.64±0.13	1.55±0.06
4	116.57	1.13±0.09	0.73±0.02	0.26±0.02	0.16±0.01

Table 9.1: Results from the measurements of ZrO_2 samples. Sample 1 is from Alfa Aesar product number 41528 [106], sample 2 is from Alfa Aesar product number 40140 [106], sample 3 is from Zircomet product number 74058 [107] and sample 4 is from HiCharms product number IDL292 [108].

exists processes of physical and chemical purification which can remove the U and Th content, for further detail please see [109]. These techniques have been developed through 15 years of R&D for NEMO-3 and continue as part of the preparation of the SuperNEMO source ^{82}Se. The purification process is expected to purify the zirconium sample to levels below 10 μBq/kg for U and 2 μBq/kg for Th as a result of the experience from the SuperNEMO purification programme. The process of purification remains considerably cheaper than enrichment. Simulations are used to determine the experimental sensitivity which can be achieved if the purification is successful.

9.2.4. Sample Holder

Once a sample has been selected it will be placed inside a specially designed Marinelli beaker which has been geometrically designed to optimise detection efficiency, as shown in Section 9.3.1. The Marinelli must be made from an extremely radio-pure material and have thin walls to ensure gammas are not obstructed by the container wall.

Several materials were considered but it was decided a marinelli constructed using Duracon holding 10-20 kg of the sample would be optimal. Experiments to find a 3D printing material of sufficient radio-purity were also conducted, as well as attempting to make Duracon into printing filaments. The result does not suggest a 3D printed marinelli can replace the conventional machine produced Marinelli containers at the current time for reasons of radio-purity. Once the sample is inserted into the Marinelli, it will sit directly above the detector end cap for measurement.

9.3. Sensitivity Study Results

MC studies were conducted using GEANT4 simulations to determine the potential half-life sensitivity of an experiment using up to 20 kg of highly pure natural zirconium oxide and a large HPGe detector for one to two years of counting. The predicted experimental sensitivity was determined using the formula;

$$T_{\frac{1}{2}} > \ln \frac{t \cdot BR \cdot N_0 \cdot \epsilon_D}{D_L} \tag{9.3}$$

where t is the exposure time, BR is the branching ratio of gamma peaks, N_0 is the number of nuclei, ϵ_D is the detection efficiency and D_L is the detection limit, i.e. the number of excluded events at a given confidence level. The definition of detection limit as stated in Section A.1 was used. In this study, B is taken as the background counts in the $\pm 3\sigma$ region around the gamma energies of interest where σ is the energy resolution of the detector at the given energy.

9.3.1. Detection Efficiency Estimates

The simulated detection efficiencies is sample and geometry dependent. The geometry is based on the ultra low background detector Obelix [110]. The accuracy of the GEANT4 simulations of the Obelix detector were tested by comparing the simulated detection efficiency results of a calibration source to an actual measurement of the source with known gamma activities as described in Section 8.2.3.

After the simulated detector results had been verified, simulations were carried out to determine the optimum geometry of a marinelli beaker in order to maximise detection efficiency. In theory this should be a container which evenly distributes the zirconium oxide sample on all sides to increase angular coverage and minimise sample self shielding and this was found to be true using GEANT4 simulations.

Due to geometrical constraints placed by the cold finger, the marinelli cannot extend over the side of the end cap by more than 13 mm. Therefore, a marinelli which extends 10 mm past the bottom of the end cap is chosen as the optimum sample geometry for maximal detection efficiency.

9.3.2. Experimental Potential

The estimated backgrounds for the experimental setup was based on the backgrounds measured by the Obelix detector [110] and the contribution in the regions of interest (ROI) after a year of counting are shown in Table 9.2.

Detector Backgrounds 1 Year (counts)		
369.8 keV	778.2 keV	1148 keV
437.5±68.3	192.1±45.3	213.4±47.7

Table 9.2: The Obelix detector background for 1 year of counting. The Obelix detector background in the $\pm 3\sigma$ region around the gamma lines of interest where σ is the detector energy resolution.

In addition the background contribution in the ROI from a purified sample of zirconium oxide with uranium and thorium levels at 10 and 2 μBq/kg respectively is shown in Table 9.3.

Mass (kg)	Backgrounds 1 Year (counts)		
	369.8 keV	778.2 keV	1148 keV
10	3.42±0.18	0.5±0.07	0.17±0.04
12.5	4.40±0.21	0.59±0.08	0.19±0.04
15	4.88±0.22	0.74±0.09	0.31±0.06
17.5	5.31±0.23	0.85±0.09	0.40±0.06
20	5.84±0.24	1.03±0.10	0.31±0.06

Table 9.3: Background contribution in the $\pm 3\sigma$ region around the gamma lines of interest, where σ is the detector energy resolution, as a result of a purified zirconium sample with uranium and thorium levels of 10 and 2 μBq/kg respectively.

Using the optimised geometry discussed above, the detection efficiency for a range of sample masses were simulated and the potential sensitivities that can be achieved were estimated, as shown in Table 9.4.

Mass (kg)	Detection Efficiency (%)		1 Year Half-life (yr)		2 Year Half-life (yr)	
	369.8 keV	778.2 keV	369.8 keV	778.2 keV	369.8 keV	778.2 keV
10	2.89	2.31	5.07×10^{20}	6.05×10^{20}	7.25×10^{20}	8.65×10^{21}
12.5	2.62	2.14	5.73×10^{20}	6.99×10^{20}	8.20×10^{20}	1.00×10^{21}
15	2.34	1.94	6.15×10^{20}	7.59×10^{20}	8.81×10^{20}	1.09×10^{21}
17.5	2.11	1.77	6.45×10^{20}	8.07×10^{20}	9.24×10^{21}	1.16×10^{21}
20	1.91	1.61	6.67×10^{20}	8.41×10^{20}	9.57×10^{21}	1.20×10^{21}

Table 9.4: Simulation results for the sensitivity to search for the ^{96}Zr double-β decay to the 0_1^+ excited state of ^{96}Mo using an Obelix-type HPGe detector. The sensitivities are reported at 95% CL for 1 and 2 years of data taking.

The sensitivity can be further improved by searching for the decay to the 0_1^+ excited state through the combined 369.8 and 778.3 keV channels. The sensitivities achievable using this method are shown in Table 9.5.

The study shows that a factor 2 improvement on the existing best limit can be achieved with a modest 10 kg of radio-pure natural zirconium oxide and one year of measurement to reach a sensitivity of 7.64×10^{20}yr.

Mass (kg)	Detection Efficiency (%)	Combined Peak Half-life (yr)	
		1 Year	2 Year
10	5.20	7.64×10^{20}	1.09×10^{21}
12.5	4.76	8.72×10^{20}	1.24×10^{21}
15	4.28	9.41×10^{20}	1.34×10^{21}
17.5	3.87	9.94×10^{20}	1.42×10^{21}
20	3.52	1.03×10^{21}	1.47×10^{21}

Table 9.5: Simulation results for the sensitivity to search for the ^{96}Zr double-β decay to the 0_1^+ excited state of ^{96}Mo using an Obelix-type HPGe detector, with the combined gamma peaks of 369.8 keV and 778.2 keV. The sensitivities are reported at 95% CL for 1 and 2 years of data taking.

The sensitivity reach of the experiment can be further improved by reducing the background levels of the HPGe detector. This can be done by replacing the detector end cap and internal components with the latest materials of greater radio-purity offered by Canberra. Better shielding and veto systems can also be introduced to further suppress background levels.

Chapter 10.

Conclusion

SuperNEMO is a modern $0\nu\beta\beta$ decay experiment with a design capability to reach a half-life sensitivity of 10^{26} yr. It uses 3D topology reconstruction of each detected event to provide a unique and powerful background rejection method and evidence for the decay process. To achieve the required sensitivity, stringent radio-purity requirements are imposed for both the construction materials and the gas in the tracking chamber to minimise background radiation.

Radon is a highly diffusive radioactive gas with a relatively long half-life and it is a decay product of U and Th. Therefore, it can be found to emanate from all materials and forms a major background to double-β decay and direct dark matter detection experiments. It is essential to be able to accurately measure the radon emanation rate of materials.

To achieve the SuperNEMO design sensitivity, the radon levels inside the gaseous tracker volume must be < 0.15 mBq/m^3. Commercial radon detectors are only able to measure radon content to levels of 100 mBq/m^3. Therefore, a specialised electrostatic detector was commissioned which had a measured background of 7.3 ± 0.6 cpd which translates to a sensitivity of:

$$0.27 \pm 0.02 \text{ mBq}, \qquad 3.82 \pm 0.28 \text{ mBq/m}^3 . \tag{10.1}$$

In order to measure and confirm that the challenging radon target has been achieved, a radon concentration line (RnCL) was developed to be used in conjunction with the electrostatic radon detector which allowed the measurement of large gas volumes. Modifications were made to the carbon trap on the RnCL resulting in a factor of 2 improvement in the trapping and transfer efficiency. The RnCL has demonstrated it is able to achieve sensitivity of 20 µBq/m^3 using 8.4 m^3 of gas, the volume used for a standard tracker radon measurement.

To ensure the gas used for the RnCL measurement was radon-free, a gas purification system was commissioned and tested which showed a radon suppression factor of >20 when nitrogen is used as the carrier gas. The suppression factor is expected to be much higher, of order 10^{10}, for helium as the atomic size of helium is much smaller. Using helium as the carrier gas the RnCL can reach an ultimate sensitivity of ∼5 μBq/m^3 for large gas volumes making the RnCL one of the world's best facilities for ultra-low background studies.

The RnCL was built for the measurement of radon emanation from the SuperNEMO quarter tracker modules during construction. The quarter trackers can be tested for radon emanation before and after cell insertion to disentangle the source of radon emanation. The radon measurement result from the first three fully instrumented C-Sections are as follows:

$$\begin{aligned} C0 \qquad & A < 11.37 \pm 1.44 \text{ mBq (90\% CL)} \\ C1 \qquad & A < 15.26^{+2.50}_{-3.82} \text{ mBq (90\% CL)} \\ C2 \qquad & A < 4.36 \pm 1.31 \text{ mBq (90\% CL)}\,. \end{aligned}$$

Combining the radon activity results of measured C-Sections and extrapolating this result to the full tracker of the SuperNEMO Demonstrator gives:

$$A = 41.0 \pm 4.6 \text{ mBq}, \qquad a = 2.7 \pm 0.3 \text{ mBq/m}^3\,. \tag{10.2}$$

By replacing the Demonstrator tracking gas continuously at a flow-rate of 33.3 lpm, this radon activity can be further suppressed by a factor 18.4. Therefore, the radon activity within the tracking gas would be less than the target level of <0.15 mBq/m^3, achieving the challenging radon target required by SuperNEMO.

A radon emanation chamber was also constructed to be used in conjunction with the large low background electrostatic radon detector to carry out radon emanation measurements optimised for small samples with a large surface area. No background contribution from the chamber itself has been observed making it capable to perform radon emanation assays with a sensitivity of:

$$\text{Chamber 1} :< 0.19 \text{ mBq} \tag{10.3}$$

Direct measurements of radon emanation of detector components in their final configuration are critical as radon emanation is heavily geometry dependent and this is the only way to determine the true emanation level. A number of samples have already been measured for SuperNEMO and LZ and the results provided important input into the radio-purity budgets of both experiments.

In the quest for ever more radio-pure experimental detectors, gamma ray spectroscopy using high purity germanium (HPGe) detectors are essential for material screening. A new HPGe facility, BUGS, has been established at Boulby Underground Laboratory. From a single detector, there are currently four detectors including; a coaxial detector, a well detector, a BEGe detector and a pre screening BEGe at the BUGS. Each are housed in custom made shielding to prevent external backgrounds. Together they are able to perform a large and diverse range of measurements from low energy measurements with the BEGe detector to small sample measurements with high efficiency using the well detector.

An analysis programme has been developed for the processing of germanium data from BUGS. This analysis was verified using calibration sources of known activities to better than 10%, as well as by comparing to results produced using industry leading analysis software provided by Canberra.

Several steps have been taken to improve the detector's sensitivity, starting with cleaning of the lead and copper shielding, followed by introducing nitrogen purging and finally designing customised shielding. The number of background counts in the 100-2700 keV range was reduced by almost a factor 4.

Having commissioned the BUGS detectors, simulations were carried out for a potential experimental measurement of the ^{96}Zr double-β decay to the 0_1^+ excited state of ^{96}Mo. ^{96}Zr is the next best candidate for a third observation of a double-β decay to the 0_1^+ excited state which can provide important information to constraint NMEs.

The simulations showed it is possible to achieve a factor 4 improvement on current world leading limits on the decay of ^{96}Zr to its first excited state with the need for a zirconium purification process. The experiment would require a large ultra low background germanium detector, with a crystal mass of more than 3 kg, measuring a 20 kg sample of purified natural zirconium oxide for 2 years, producing an sensitivity of:

$$T_{1/2} = 1.47 \times 10^{21}\ \text{yr (at 90\% CL)}\,.$$

The RnCL has clearly achieved its primary purpose to measure the SuperNEMO quarter trackers for radon emanation, at ultra low levels, during construction. The Demonstrator is on track to meet its stringent radio-purity requirements for the both tracker gas and the detector components. At the time of writing this thesis, the assembly of the Demonstrator module is nearly complete.

Looking to the future, first measurement results from the Demonstrator will confirm if the challenging radio-purity requirements have been fulfilled. The RnCL will be re-purposed to carry out studies of radon properties such as emanation rate at extremely low temperatures. The facilities at the Boulby Underground Laboratory would be an ideal location to house a large ultra-low background HPGe for a measurement of ^{96}Zr double-β decay to the 0_1^+ excited state.

Appendix A.

Appendix A

A.1. Minimum Detectable Activity

To determine the sensitivity of the detector and the radon emanation chamber a rigorous definition must first be defined for the sensitivity of a measurement. In this case, the definition of Minimum Detectable Activity (MDA) as stated in 'Radiation Detection and Measurement' by G. F. Knoll [78] was used as briefly outlined below.

A.1.1. Detection Limit

In the simple case of a counting experiment, for a sample of unknown activity in a detector, the net counts N_S can be calculated as:

$$N_S = N_T - N_B \tag{A.1}$$

where N_T is the total counts with the sample present and N_B is the background counts. The critical limit, L_C, is the activity level above which a positive measurement can be claimed with an associated confidence level. To determine if the sample has any activity compare N_S with the critical limit, if $N_S > L_C$ then activity is present, if $N_S < L_C$ then no activity is present. When Gaussian distributions result from measuring both N_B and N_T for a sufficient time the result of subtracting one from the other should result in a Gaussian with a mean of the net number of counts and a standard deviation of:

$$\sigma_{N_S}^2 = \sigma_{N_T}^2 + \sigma_{N_B}^2 \,. \tag{A.2}$$

In the case where no activity is present in the sample, then $N_B = N_T$ and the mean of N_S are zero with a standard deviation of:

$$\sigma_{N_S} = \sqrt{2}\sigma_{N_B} = \sqrt{2N_B} \,. \tag{A.3}$$

Any measurement of signal will therefore be false positive hence L_C should be set sufficiently high to reduce the probability of $N_S > L_C$ down to a predetermined level. For a false positive probability of less than 10% L_C should be set at:

$$L_C = 1.64\sigma_{N_S} = \sqrt{2}\sigma_{N_B} = 2.326\sigma_{N_B} \,. \tag{A.4}$$

When activity is present in sample the mean of N_S should be positive. The size of N_S required to minimise the probability of false negative result to a predetermined level is defined as the detection limit, N_D. When the probability of false negatives is less than 10%, 90% of the Gaussian distribution of N_D must be above L_C:

$$N_D = L_C + 1.64\sigma_{N_D} \tag{A.5}$$

where σ_{N_D} is the standard deviation of the Gaussian distribution about the N_D mean. Since $N_S = N_D$:

$$\sigma_{N_D}^2 = \sigma_{N_T}^2 + \sigma_{N_B}^2 = \left(\sqrt{N_T}\right)^2 + \left(\sqrt{N_B}\right)^2 = N_D + 2N_B \,, \tag{A.6}$$

$$\sigma_{N_D} = \sqrt{N_D + 2N_B} \,. \tag{A.7}$$

Combining (A.7) and (A.4) into (A.5) gives:

$$N_D = 1.64\left(\sqrt{2N_B} + \sqrt{N_D + 2N_B}\right) \tag{A.8}$$

Solving for N_D gives:

$$N_D = 2.71 + 4.65\sqrt{N_B} \tag{A.9}$$

A.1.2. Minimum Detectable Activity

The Knoll definition is based on a binary decision of whether the detector output is background or signal plus background. Prior to each measurement the probabilities of a false positive (a background event being classed as a signal event) or a false negative (a signal event being is accepted as a background event) must be defined. A critical number of counts, n_c, must also be predefined above which a signal can be claimed to be present.

Given a well known number of expected background events, B, and a measurement confidence level, CL, the n_c is defined so that the probability of a false positive is less than 1 - CL,see Fig A.1.

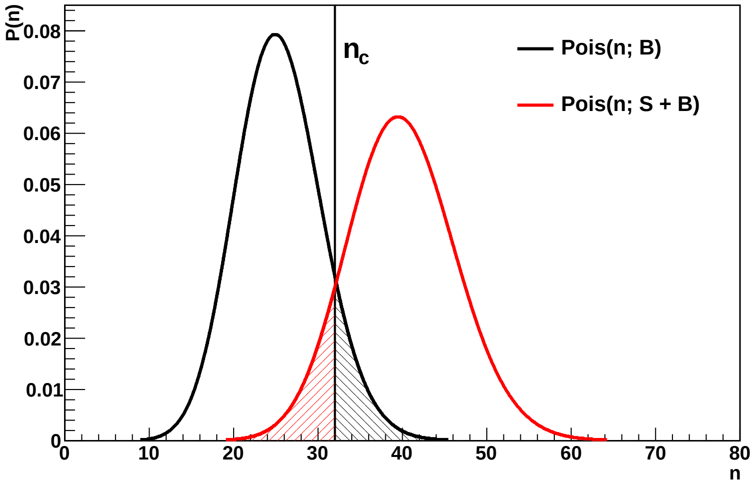

Figure A.1: The black curve represents the expected Poisson distributed background, from which n_c has been set so that the black shaded area corresponds to $1 - \text{CL}$. The red line is the distribution for the minimum signal on the same background, where S has been set such that the red shaded area also corresponds to $1 - \text{CL}$ [19].

If B is Poisson-distributed in order to satisfy the above criterion n_c must be increased until the following inequality is satisfied:

$$P_B(n \geq n_c) = \sum_{n=n_c}^{\infty} Pois(n; B) = 1 - \sum_{n=0}^{n_c-1} e^{-B}\frac{B^n}{n!} \leq 1 - \text{CL} \tag{A.10}$$

Once n_c has been set to reduce the probability of false positives to $1 - \mathrm{CL}$, the probability for false negatives can be used to calculate the minimum expected number of signal events, S, that satisfy the MDA requirement. Therefore, S is increased until the following is true:

$$P_{S+B}(n < n_c) = \sum_{n=0}^{n_c-1} Pois(n; S+B) = \sum_{n=0}^{n_c-1} e^{-(S+B)} \frac{(S+B)^n}{n!} \leq 1 - \mathrm{CL} \quad \text{(A.11)}$$

where n_c is increased until the false positive result corresponding to the black shaded area has a sufficiently low probability. Then S is increased until the red shaded area corresponding to the false negative result also has area $1 - \mathrm{CL}$. Once the minimum signal is been found, it can be converted into an activity. This minimum activity is what is referred to as the MDA.

A.1.3. The Normal Approximation

The Poisson distribution is difficult to work with analytically so for sample sizes where, y, is sufficiently large the Poisson distribution can be approximated by the normal distribution, as a result of the poisson convergence theorem. Hence:

$$Pois(y) \approx Norm(\mu = y, \sigma = \sqrt{y}) \quad \text{(A.12)}$$

.

The continuity correction $n_c \rightarrow n_c - \frac{1}{2}$ if then applied to further improved the approximation. Hence, equation (A.10), when $y = B$, becomes

$$P_B(n \geq n_c) \approx \int_{n_c-\frac{1}{2}}^{\infty} \frac{1}{\sqrt{2\pi B}} e^{-\frac{(x-B)^2}{2B}} dx = \frac{1}{2} - \frac{1}{\sqrt{\pi}} \int_0^{\frac{n_c-\frac{1}{2}-B}{\sqrt{2B}}} e^{-t^2} dt \quad \text{(A.13)}$$

.

The error function, is defined as

$$\mathrm{erf}(x) = \frac{2}{\sqrt{\pi}} \int_0^x e^{-t^2} dt \tag{A.14}$$

Using this definition and equations (A.10) and (A.13) it can be seen that

$$P_B(n \geq n_c) \approx \frac{1}{2}\left(1 - \mathrm{erf}\left(\frac{n_c - \frac{1}{2} - B}{\sqrt{2B}}\right)\right) \leq 1 - \mathrm{CL} \tag{A.15}$$

The equivalent procedure can be applied to equation (A.11) to give

$$P(n < n_c) \approx \frac{1}{2}\left(1 + \mathrm{erf}\left(\frac{n_c - \frac{1}{2} - (S+B)}{\sqrt{2(S+B)}}\right)\right) \leq 1 - \mathrm{CL} \tag{A.16}$$

The MDA definition provides the smallest value of S for a given B, so n_c can be eliminated. (A.15) and (A.16) are combined to find

$$S - \sqrt{2B}E \geq \sqrt{2(S+B)}E \tag{A.17}$$

where E is a positive number defined as:

$$E = \mathrm{erf}^{-1}(2\mathrm{CL} - 1) \tag{A.18}$$

Excluding the unphysical solution where $S \leq 0$, it is found that

$$S \geq 2E(E + \sqrt{2B}) \tag{A.19}$$

Hence, the MDA can be calculated from the minimum number of signal events that are detectable, S_0, which is the minimum value of S and given by

$$S_0 = 2E(E + \sqrt{2B}) \tag{A.20}$$

Bibliography

[1] D. Griffiths, *Introduction to elementary particles.* WILEY-VCH, (2004).

[2] C. Cowan, F. Reines, F. Harrison, H. Kruse, and A. McGuire, *Detection of the free neutrino: A Confirmation*, Science **124** (1956) 103–104.

[3] R. Davis and D. S. Harmer, *Attempt to Observe the* Cl^{37} $(\bar{\nu}, e^{-})$ Ar^{37} *Reaction Induced by Reactor Antineutrinos*, Bull. Am. Phys. Soc **4** (1959) 217.

[4] E. J. Konopinski and H. M. Mahmoud, *The Universal Fermi Interaction*, Phys. Rev. **92** (1953) 1045–1049.

[5] University of Zurich, *Standard Model, modified on 25 April 2015*, `http://www.physik.uzh.ch/groups/serra/StandardModel.html`.

[6] G. Danby, J. Gaillard, K. A. Goulianos, et al., *Observation of High-Energy Neutrino Reactions and the Existence of Two Kinds of Neutrinos*, Phys. Rev. Lett. **9** (1962) 36–44.

[7] DONUT Collaboration, K. Kodama, N. Ushida, C. Andreopoulos, et al., *Observation of tau neutrino interactions*, Phys. Lett. B. **504** (2001) 218–224.

[8] B. Adeva et al., *Measurement of* Z^0 *decays to hadrons, and a precise determination of the number of neutrino species*, Phys. Lett. B. **237** (1990) no. 1, 136–146.

[9] S. Schael et al., *Precision electroweak measurements on the Z resonance*, Phys. Rept. **427** (2006) 257–454.

[10] K. Eguchi, S. Enomoto, et al., *First Results from KamLAND: Evidence for Reactor Antineutrino Disappearance*, Phys. Rev. Lett. **90** (2003) 021802.

[11] B. Pontecorvo, *Mesonium and anti-mesonium*, Sov. Phys. JETP **6** (1957) 429.

[12] B. Pontecorvo, *Inverse beta processes and nonconservation of lepton charge*, Sov. Phys. JETP **7** (1958) 172–173.

[13] B. Kayser, *Neutrino physics*, eConf **C040802** (2004) L004.

[14] M. C. Gonzalez-Garcia, M. Maltoni, and T. Schwetz, *Updated fit to three neutrino mixing: status of leptonic CP violation*, arXiv (2014) , `arXiv:1409.5439 [hep-ph]`.

[15] E. Majorana, *Theory of the Symmetry of Electrons and Positrons*, Nuovo Cim. **14** (1937) 171–184.

[16] M. Goeppert-Mayer, *Double Beta-Disintergration*, Phys. Rev. **48** (1935) no. 6, 512–516.

[17] M. G. Inghram and J. H. Reynolds, *Double Beta-Decay of* Te^{130}, Phys. Rev. **78** (1950) 822–823.

[18] S. R. Elliott, A. A. Hahn, and M. K. Moe, *Direct evidence for two-neutrino double-beta decay in* $^{82}\mathrm{Se}$, Phys. Rev. Lett. **59** (1987) 2020–2023.

[19] J. E. Mott, *Search for double beta decay of* ^{82}Se *with the NEMO-3 detector and development of apparatus for low-level radon measurements for the SuperNEMO experiment.* PhD thesis, University College London, 2013.

[20] F. T. Avignone, S. R. Elliott, and J. Engel, *Double Beta Decay, Majorana Neutrinos, and Neutrino Mass*, Rev. Mod. Phys. **80** (2008) 481–516.

[21] W. H. Furry, *On Transition Probabilities in Double Beta-Disintergration*, Phys. Rev. **56** (1939) no. 12, 1184–1193.

[22] S. M. Bilenky, S. Pascoli, and S. T. Petcov, *Majorana neutrinos, neutrino mass spectrum,* CP *violation, and neutrinoless double* β *decay: The three-neutrino mixing case*, Phys. Rev. D **64** (2001) 053010.

[23] J. Vergados, H. Ejiri, and F. Simkovic, *Theory of Neutrinoless Double Beta Decay*, Rept. Prog. Phys. **75** (2012) 106301.

[24] SuperNEMO Collaboration, R. Arnold et al., *Probing New Physics Models of Neutrinoless Double Beta Decay with SuperNEMO*, Eur. Phys. J. **C70** (2010) 927–943.

[25] J. Menendez, A. Poves, E. Caurier, and F. Nowacki, *Disassembling the Nuclear Matrix Elements of the Neutrinoless beta beta Decay*, Nucl. Phys. **A818** (2009) 139–151.

[26] M. Kortelainen and J. Suhonen, *Nuclear matrix elements of $0\nu\beta\beta$ decay with improved short-range correlations*, Phys. Rev. C. **76** (2007) no. 2, 024315.

[27] J. Barea and F. Iachello, *Neutrinoless double-β decay in the microscopic interacting boson model*, Phys. Rev. C. **79** (2009) no. 4, 044301.

[28] P. Rath, R. Chandra, K. Chaturvedi, P. Raina, and J. Hirsch, *Uncertainties in nuclear transition matrix elements for neutrinoless $\beta\beta$ decay within the projected-Hartree-Fock-Bogoliubov model*, Phys. Rev. C. **82** (2010) no. 6, 064310.

[29] T. R. Rodriguez and G. Martinez-Pinedo, *Energy density functional study of nuclear matrix elements for $0\nu\beta\beta$ decay*, Phys. Rev. Lett. **105** (2010) 252503.

[30] Particle Data Group, J. Beringer et al., *Review of Particle Physics*, Phys. Rev. D. **D86** (2012) 010001.

[31] Troitsk Collaboration, V. Aseev et al., *An upper limit on electron antineutrino mass from Troitsk experiment*, Phys. Rev. D. **D84** (2011) 112003.

[32] C. Kraus, B. Bornschein, L. Bornschein, J. Bonn, B. Flatt, et al., *Final results from phase II of the Mainz neutrino mass search in tritium beta decay*, Eur. Phys. J. **C40** (2005) 447–468.

[33] T. Bowles and R. Robertson, *Tritium beta decay and the search for neutrino mass*, Los Alamos Sci. **25** (1997) 86–91.

[34] G. Drexlin, V. Hannen, S. Mertens, and C. Weinheimer, *Current direct neutrino mass experiments*, Adv. High Energy Phys. **2013** (2013) 293986.

[35] K. N. Abazajian, E. Calabrese, A. Cooray, et al., *Cosmological and astrophysical neutrino mass measurements*, Astropartic. Phys. **35** (2011) no. 4, 177–184.

[36] A. Gando, Y. Gando, T. Hachiya, et al., *Search for Majorana neutrinos near the inverted mass Hierarchy region with KamLAND-Zen*, Phys. Rev. Lett. **117** (2016) no. 8, 082503.

[37] P. Silvia, *A portal to new physics*, CERN Courier (2016) .

[38] T. Ohlsson, H. Zhang, and S. Zhou, *Probing the leptonic Dirac CP-violating phase in neutrino oscillation experiments*, Phys. Rev. D. **D87** (2013) 053006.

[39] F. F. Deppisch, M. Hirsch, and H. Päs, *Neutrinoless double-beta decay and physics beyond the standard model*, Journal of Physics G: Nuclear and Particle Physics **39** (2012) no. 12, 124007.

[40] W. Rodejohann, *Neutrinoless double beta decay and neutrino physics*, J. Phys. G. **G39** (2012) 124008.

[41] Tosaka, *Uranium Decay chain, modified on 21 November 2014*, `https://commons.wikimedia.org/wiki/File:Decay_chain(4n%2B2,_Uranium_series).PNG`.

[42] Tosaka, *Thorium Decay chain, modified on 15 October 2009*, `https://commons.wikimedia.org/wiki/File:Decay_chain(4n,Thorium_series).PNG`.

[43] National Academy of Sciences, National Academy of Engineering, Institute of Medicine, National Research Council, A. J. LANKFORD, Y. ALHASSID, et al., *An Assessment of the Deep Underground Science and Engineering Laboratory (DUSEL)*, tech. rep., (2011).

[44] J. R. Wilson, *Non-accelerator Neutrino Physics*, IoP HEPP & APP Group Meeting, (2013).

[45] KamLAND-Zen Collaboration, A. Gando et al., *Limit on $0\nu\beta\beta$ Decay of ^{136}Xe from the First Phase of KamLAND-Zen and Comparison with the Positive Claim in ^{76}Ge*, Phys. Rev. Lett. **110** (2013) no. 6, 062502.

[46] KamLAND-Zen Collaboration, A. Gando et al., *Limits on Majoron-emitting double-beta decays of ^{136}Xe in the KamLAND-Zen experiment*, Phys. Rev. C. **C86** (2012) 021601.

[47] KamLand-Zen Collaboration, J. Shirai, *KamLAND-Zen: Status and Future*, Nucl. Phys. Proc. Suppl. **237-238** (2013) 28–30.

[48] S. Umehara, T. Kishimoto, I. Ogawa, R. Hazama, H. Miyawaki, et al., *Neutrino-less double-beta decay of ^{48}Ca studied by CaF_2(Eu) scintillators*,

Phys. Rev. C. **C78** (2008) 058501.

[49] F. Piquemal, *Future double beta decay experiments*, Nucl. Phys. Proc. Suppl **235** (2013) no. 236-273, .

[50] E. Andreotti, C. Arnaboldi, F. Avignone, et al., *^{130}Te Neutrinoless Double-Beta Decay with CUORICINO*, Astropart. Phys. **34** (2011) 822–831.

[51] K. Alfonso, D. Artusa, A. III, et al., *Search for Neutrinoless Double-Beta Decay of ^{130}Te with CUORE-0*, Phys. Rev. Lett. **115** (2015) no. 10, 102502.

[52] L. Canonica, *Status and prospects for CUORE, XXVII International Conference on Neutrino Physics and Astrophysics (Neutrino 2016), London, 4-9 July, 2016*, (2016).

[53] H. Klapdor-Kleingrothaus, A. Dietz, L. Baudis, G. Heusser, I. Krivosheina, et al., *Latest results from the Heidelberg-Moscow double beta decay experiment*, Eur. Phys. J. **A12** (2001) 147–154.

[54] C. Aalseth, F. Avignone, R. Brodzinski, W. Hensley, H. Miley, et al., *Recent results of the IGEX ^{76}Ge double-beta decay experiment*, Phys. Atom. Nucl. **63** (2000) 1225–1228.

[55] H. Klapdor-Kleingrothaus, I. Krivosheina, A. Dietz, and O. Chkvorets, *Search for neutrinoless double beta decay with enriched ^{76}Ge in Gran Sasso 1990-2003*, Phys. Lett. B. **586** (2004) 198–212.

[56] GERDA Collaboration, M. Agostini, M. Allardt, E. Andreotti, et al., *Results on Neutrinoless Double-β Decay of ^{76}Ge from Phase I of the GERDA Experiment*, Phys. Rev. Lett. **111** (2013) no. 12, 122503.

[57] GERDA Collaboration, K. Knöpfle, *GERDA - Status and Perspectives*, Nucl. Phys. Proc. Suppl. **237-238** (2013) 31–33.

[58] Majorana Collaboration, N. Abgrall et al., *The Majorana Demonstrator Neutrinoless Double-Beta Decay Experiment*, Adv. High Energy Phys. (2013) .

[59] Majorana Collaboration, C. Cuesta, *Background model for the Majorana Demonstrator*, arXiv (2016) , `arXiv:1610.01146 [physics.ins-det]`.

[60] J. Ebert, M. Fritts, D. Gehre, et al., *Results of a search for neutrinoless*

double-β decay using the COBRA demonstrator, Phys. Rev. C **94** (2016) 024603.

[61] The EXO-200 Collaboration, *Search for Majorana neutrinos with the first two years of EXO-200 data*, Nature **510** (2014) no. 7504, 229–234.

[62] R. Henning, *Current status of neutrinoless double-beta decay searches*, Reviews in Physics **1** (2016) 29–35.

[63] J. Martín-Albo, J. M. Vidal, P. Ferrario, et al., *Sensitivity of NEXT-100 to neutrinoless double beta decay*, arXiv (2015) , `arXiv:1511.09246 [physics.ins-det]`.

[64] R. Arnold, C. Augier, J. Baker, et al., *Results of the search for neutrinoless double-β decay in ^{100}Mo with the NEMO-3 experiment*, Phys. Rev. D **92** (2015) no. 7, 072011.

[65] R. Saakyan, *Tracking-based Experiments in Double Beta Decay*, Nucl. Phys. Proc. Suppl. **229-232** (2012) 135–140.

[66] The SuperNEMO Collaboration, *SuperNEMO Conceptual Design Report*, tech. rep., (2010).

[67] R. Saakyan, *Tracking-based Experiment in Double Beta Decay*, Nucl. Phys. Proc. Suppl. **00** (2011) 1–6.

[68] SuperNEMO Collaboration, H. Gómez, *BiPo: A dedicated radiopurity detector for the SuperNEMO experiment*, AIP Conference Proceedings **1549** (2013) no. 1, 94–97.

[69] S. W. Ramsay and R. Whytlaw-Gray, *La densité de l'émanation du Radium*, Comptes rendus hebdomadaires des séances de l'Académie de Sciences **151** (1910) 126–128.

[70] V. Vasiliev, *Radon in SuperNEMO*, Internal Note (2008) DocDB:297.

[71] J. Mott and C. Vilela, *Flow rate study with single cell First Radon measurements of the gas system*, tech. rep., University College London, (2013).

[72] S. De Capua and P. Guzowski, *Flow rate study*, Internal Note (2014) DocDB:3146.

[73] E. Choi, M. Komori, K. Takahisa, et al., *Highly sensitive radon monitor and radon emanation rates for detector components*, Nucl. Instrum. Meth. **A459** (2001) 177–181.

[74] C. Mitsuda, T. Kajita, K. Miyano, S. Moriyama, et al., *Development of super-high sensitivity radon detector for the Super-Kamiokande detector*, Nucl. Instrum. Meth. **A497** (2003) 414–428.

[75] E. Wellisch, *The distribution of the active deposit of radium in an electric field*, Philosophical Magazine Series 6 **26** (1913) no. 154, 623–635.

[76] P. Pagelkopf and J. Porstendörfer, *Neutralisation rate and the fraction of the positive* ^{218}*Po-clusters in air*, Atmospheric Environment **37** (2003) no. 8, 1057 – 1064.

[77] B. N. Laboratory, *National Nuclear Data Center*, http://www.nndc.bnl.gov/nudat2/ .

[78] G. Knoll, *Radiation Detection and Measurement*, ISBN-9780470131480 (2000) .

[79] SuperNEMO Collaboration, J. Busto, *Radon adsorption in nanoporous carbon materials*, AIP Conference Proceedings **1549** (2013) no. 1, 112–115.

[80] G. Heusser, W. Rau, B. Freudiger, M. Laubenstein, M. Balata, and T. Kirsten, ^{222}*Rn detection at the* $\mu Bq/m^3$ *range in nitrogen gas and a new Rn purification technique for liquid nitrogen*, Applied Radiation and Isotopes **52** (2000) no. 3, 691 – 695.

[81] J. Busto, *Design of a Preliminary Anti-Radon System*, Internal Presentation (2014) DocDB:3117.

[82] J. E. Mott, *First radon measurements of C0*, Internal SuperNEMO Technical Report (2013) DocDB:2957.

[83] J. Busto, *Effect of alcohol on radon adsorption and adsorption*, Internal Note (2016) DocDB:4072.

[84] B. Soule, *Emanation Setup Status and 5 Inch PMT Measurements*, Internal Presentation (2014) DocDB:3270.

[85] DURRIDGE, *RAD7 Radon Detector*, http://www.durridge.com .

[86] H. M. Araújo, J. Blockley, C. Bungau, M. J. Carson, et al., *Measurements of neutrons produced by high-energy muons at the Boulby Underground Laboratory*, Astropartic. Phys. **29** (2008) no. 6, 471–481.

[87] G. Gilmore, *Practical gamma-ray spectroscopy.* John Wiley & Sons, (2011).

[88] IAEA, *IAEA-385 , Irish Sea Sediment*, https://nucleus.iaea.org/rpst/referenceproducts/referencematerials/radionuclides/IAEA-385.htm
.

[89] CERN, *Platform for the simulation of the passage of particles through matter using Monte Carlo methods*, http://geant4.cern.ch .

[90] P. Povinec, *Intercomparisons on Radiopurity Measurements*, Internal SuperNEMO Note (2013) DocDB:2911.

[91] CERN, *An object oriented framework for large scale data analysis.*, http://root.cern.ch/drupal/ **Version 5.26** .

[92] J. P. Stewart and D. Groff, *LabSOCS™ vs. source-based gamma-ray detector efficiency comparisons for nuclear power plant geometries*, 48th Annual Radiobioassay and Radiochemical Measurements Conference (2002) .

[93] DURRIDGE, *RAD7 Communications Software*, http://www.durridge.com .

[94] X. R. Liu, *Low level radioactivity assays with HPGe detectors*, Master's thesis, University College London, (2013).

[95] L. Baudis and A. e. a. Ferella, *Gator: a low-background counting facility at the Gran Sasso Underground Laboratory*, Journal of Instrumentation **6** (2012) no. 08, P08010.

[96] F. Perrot, *Radiopurity measurement of the 8" PMT glass from Hamamatsu*, Internal SuperNEMO Presentation (2014) DocDB:3441.

[97] J. Suhonen and O. Civitarese, *Weak-interaction and nuclear-structure aspects of nuclear double beta decay*, Phys. Rept. **300** (1998) 123–214.

[98] M. Aunola and J. Suhonen, *Systematic study of beta and double beta decay to*

excited final states, J. Nucl. Phys. A **602** (May, 1996) 133–166.

[99] M. Duerr, M. Lindner, and K. Zuber, *Consistency test of neutrinoless double beta decay with one isotope*, Phys. Rev. D **84** (2011) 093004.

[100] A. S. Barabash, F. T. Avignone, J. Collar, et al., *Two neutrino double-beta decay of* ^{100}*Mo to the first excited* 0^+ *state in* ^{100}*Ru*, Phys. Lett. B. **345** (1995) no. 4, 408–413.

[101] A. S. Barabash, P. Hubert, A. Nachab, and V. I. Umatov, *Investigation of* $\beta\beta$ *decay in* ^{150}Nd *and* ^{148}Nd *to the excited states of daughter nuclei*, Phys. Rev. C. **79** (2009) 045501.

[102] NEMO-3 Collaboration, J. Argyriades et al., *Measurement of the two neutrino double beta decay half-life of* ^{96}*Zr with the NEMO-3 detector*, Nucl.Phys. **A847** (2010) 168–179.

[103] S. W. Finch and W. Tornow, *Search for two-neutrino double-*β *decay of* ^{96}*Zr to excited states of* ^{96}*Mo.*, Phys. Rev. C. **92** (2015) no. 4, 045501.

[104] S. Stoica, *Two-neutrino double-beta decay half-lives of 96Zr and looMo Two-neutrino double-beta decay half-lives of* ^{96}*Zr and* ^{100}*Mo to excited states of* ^{96}*Mo and* ^{100}*Ru*, Phys. Lett. B. **350** (1995) no. 2, 152–157.

[105] Y. Ren and Z. Ren, *Systematic law for half-lives of double-*β *decay with two neutrinos*, Phys. Rev. C. **89** (2014) no. 6, 064603.

[106] Alfa-Aesar https://www.alfa.com/en/ .

[107] Zircomet http://www.zircomet.com .

[108] HiCharms http://www.hicharms.com .

[109] R. Arnolda, C. Augierb, J. Bakerc, et al., *Chemical purification of molybdenum samples for the NEMO 3 experiment*, Nuclear Instruments and Methods in Physics Research Section A: Accelerators, Spectrometers, Detectors and Associated Equipment **474** (2001) no. 1, 93–100.

[110] P. Loaiza, V. Brudanin, F. Piquemal, et al., *Obelix, a new low-background HPGe at Modane Underground Laboratory*, AIP Conference Proceedings **1672** (2016) 130002.